AD-A067 348 ARMY ENGINEER WATERWAYS EXPERIMENT STATION VICKSBURG MISS F/G 17/1
ACOUSTIC-TO-SEISMIC COUPLING: PROPERTIES AND APPLICATIONS TO SE--ETC(U)
FEB 79 M D FLOHR, D H CRESS

UNCLASSIFIED WES-TR-EL-79-1 NL

1 OF 2
AD A067348

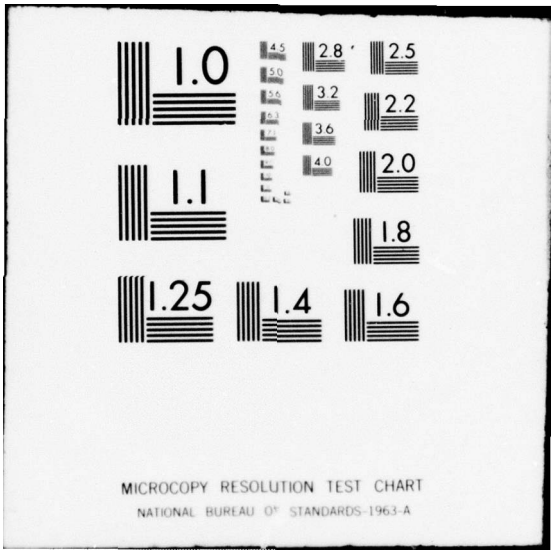
1.0
1.1
1.25
1.4
1.6
1.8
2.0
2.2
2.5
2.8
3.2
3.6
4.0
4.5
5.0
MICROCOPY RESOLUTION TEST CHART
NATIONAL BUREAU OF STANDARDS-1963-A

AD A067348

DDC FILE COPY

LEVEL II

TECHNICAL REPORT EL-79-1

ACOUSTIC-TO-SEISMIC COUPLING; PROPERTIES AND APPLICATIONS TO SEISMIC SENSORS

by

Mark D. Flohr, Daniel H. Cress

Environmental Laboratory
U. S. Army Engineer Waterways Experiment Station
P. O. Box 631, Vicksburg, Miss. 39180

February 1979
Final Report

Approved For Public Release; Distribution Unlimited

Prepared for Sandia Laboratories, Albuquerque, N. Mex. 87115

Under Purchase Order No. 03-9497

DDC
RECEIVED
APR 17 1979
D

79 04 16 040

Destroy this report when no longer needed. Do not return it to the originator.

Unclassified

SECURITY CLASSIFICATION OF THIS PAGE (When Data Entered)

REPORT DOCUMENTATION PAGE

READ INSTRUCTIONS BEFORE COMPLETING FORM

1. REPORT NUMBER (14) WES-TR- Technical Report EL-79-1
2. GOVT ACCESSION NO.
3. RECIPIENT'S CATALOG NUMBER

4. TITLE (and Subtitle) (6)
ACOUSTIC-TO-SEISMIC COUPLING; PROPERTIES AND APPLICATIONS TO SEISMIC SENSORS.

5. TYPE OF REPORT & PERIOD COVERED (9)
Final report, Jul 76 - Feb 78,

6. PERFORMING ORG. REPORT NUMBER

7. AUTHOR(s) (10)
Mark D. Flohr
Daniel H. Cress

8. CONTRACT OR GRANT NUMBER(s)

9. PERFORMING ORGANIZATION NAME AND ADDRESS
U. S. Army Engineer Waterways Experiment Station
Environmental Laboratory
P. O. Box 631, Vicksburg, Miss. 39180

10. PROGRAM ELEMENT, PROJECT, TASK AREA & WORK UNIT NUMBERS
See Block 18

11. CONTROLLING OFFICE NAME AND ADDRESS
Sandia Laboratories
Albuquerque, New Mexico 87185

12. REPORT DATE (11)
February 1979

13. NUMBER OF PAGES
146

14. MONITORING AGENCY NAME & ADDRESS (if different from Controlling Office) (12) 150p.

15. SECURITY CLASS. (of this report)
Unclassified

15a. DECLASSIFICATION/DOWNGRADING SCHEDULE

16. DISTRIBUTION STATEMENT (of this Report)
Approved for public release; distribution unlimited.

17. DISTRIBUTION STATEMENT (of the abstract entered in Block 20, if different from Report)

18. SUPPLEMENTARY NOTES
This study was sponsored by Sandia Laboratories, Albuquerque, New Mexico, under Purchase Order No. 03-9497 having the project title, "Acoustically Coupled Seismic Propagation Study." This study was also conducted in support of the U. S. Army Material Development and Readiness Command in furtherance of Department of the Army Project No. (16) 1A762730AT42 A4 E3/001, "Analytical Techniques for the Design of Environmentally Insensitive Seismic and Acoustic Sensors."

19. KEY WORDS (Continue on reverse side if necessary and identify by block number) (17) A4

Acoustic detection	Mathematical models
Acoustic signatures	Seismic detection
Acoustic-to-seismic coupling	Seismic sensors

20. ABSTRACT (Continue on reverse side if necessary and identify by block number)

Acoustic-to-seismic coupling is investigated using measurements of acoustic and seismic signals generated from acoustic sources. Source types used for the measurements were: pure tones, band limited pink and white noise, and broad band noise from an acoustic impulse (gun shot). The measurements showed that the frequency dependence of acoustic-to-seismic coupling was independent of source type. However, the efficiency of coupling favored certain frequency bands for a fixed source height. → next page

(Continued)

DD FORM 1 JAN 73 1473 EDITION OF 1 NOV 65 IS OBSOLETE

Unclassified

SECURITY CLASSIFICATION OF THIS PAGE (When Data Entered)

038 100

79 04 16 040

20. ABSTRACT (Continued).

Dependence of the coupling on source height was also investigated. Measurements showed that the favored frequency bands were lowered as the source height was increased for frequencies below 250 Hz.

Two techniques were evaluated for separating the acoustic-to-seismic coupled signature from the measured seismic signature in order to support development of methods for suppressing acoustic-to-seismic coupled background noise. Alternatively, such separation could help improve target classification. The two techniques (one using velocity measurements, the other using coherence measurements) were shown to be potentially useful for separating the acoustic-to-seismic coupled part of the seismic signature from the measured seismic signature.

A theoretical approach with a simplified model of plane waves, a smooth surface, and no soil layering was not adequate to explain the measured dependence of acoustic-to-seismic coupling on frequency and source height.

ACCESSION for
NTIS
DDC
UNANNOUNCED
JUSTIFICATION
BY
DISTRIBUTION/AVAILABILITY CODES
Dist. AVAIL. and/or SPECIAL
A

DDC
RECEIVED
APR 17 1979
D

THE CONTENTS OF THIS REPORT ARE NOT TO BE USED FOR ADVERTISING, PUBLICATION, OR PROMOTIONAL PURPOSES. CITATION OF TRADE NAMES DOES NOT CONSTITUTE AN OFFICIAL ENDORSEMENT OR APPROVAL OF THE USE OF SUCH COMMERCIAL PRODUCTS.

PREFACE

This study was sponsored by Sandia Laboratories, Albuquerque, New Mexico, under Purchase Order No. 03-9497 having the project title, "Acoustically Coupled Seismic Propagation Study." This study was also conducted in support of the U. S. Army Material Development and Readiness Command in furtherance of Department of the Army Project No. 4A762730AT42A4/E3/001, "Analytical Techniques for the Design of Environmentally Insensitive Seismic and Acoustic Sensors."

The work was conducted at the U. S. Army Engineer Waterways Experiment Station (WES), during the period July 1976 to February 1978, under the general supervision of Messrs. W. G. Shockley, Chief, Mobility and Environmental Systems Laboratory, B. O. Benn, Chief, Environmental Systems Division (ESD), and Dr. L. E. Link, Chief, Environmental Research Branch (ERB). The ERB and the ESD are now part of the recently organized Environmental Laboratory, Dr. John Harrison, Chief.

This investigation was planned by Mr. J. R. Lundien, ESD, and Dr. D. H. Cress, ERB. Professors L. N. Bolen and H. E. Bass of the University of Mississippi worked with WES in collecting and analyzing the data. Dr. Cress and Mr. M. D. Flohr, ERB, analyzed the data and prepared this report. Sandia Laboratory personnel (specifically Mr. Lyle Porter) helped define specific questions to be addressed in this study.

Other personnel making contributions to this study were Messrs. C. A. Miller and B. T. Helmuth who conducted the field data collection with the University of Mississippi personnel.

Commander and Director of WES during this work and preparation of this report was COL J. L. Cannon, CE. Technical Director was Mr. F. R. Brown.

CONTENTS

	Page
PREFACE	2
CONVERSION FACTORS, METRIC (SI) UNITS TO U. S. CUSTOMARY AND U. S. CUSTOMARY TO METRIC (SI) UNITS OF MEASUREMENT	4
PART I: INTRODUCTION	5
Purpose and Scope	6
Approach	7
Definitions	9
PART II: TEST PROGRAM	11
Test Layouts and Instrumentation	11
Test Site Environment	16
Test Procedures	22
PART III: RESULTS AND ANALYSIS	27
Results	27
Analysis	31
Theoretical Results	38
PART IV: CONCLUSIONS AND RECOMMENDATIONS	45
Conclusions	45
Recommendations	46
REFERENCES	47
TABLES 1-4	
FIGURES 1-26	
PLATES 1-26	
APPENDIX A: MATHEMATICAL METHODS	A1
APPENDIX B: ACOUSTIC WAVES AT BOUNDARIES	B1
Introduction	B1
Spherical Sound Source	B2
Plane Wave Propagation Near a Surface	B6
APPENDIX C: THEORETICAL BACKGROUND	C1
Introduction	C1
Plane Wave Approximation	C1
Boundary Conditions	C1
Acoustic Pressure	C9
APPENDIX D: SITE CHARACTERIZATION MEASUREMENTS	D1
Introduction	D1
Measurement of Seismic Velocities	D1
Measurement of Coherence Length and Ground Surface Impedance	D2
TABLE D1	

CONVERSION FACTORS, U. S. CUSTOMARY TO METRIC (SI)
UNITS OF MEASUREMENT

U. S. customary units of measurement used in this report can be converted to metric (SI) units as follows:

Multiply	By	To Obtain
degrees (angle)	0.0174539	radians
feet	0.3048	metres
inches	25.4	millimetres
pounds (force)	4.448	newtons

ACOUSTIC-TO-SEISMIC COUPLING; PROPERTIES AND APPLICATIONS TO SEISMIC SENSORS

PART I: INTRODUCTION

1. Seismic and acoustic signatures have been used separately and in combination by sensors to detect, classify, and locate military targets. Devices that use the seismic signature of such targets have experienced a degradation in their performance that is attributable to the coupling of acoustic energy to the terrain. Such coupling contributes a component to the total signature received by the sensor that has not been systematically included in the design of seismic sensors.

2. The characteristics of the acoustic-to-seismic coupled component of the signature that affect the performance of seismic sensors depend on the sensor type and function. Presently, two types of seismic sensors (point sensors and line sensors) employing two functions (detection only and both detection and classification) are being used by the military. Point sensors are being designed that will be responsive to targets at greater distances than are line sensors (i.e., 10 m or greater for point sensors versus 2 m or less for line sensors). Because of the nature of propagating seismic wave forms for intruder-type sources (personnel, wheeled and tracked vehicles), point sensors generally use higher frequency components[1] (10 to 100 Hz) for detection and classification than do line sensors (which respond to frequencies below 10 Hz).

3. The degradation in performance attributable to acoustic-to-seismic coupling can be caused by:

a. Masking of the component of the signature induced by surface-contact targets (such as walking man) by a larger component induced by acoustic background noise (in the same frequency range as the component of the surface-contact target).

b. Distortion of the seismic signature of an acoustically active target (aircraft or vehicle) by the acoustic-to-seismic coupling phenomenon so as to make the resultant

signature unrecognizable (for detection or classification) by the sensor.

4. To adequately determine the extent to which acoustic-to-seismic coupling can either be exploited or suppressed, improved understanding of the coupling phenomenon is needed. Alternate signal-processing techniques to those currently being used by sensors need to be further investigated with the practical objective of identifying ways of separating the acoustically induced component of the seismic signature from that induced by surface contact.

Purpose and Scope

5. The overall purposes of the study reported herein were:

   a. To develop a mathematical technique for predicting the characteristics (frequency and amplitude) of seismic signatures induced by acoustic-to-seismic coupling.

   b. To develop a concept for separating the component of the seismic signature induced by surface contact from that induced by acoustic-to-seismic coupling.

6. It would be desirable to have a mathematical technique available for predicting the frequency and amplitude characteristics of acoustic-to-seismic coupled components of the signature as a function of the source-to-sensor geometry (range, angle of incidence, depth of sensor, etc.) and the physical properties of the air and the terrain (temperature, densities, surface vegetation, compression and shear moduli of soils, etc.). However, formulations available in the literature for calculating the transmission of vibratic across fluid-solid interfaces have not been applied to the complex environmental situation of an acoustic vibration in air crossing a terrain interface. As a beginning in the development of new formulations to fill such a gap, the theoretical and data analysis aspects of this study were directed toward investigating geometric and environmental factors affecting the transmission of acoustic vibrations in air into the terrain and toward investigating the applicability of conventional formulations, assuming a plane, frictionless interface between a fluid and a solid,

to predict the transmission of such vibrations from the air into the terrain.

Approach

7. As implied in the preceding paragraph, the approaches used in this study were both theoretical and experimental. The theoretical approach consisted of applying plane-wave theory for a fluid over a solid interface to predict measurable quantities describing the transmission of vibrations in air into the terrain. The experimental approach consisted of using measured data to:

a. Evaluate the adequacy of the theoretical approach for predicting the transmission of vibrations in air into the terrain.

b. Identify properties of the acoustic-to-seismic coupled signatures and factors (geometric relationships between the source and sensor, physical properties, etc.) affecting their characteristics.

c. Evaluate the potential of two techniques for separating the acoustic-to-seismic coupled component of the seismic signature from the component induced by surface contact.

8. The two techniques investigated for separating the acoustic-to-seismic coupled component of the seismic signature from the component induced by physical contact with the surface (presumably by an intruder) both required the use of multiple sensors. The first technique investigated is based on exploiting differences in the velocity of propagation of the two components. If the predominant portion of the component of the seismic signature induced by the movement of an acoustic wave parallel to the terrain surface moves with the velocity of sound in air, this component can be identified by using an appropriate array of geophones. Since the predominant component of the signature induced by physical contact is Rayleigh wave motion, hence having a velocity generally less than the velocity of sound in air, the Rayleigh wave component can be identified by its slower velocity. For this technique to be a viable candidate for distinguishing between the two components of the seismic signature, it must be demonstrated that the

predominant portion of the component of the signature induced by an acoustic wave moving parallel to the surface moves at or near the velocity of sound in air.

9. The second technique is based on the degree of correlation between the signature received by a microphone and a collocated geophone. The correlation is carried out at each frequency of the measured signatures. If the correlation between the microphone and geophone signatures at a given frequency is high, it is reasonable to attribute the signature at that frequency to an acoustic source. If the correlation is low and the signature from the geophone is above the ambient background noise level, it is reasonable to attribute that component to a physical contact source. To prove this technique a viable candidate for distinguishing between the two components of the seismic signature, it must be demonstrated that for an acoustic source there does, in fact, exist a high degree of correlation between the microphone and geophone signatures.

10. Field measurements were obtained twice during the study. The first set of measurements (Test I) was obtained in December 1976, and the second set (Test II) was obtained in March 1977.

11. This report consists of four parts:

a. Introduction, Part I.

b. Test Program, Part II.

c. Results and Data Analysis, Part III.

d. Conclusions and Recommendations, Part IV.

12. Four appendixes are presented at the end of this report. Appendix A discusses mathematical methods used in the spectral analysis. Appendix B discusses reflection and transmission of acoustic waves at boundaries in terms of acoustic impedances of the media. Appendix C discusses the theoretical calculation of acoustic-to-seismic coupling in terms of measured variables (seismic particle velocity and acoustic sound pressure). Appendix D discusses the site characterization measurements (compression, shear, and Rayleigh wave velocity, coherence length, and ground surface impedance) and the results of these measurements.

Definitions

13. A summary of terms, and their definitions as used in this report, is presented below.

a. Acoustic impedance--The complex representation of average sound pressure at a vibrating surface divided by the complex representation of the volume velocity at the surface.

b. Autospectrum--The square of the amplitude or modulus of a signature as a function of frequency.

c. Band limited white noise--White noise with a frequency band of 45-1800 Hz in Test I, 25-2000 Hz in Test II.

d. Coherence--Measure of the stability of the phase difference between two signatures for a particular frequency (see Appendix A).

e. Coherence length--The separation distance between microphones for which the peak amplitude of the correlation function falls to a value of $1/e$ (e is the base of the natural logarithm) of the value it would have for zero separation (see Appendix D).

f. Correlation function--The area under the curve representing the product of two normalized signatures as a function of the amount of shift of the independent variable (usually time) of one signature relative to the other.

g. Ground surface impedance--Quantity for determining reflection and refraction properties of the ground surface (see Appendix D).

h. Impedance--The ratio of pressure to particle velocity at the same point in a sound wave.

i. Intensity ratio--The square of the ratio of the amplitude of the seismic particle velocity for a particular frequency to the amplitude of the sound pressure above the geophone for the same frequency.

j. Octave band pink noise--Pink noise banded such that the frequency of the upper half-power point is twice the frequency of the lower half-power point. The roll-off from the half-power points is 48 db per octave.

k. One-third octave band pink noise--Pink noise banded such that the frequencies of the half-power points are given by $2^{\pm 1/6}$ times the center frequency. The roll-off from the half-power points is 48 db per octave.

l. Phase difference--Angular difference between two sinusoids for a particular frequency.

m. Pink noise--Random noise such that all octave bands contain the same amount of total power.

n. Poisson's ratio--The ratio of the strain in the transverse direction to the longitudinal strain.

o. Pure tone--Monofrequency signal.

p. Sound pressure--Difference in pressure between instantaneous pressure and the static pressure.

q. Specific flow resistance--Ratio of the pressure difference in a fluid to the fluid velocity.

r. White noise--Random noise such that all frequencies have the same amount of power.

PART II: TEST PROGRAM

14. To address the experimental approach to this study (paragraph 7), data were needed for comparing theoretically derived characteristics of acoustic-to-seismic coupled signatures with measured characteristics and to identify properties of such signatures and factors affecting the acoustic-to-seismic coupling phenomenon. Data were also needed to evaluate the extent to which the two techniques for separating the acoustic-to-seismic coupled component from that induced by surface contact (paragraphs 8 and 9) were viable. Accordingly, measurements were obtained to identify or evaluate:

a. Dependence of acoustic-to seismic coupling on
   (1) Source type.
      (a) continuous waves with different bandwidth.
      (b) impulse (broadband).
   (2) Angle of incidence of acoustic waves.

b. Velocity of propagation of acoustic-to-seismic coupled signature.

c. Techniques for separating the seismic signature components (paragraphs 8 and 9).

d. Terrain and atmospheric conditions.

15. This part of the report consists of three sections: test layouts and instrumentation, test site environment, and test procedures. The first section describes the test layouts and measurements for items a through c above. The second section presents the measurements of the terrain and atmospheric conditions of the test site (d above). Test procedures are explained in the third section.

Test Layouts and Instrumentation

Test layouts

16. As discussed in paragraph 10, the test program consisted of two testing periods, Test I and Test II. The test layouts for Test I and Test II are shown in Figures 1 and 2, respectively. The rationale

for the layouts is given in the following paragraphs.

17. The quantity chosen to represent acoustic-to-seismic coupling characteristics was the square of the ratio of the seismic particle velocity to the sound pressure above the ground surface at each frequency. Therefore, the sound pressure was measured by a microphone placed (above the ground) directly over the geophone measuring the seismic particle velocity. In order to provide data to investigate the effect of the angle of incidence on the intensity ratio, geophones were placed close to the source (10 m) to obtain a large range of incident angles (5.7-45 deg for a speaker height range of 1-10 m) while maintaining a distance large enough for the speaker to be considered a point source.

18. The measurements of propagation velocities required at least two geophones spaced radially outward from the source. However, more than two geophones were used in order to average results. Two linear arrays of six geophones were used for velocity measurements in Test I: one array had 0.75-m spacing and the other array had a 1.5-m spacing between geophones. (In Figure 1 only nine geophones were needed to complete the two arrays at location 2 because three of the geophones for the 0.75-m spacing could be used for the 1.5-m spacing.) In Test II, there was a six-geophone array approximately 10 m from the speaker location (0.75-m spacing) and a three-geophone array at location 2 (1.5-m spacing) (Figure 2).

19. In order to exploit the velocity of propagation of the acoustic-to-seismic coupled wave for its separation from the physical contact component (paragraph 8), the velocity of the acoustic-to-seismic coupled wave had to be measured to demonstrate that its predominant part moved at the velocity of sound in air. The velocity characteristics were examined using an impulsive source and time of arrival of the impulse at the geophone arrays (paragraph 82). If the predominant part of the acoustic-to-seismic signature moved with the velocity of sound, the dominant part of the seismic signature would arrive at the same time as the dominant part of the acoustic signature. On the other hand, the impulse induces ground motion continuously from the source to the

geophones. It can be expected that the induced ground motion would spread from the point of acoustic-to-seismic coupling as a seismic wave, although the amplitude of the spreading wave may be considerably smaller than the directly coupled wave (i.e., that wave originating immediately from the change in the acoustic pressure above the ground). The induced seismic wave could be expected to move at a velocity dependent on the bulk properties of the media (hence, not necessarily the acoustic velocity in air). If the directly coupled wave dominated relative to the spreading wave, the dominant portion of the seismic signature of the impulse should arrive at the same time as the acoustic signature of the impulse. The directly coupled wave should have considerably greater amplitude than the residual vibration in the signature arriving before or after the acoustic record of the impulse. For such a comparison of the time of arrival of the acoustic and seismic components of the impulse signatures, a collocated microphone and geophone were needed. For measurement of the velocity of the seismic propagating components, a geophone array was needed.

20. In order to measure the coherence for use in separation of the components of the seismic signature (paragraph 9), a collocated microphone and geophone were needed.

Instrumentation

21. The system used to generate and collect seismic and acoustic signals consisted primarily of a source, transducers, amplifiers, and a recording system, as illustrated in Figure 3. In order to obtain quantitative data for analysis, the system was calibrated by applying known inputs to the various components of the system and tabulating the respective outputs. The following paragraphs describe the types of equipment used in the system and also briefly explain the various procedures used for calibration.

22. Source. The acoustic signal source was one of two types: continuous or impulsive. The continuous source was a large bass-reflex speaker system (Altec Corporation) driven by a relatively large stereo amplifier (McIntosh 175-watt amplifier). The stereo amplifier was driven by either a frequency sweep generator (Spectral Dynamics

model SD104A) or by a cassette tape recorder, depending on the desired type of output signal. The output of the cassette tape recorder was amplified with a direct-current (DC) amplifier (Bell & Howell CEC 1-165) prior to input to the McIntosh amplifier. Cassette tapes containing pure tones at octave band intervals (i.e., 25, 50, 100, 200, 400, 800, and 1600 Hz), white noise signals, and pink noise signals at selected octave band and one-third octave bandwidths were supplied by the University of Mississippi personnel. Table 1 shows the center frequencies and half-power points of the pink noise sources used. The impulsive sources were a 45-caliber U. S. Navy line thrower in Test I and a 12-gauge shotgun in Test II.

23. For purposes of analysis, the speaker was treated as a point source generating spherical waves. Figure 4 is a diagram of the directivity pattern of the speaker. The zero degree position is directly in front of the speaker. For a spherical wave source, the amplitude contours in Figure 4 (i.e., the curves showing the amplitude of the wave, in decibels, as a function of angle from directly in front of the speaker) should be circular. Such is the case, or at least nearly so, for frequencies below 600 Hz. The increased directionality (or decreased sphericity) at higher frequencies (above 600 Hz) is a characteristic of radiating circular pistons. For the source-microphone geometries used in the test program, the angles of the source-microphone line with the ground surface were as large as 45 deg. A deviation from sphericity of ± 2 db was considered the maximum allowable without making corrections for directionality.

24. A field calibration was made of the speaker system by measuring the frequency response of the speaker using a microphone placed under the speaker (Figure 5a). The units of relative response as plotted in Figure 5b are decibels (using the peak response as the reference level). A theoretical frequency-response curve (Figure 6) was provided by the manufacturer of the speaker. Comparison of Figures 5 and 6 shows that the actual response was not as good as the theoretical response for frequencies below about 32 Hz. The specifications for the design of the speaker cabinet were provided by the manufacturer.

25. Transducers. Seismic-response data were measured using Mark Products L1U-3D scientific triaxial geophones that are capable of detecting seismic signals in the vertical, radial, and horizontal* directions with a frequency range from 1 Hz to frequencies exceeding 500 Hz. These were buried beneath approximately 5 cm of soil. To effect field calibration, the amplifiers for each geophone channel were set to gains to be used during each test. A sine wave voltage was applied to the amplifier, and the voltage was varied until a 1-volt root-mean-square (RMS) signal was output to the recorder. The input voltage readings were recorded in the data log so that voltages generated by the geophones during each test could be calculated. The particle velocity signal amplitude can then be computed by multiplying the calculated voltage output of the geophone by the geophone sensitivity.

26. Acoustic transducers (General Radio (GR) and B&K model 4135) consisted of capacitance-type microphones. The microphones were calibrated with a GR Type 1662 sound-level calibrator, which provides a 250-Hz sine wave signal with a known sound pressure level. To effect calibration, the gain setting of the microphone amplifier (Bell and Howell CEC 1-165 DC amplifier) was set so that 1-volt RMS was applied to the tape recorder. During testing, any changes in the amplifier gain settings were recorded in a data log, so that the sound pressure levels recorded from the microphone could be computed. The sound pressure units used in this report are microbars (μbars), which convert to decibel (db) units as follows:

$$P(db) = 20 \log \frac{P(\mu bars)}{0.0002}$$

where

P(db) = sound pressure level in db

P(μbars) = sound pressure in μbars

---

* Horizontal refers to the axis of a seismic sensor and as used here indicates the axis is horizontal and perpendicular to the speaker-geophones line; radial indicates the axis is horizontal and aligned with the speaker-geophones line.

27. Amplifiers. The amplifiers used for the seismic and acoustic signals are commercially available DC-powered units. These units are specified to provide gains from 10 to 2,500 times the input voltage. They provide a standard flat frequency response from 0 to 10,000 Hz. The gain setting of each amplifier used was recorded during each test run.

28. Recording system. The recording system consisted of a 14-channel magnetic tape recorder conforming to Inter-Range Instrumentation Group (IRIG) standards. Data were recorded at a tape speed of 7.5 ips. All data were recorded by frequency-modulating a carrier frequency provided in the recording electronics. This results in a frequency response from 0 to 2500 Hz when run at 7.5 ips. This system will provide good recording fidelity (DC-2500 Hz; less than 1.5 percent total harmonic distortion; signal/noise ratio, 46 db) for input signals less than the calibration voltage (1.4 volts, zero to peak) and larger than the system noise level (approximately 0.02 volts). The analog signals were digitized before analyzing the data. The digitizing rate was 5000 samples/sec for Test I and 2500 samples/sec for Test II. The digitized data were multiplexed on 18-bit-binary coded tapes and converted to 36-bit-binary tapes for use on the Honeywell G635 at the U. S. Army Engineer Waterways Experiment Station (WES).

29. During the tests, specified portions of the collected data were played back onto a strip chart recorder to provide preliminary field analysis. This recording configuration provided a hard copy of the signal output. The galvanometers used have a frequency response from 0 to 500 Hz. This limited bandwidth response was considered adequate for field analysis of the data.

Test Site Environment

Rationale for site documentation and selection

30. A number of physical parameters affect acoustic and seismic propagational phenomena (vegetation height and density, surface roughness, soil layering, etc.). In addition, adverse environmental

conditions can degrade the measurements of the seismic and acoustic signatures during testing. Background noise (seismic and acoustic) from local cultural activity and wind noise can mask the desired signatures. Atmospheric turbulence due to localized variations in air flow and physical properties of the air (pressure and temperature) can reduce the coherence of the acoustic wave train to the extent that phase-sensitive measurements cannot be obtained. Large temperature gradients above the ground surface can refract the acoustic wave so that straight-line approximations for determining acoustic path length are no longer valid.

31. In order to properly document site conditions and to select an appropriate site for testing, it was necessary to identify factors affecting acoustic and seismic propagation. The factors are:

a. Seismic.

(1) Topography.

(2) Bulk properties of soils (compression wave velocity, shear velocity, bulk density).

(3) Depths to interfaces. (Interfaces are defined by boundaries between earth media having significantly different bulk properties.)

b. Acoustic.

(1) Atmospheric conditions (temperature, wind velocity).

(2) Vegetation.

32. Several acoustic measurements can be made to further document the effects of atmospheric and surface terrain conditions on the propagation of acoustic waves, although they are only indirectly related to the above factors. These measurements are the coherence length of the atmosphere and the surface impedance. The coherence length of the atmosphere is a measure of the stability of the phase of the propagating signal over distance. The coherence length can be affected by local variations in atmospheric conditions, particularly by turbulence induced by wind. Phase-sensitive measurements are valid only if the acoustic waves are coherent over the path length across which the phases are

being compared (i.e., the coherence length must exceed this path length). Appendix D further describes the coherence length and its measurement. The measurement of the surface impedance identifies the phase change and energy loss of the reflected wave from the terrain boundary relative to the incident wave.

Requirements

33. To simplify the environmental contribution to the total phenomenon of acoustic-to-seismic coupling, it was desirable to have a site for which the number of factors affecting acoustic and seismic propagation was minimized and those factors that could not be eliminated were, in so far as possible, uniformly distributed. The following characteristics were identified as desirable:

a. Topography: A flat surface (i.e., local variation in surface geometry less than 0.5 m in a horizontal distance on the order of 5 m).

b. Soils: Uniform soil conditions with homogeneous material near the surface (i.e., within several metres of the surface).

c. Vegetation: Small surface vegetation (i.e., height less than shortest acoustic wavelengths of principal interest in the tests, approximately 0.5 m).

d. Low background noise (seismic and acoustic).

e. Low atmospheric turbulence.

f. Small vertical temperature gradient above ground.

34. A flat surface is desirable for uniform acoustic-to-seismic coupling. Experimental and theoretical work done by WES[2] has shown that the frequency content of seismic signature generated by footsteps, wheeled vehicles, etc., is dependent on the thickness of soil layers. A thick top layer (on the order of 10 m thick) would approximate an infinite half-space condition, and this would be preferable for an initial investigation of acoustic-to-seismic coupling. Large surface vegetation (tall grass, brush, trees, etc.) can cause wind-induced soil motion that masks the acoustic-to-seismic coupled signatures. Reflection of acoustic waves from large surface vegetation would complicate the analysis of data.

35. Background noise levels, particularly from seismic sources,

need to be minimized. To accomplish this, the selected site had to be several hundred metres from light vehicle traffic. Time of testing could be controlled so as to minimize degrading effects of seismic or acoustic background noise sources. Atmospheric turbulence, induced principally by wind noise, had to be such that the coherence length requirements for testing were met. The "worst case" requirement was for the surface impedance measurements, for which the coherence length had to exceed 30 m.

36. A temperature gradient above the ground surface will result in refraction of waves to the extent that straight-line approximations for the acoustic path length used in subsequent analyses (principally for ground-surface impedance measurements) become invalid. Small-scale temperature gradients, less than 5°C within a few centimetres of the surface are of little consequence, since several centimetres is a small length compared with the acoustic wavelengths of interest and overall path length from the source to the receiver (10 m or greater for phase-sensitive measurements involving the direct and reflected waves). A temperature gradient requirement necessary for assuming straight-line propagation is that it not exceed 1°C/m. Using methods in Reference 3, this gradient will give a path-length difference between a direct path of 60 m (largest experimental range) and the corresponding refracted path of less than a tenth of a wavelength for frequencies less than 500 Hz (one of the higher frequencies used in tests).

Description of test site

37. The test site chosen for data collection (Figure 7) is located at the far eastern boundary of the WES installation in an area that has been set aside for field experiments. Specifically, the test site is located approximately 220 m from Porter's Chapel Road in the northwest quarter of Section 6, Township 15 North, Range 4 East, in Warren County, Mississippi. Warren County is located in the west-central part of the state. The Mississippi River forms the western border of the county, except for a small part of the county that lies west of the river and is bordered by Louisiana. The remainder of this section provides a description of the test site.

38. Topography. The general topography in this area consists of rolling hills. The test site is relatively flat with a gradual drop in elevation from south to north of approximately 1 m per 100 m. A photograph of the test site is shown in Figure 7b.

39. Soils. The surface soil is a brown to dark brown heavy silt loam (Unified Soil Classification System, CL). The texture of the subsoil ranges from heavy loam (CL) to silty clay loam (CL).

40. The shear and compression strength properties of soil were documented by measuring the shear, Rayleigh, and compression wave velocities of the soil medium. As shown in Figure 8, measurements documenting seismic properties were obtained at three locations on the site. These velocities were measured using standard seismic-refraction techniques (see Appendix D).

41. Table 2 presents the results of the measurements of compression and shear wave velocities for Test I and Test II. The seismic measurements obtained just prior to Test I indicated that the near-surface (i.e., surface to 5 m) soil conditions were uniformly distributed across the site. Only one compression wave measurement (at location 2 in Figure 8) was made for Test II. The table shows that the first-layer compression wave velocity and layer depth measurements obtained for Test I at location 2 (30 m from speaker) were very similar to those measured in Test II at the same location. The second layer velocity did vary significantly over the site possibly because of varying degrees of water content across the site. However, in view of the depth of the top layer (5-6 m), the effects of variation in second layer velocity on the acoustic-to-seismic coupling phenomenon were not expected to be significant.

42. Rayleigh wave velocity measurements were also obtained prior to Test I and after Test II. The results are shown in Figure 9 and show no more than a 10 to 20 percent change from Test I to Test II. The method used to obtain the Rayleigh wave velocity may lend itself to as much as 10 percent error in the wave velocity determination. Past experience of WES personnel in relating the response of the terrain to surface stresses as a function of seismic velocities of the terrain has

indicated that a 10 to 20 percent change in the Rayleigh wave velocity does not significantly affect the seismic response of the terrain when compared with the range of Rayleigh wave velocities that occur in common terrain environments (i.e., forty to several hundred metres per second, excluding rock). Therefore, the differences in seismic wave velocities between Test I and Test II are not considered to be very significant.

43. Vegetation. As can be seen in Figure 7b, the test site contains sparsely distributed, short grasses. The grasses and vegetation extend to a considerable distance to the west of the site. Along the eastern boundary, approximately 30 m from the test area, the vegetation consists of moderately dense woods having an upper canopy height of approximately 20 m. The underbrush is relatively thick with a bed of leaves and sparse grasses. The perimeter line separating the dense woods on the eastern boundary from the short vegetation of the test area was selected to be parallel to the direction of propagation of the acoustic signatures from the source to the sensor so that reflected energy would not be moving in the same direction as the directly propagating waves.

44. Low background noise and atmospheric turbulence. The requirement for low background seismic noise was met by conducting tests at times when there was very little traffic on the nearby road (paragraph 37).

45. For the low background acoustic noise criterion, wind noise was monitored during the test in an effort to restrict data collection to times when the wind velocity did not exceed 3.5 m/sec. The wind velocity during Test I measurements ranged from 0.0 to 3.0 m/sec. The wind velocity for Test II ranged from 2.7-3.7 m/sec during site documentation measurements of coherence length (see Appendix D for results). The wind velocity for the remainder of measurements in Test II was less than 3.0 m/sec. Although the wind velocity exceeded the desired limit of 3.5 m/sec, the coherence length (measured during these windy conditions) was sufficient (i.e., exceeded 30.0 m). Thus, it was concluded that the background noise level and wind turbulence did not degrade the data collected during the test.

46. Small temperature gradient above ground. Readings of temperature were made at several elevations above the ground throughout Tests I and II. Figure 10 shows the device used for these measurements. Temperature sensors were placed at 1.52-m intervals on the pole, from the base to 6.1 m. The temperature extremes (minimum and maximum) for five days, recorded by the four temperature sensors at or above 1.52 m, are presented in Figure 11. The measured values showed that the maximum temperature gradient over the five days of testing was less than 1°C/m for measurements above the ground. Therefore, the temperature gradient requirement in paragraph 36 was met for heights between 1.52 m and 6.1 m above the ground. The gradient between the ground and 1.52 m above the ground exceeded 1°C/m during several testing periods. However, the assumption of straight-line propagation may still be good if most of the temperature difference occurs within a few centimetres of the surface (see paragraph 36).

47. It can be concluded that all the environmental requirements were met or did not significantly degrade the assembled data for the frequency range of interest. Therefore, the measured data did not need to be adjusted or corrected because of environmental conditions.

Test Procedures

48. This section presents a description of the test procedures (i.e., sources, sensors used, their locations, etc.) for the test program. The measurement categories address those measurements identified in paragraph 14. The measurement categories, corresponding source types, and the number and location of geophones and microphones are summarized in Table 3. The notation for locating geophones and microphones as presented in Table 3 is keyed to Figures 1 and 2 where geophones and microphones are identified by lower- and upper-case alphabetical characters, respectively. Only those measurements of the terrain and atmospheric conditions that were made using the instrumentation previously discussed (i.e., speaker and microphones) are included in the description of these procedures, namely measurements of coherence length

and surface impedance. Other data documenting terrain and atmospheric conditions were presented in paragraphs 38 through 46.

Dependence of coupling on source type and incident angle

49. As can be seen from Table 3, three source types were used for determining dependence of coupling on source type in Test I, i.e., 20-300 Hz frequency sweep, octave band pink noise, and the impulsive source. The tests using the frequency sweep source made use of a signal generator (paragraph 22) whose output was played through the McIntosh 175-watt amplifier. The signal generator was set to generate a signal sweeping in frequency from 20-300 Hz at a rate of 2 Hz/sec. Recordings of the outputs of microphone B and the vertical transducer of geophone d were made. As described in paragraph 22, the tests using the octave band pink noise as a source made use of five sets of prerecorded pink noise with center frequency and half-power point characteristics listed in Table 1. The prerecorded pink noise was played through the amplifier-speaker arrangement for the speaker located 2.44 m above the ground. The outputs of microphone A and the geophone d were recorded. To conduct the test with the impulse source, the recorder was turned on, and a 45-caliber Navy line thrower held at 1.5 m above the ground was discharged three times within a 30-sec time interval. The recording instrumentation required to record the outputs of microphone B and the vertical transducer of geophone d (Figure 1) was turned on 15 sec prior to discharging the first round and was turned off about 15 sec after the last round was fired.

50. For test II, the same frequency sweep generator was used as in the first series of tests, but it was set up for a logarithmic sweep (0.5 decades/min). This reduced the amount of time needed to sweep the range of frequencies 20-700 Hz and still gave a sufficiently slow sweep rate for the frequencies below 100 Hz. For this test series, the speaker height was 2.44 m, and outputs from microphone B and the vertical transducer of geophone g were recorded.

51. In Test II, data to study the dependence of coupling on incident angle were collected in addition to the data needed to study

the effects of source type. As can be seen in Table 3, the tests using pink noise made use of narrower bands than for Test I, i.e., one-third of an octave instead of a full octave of pink noise at various speaker heights. In a manner identical to Test I, the prerecorded pink noise was played through the McIntosh 175-watt amplifier, and outputs from microphones A and B and the vertical and radial transducers of geophones d and g were recorded. The initial speaker height was 1.0 m. All of the one-third octave bands were played sequentially (30 sec each) before the speaker was raised to the successive positions indicated on Table 3.

Velocity of propagation of acoustic-to-seismic coupled signatures

52. Table 3 shows that the source used for determining the velocity of propagation was the octave band pink noise in Test I and the one-third octave band pink noise and broadband white noise in Test II. The speaker was at 2.44 m in Test I, and the output of the vertical transducers of the linear array of six geophones (1.5-m spacing) was recorded simultaneously during broadcast of the octave band pink noise data. The measurements for the velocity of propagation during Test II were run coincidentally with the measurements for determining coupling dependence on source type and incident angle. In Test II, the vertical and radial transducers of geophones a-f (array at 10 m in Figure 2) were recorded.

Separation of seismic signatures

53. By velocity. Since the impulsive source was used for this measurement category, the data for this were recorded at the same time as the impulse tests for measurements of the coupling dependence on source type in Test I (paragraph 49). Outputs were recorded for the vertical transducers of geophones b-g.

54. By coherence. The data used for this analysis were the same used for determining the dependence of coupling on source type for the pink noise sources of Test I and Test II (i.e., the outputs of microphone A and the vertical transducer of geophone d for Test I and

microphone B and the vertical transducer of geophone g for Test II).

Terrain and atmospheric conditions

55. Coherence length. Prerecorded band limited white noise was the source used for this measurement in both Test I and Test II. Both lateral and radial coherence length measurements were made. In Test I, lateral coherence length measurements were made at location 2 for two microphones (marked as microphones E-L in Figure 1, each at a height of 0.91 m) equidistant from the speaker and laterally separated by 1.0 m, 3.0 m, 5.0 m, and then 10.0 m. Three minutes of white noise was played for each separation distance. This was repeated for microphones (M-T in Figure 1) at 60 m with the microphones at ground level.

56. In Test II, the same source was used but with four microphones (D, E, F, and I in Figure 2) at location 2: one (I) on the speaker-geophone line, one (F) at 3.0 m, one (E) at 10.0 m, and the last (D) at 20.0 m from this line. Again, three minutes of prerecorded white noise was played for the test, but it had to be played only once to get information for the four separation distances. This was done only at location 2 in Test II.

57. For the radial coherence length measurement, the microphones (A and D in Figure 1 and B and C in Figure 2) were placed at ground level at 30 m and 60 m from the speaker location in Test I and Test II during the pink noise tests for determining coupling dependence on source type and angle of incidence.

58. Ground surface impedance. Two source types are shown in Table 3 for generating the acoustic energy needed for measurements that were used to calculate ground surface impedance in Test I. The first source shown, pure tones at octave band intervals, was prerecorded on cassette tapes and played through the McIntosh amplifier, 60 sec for each tone. The output of one microphone (C) on the ground under the speaker and two microphones at location 2 were recorded. One microphone (A) at location 2 was initially on the ground and the other (B) was 0.91 m above the ground. The microphones at location 2 were each raised 0.15 m, and the pure octave tones were played again. This was repeated five times until the lower microphone was at 0.75 m and the

upper one at 1.66 m. The entire test was repeated in an identical fashion for the microphone under the speaker and two microphones (D and U) at location 3 (Figure 1). The ground surface impedance at high frequencies determined from data collected in this manner represents an average over the surface. For low frequencies, a larger separation between microphones is needed because of the large wavelengths associated with them. Therefore, only three largely different measurement points could be used from these tests for low frequency impedance values (i.e., microphone outputs from locations 0 m, 30 m, and 60 m radially outward from the source).

59. In Test II, separate tests were made for the ground surface impedance measurement, using the prerecorded one-third octave band pink noise. Each band was played for 40-45 sec. This was done in two sets. First, five microphones (G, H, I, J, and K) were placed at 10 m, 20 m, 30 m, 40 m, and 43 m with the heights shown in Table 3; and then the five microphones (A, J, L, M, and N) were placed at 10 m, 40 m, 50 m, and 60 m, and 63 m with the heights shown in the table.

PART III: RESULTS AND ANALYSIS

60. This part of the report describes how the data collected in the tests for items a, b, and c (paragraph 14) were reduced and analyzed. The coherence length and ground surface impedance data for documenting terrain and atmospheric conditions (paragraph 14, d) are discussed in Appendix D. The test results for the acoustic-to-seismic coupled component are discussed in the first section of this part. An analysis of the experimental results is presented in the second section. A comparison of theoretical and experimental results is discussed in the third section.

Results

Dependence of coupling on source type and incident angle

61. Source type. The quantity chosen to represent the coupling characteristics will be called the intensity ratio and is calculated using

$$\text{Intensity ratio} = \left[\frac{v(f)}{P(f)}\right]^2 \tag{1}$$

where

v = seismic particle, 10^{-3} cm/sec

P = sound pressure, μbars

f = frequency, Hz

The intensity ratio results for Test I are presented in Figure 12 for the three source types listed in Table 3 derived from data collected for collocated seismic and acoustic sensors at location 2 (30 m) as shown in Table 3.

62. Figure 12a was obtained from the 20- to 300-Hz frequency sweep test. Only data to 150 Hz are shown here for comparison with the results of the first two octave bands of pink noise. Data from the full

frequency range (20-300 Hz) will be discussed further in the analysis (paragraph 71). The derivation of the intensity ratio from the frequency sweep was made by measuring the particle velocity and source pressure at selected frequencies from calibrated (voltage converted to engineering units of seismic particle velocity and sound pressure) plots of the analog signals from the seismic and acoustic sensors.

63. In order to calculate the intensity ratio results for the other plots in Figure 12, the analog data were digitized at the rate of 5000 samples/sec, and the digital information from each of the channels was multiplexed into one channel so that the data on this channel looked like

CH 1 (1), CH 2 (1), ...; CH 1 (2), CH 2 (2), ...; ...

where

CH = channel

(n) = n time increments

The spectral analysis of this digitized data was made using a discrete Fast Fourier Transform (FFT). A time sample of 2048 points (0.4096 sec in Test I, 0.8192 sec in Test II) was taken from the digitized data. The intensity ratio was calculated as the square of the ratio of the seismic amplitude spectrum and the acoustic amplitude spectrum obtained from the FFT using the relation shown in Equation 1. These results were sufficient to show the dependence of acoustic-to-seismic coupling on source type. Therefore, reduction of Test II data for study of the dependence on source type was not considered necessary.

64. Incident angle. As shown in Table 3, the source used to determine the coupling dependence on incident angle (speaker height) in Test II was the one-third octave band pink noise. The center frequencies of these bands (Table 1) were chosen to correspond to peaks and dips in the intensity ratio results of Test I. The data were analyzed in the same way as the Test I octave band noise data, except that the digitizing rate was reduced to 2500 samples/sec. Plates 1-15 show the intensity ratio results for the five speaker heights (1, 2.44, 5, 7.5,

and 10 m) and for three one-third octave band frequency ranges (center frequencies of 40, 90, and 220 Hz) for measurements at the 10-m location.

Velocity of propagation of acoustic-to-seismic coupled signatures

65. The determination of the velocity of propagation is item b in the introduction of the test program (paragraph 14). Table 3 shows the source and sensors used for this calculation in Test I and Test II. Since seismic waves are generally dispersive, the velocity was calculated as a function of frequency. The travel time for a given frequency was obtained using the phase difference between seismic signatures obtained at each geophone for each frequency (see Appendix A for phase calculation using Fourier coefficients). Once the phase difference between geophone signatures had been obtained, the phase difference was related to the travel time by the relationship:

$$\Delta\phi = \omega\Delta t \tag{2}$$

where

$\Delta\phi$ = phase difference, rad

ω = circular frequency, rad/sec

Δt = time difference between signals (travel time), sec

Therefore, once the phase difference and the spatial separation are known, the velocity can be computed from

$$v = \frac{\Delta x}{\left(\frac{\Delta\phi}{\omega}\right)} = \omega\left(\frac{\Delta x}{\Delta\phi}\right) \tag{3}$$

where

v = velocity, m/sec

Δx = separation of sensors, m

In Test I the six geophones (Table 3) were grouped into five pairs (c and e, e and g, g and h, h and i, and i and j). The quadrature

spectra and cospectra (see Appendix A) from these five pairs of geophones were averaged before the phase difference was calculated for each frequency. The phase difference results for the 63- and 125-Hz octave band pink noise are presented as the dashed lines in Figure 13a and 13b, respectively. In this figure, the phase difference value was zeroed for frequencies for which the squared coherence was less than 0.4. The solid lines in this figure indicate the phase difference values that could be expected for waves moving with the velocity of sound waves in air and waves moving with the measured Rayleigh wave velocities shown in Figure 9.

66. In Test II, the six geophones were grouped into three pairs (a and d, b and e, and c and f, Figure 2). The phases were calculated from the average cospectrum and the quadrature spectrum of the three pairs of geophones. The phase difference values for Test II are presented in Plates 16-21 for the 40-, 60-, 90-, 135-, and 220-Hz one-third octave bands, as well as for the 25- to 2000-Hz broadband white noise, which was also prerecorded on a cassette tape.

Separation of acoustic-to-seismic coupled signatures

67. By velocity. The time domain signatures as measured by acoustic and seismic sensors (vertical transducers) at location 2 (Figure 1) for the impulse source are presented in Figures 14a and 14b, respectively. The microphone was located 1 m above the ground for this measurement. Other geophones (vertical transducer signatures) not presented here were similar to the signature in Figure 14b except that the trailing pulse indicated in the figure was successively later in time for geophones located successively farther from the source.

68. By coherence. Data from the measurements for determining dependence of acoustic-to-seismic coupling on source type and incident angle were used in this analysis. Figures 15-18 show the seismic and acoustic autospectra and their coherence for data from Test I and Test II. The calculation of coherence is discussed in Appendix A (Equation A10).

Analysis

Dependence of coupling on source type and incident angle

69. Source type. As shown in Table 3, the source types used for measuring the effect of source type on acoustic-to-seismic coupling were pure tones, octave band pink noise, and impulses. Figure 12 presents the computed values of the intensity ratio for these source types including two octave bands (63 Hz and 125 Hz). The speaker height was 2.44 m. As may be seen in Figure 12, the locations of the peaks and dips in the intensity ratio were nearly unchanged (within 5 Hz) despite changes in the source types. However, the magnitude of the peaks of the intensity ratio did vary with the source type used. Table 4 summarizes information for two peaks--one located near 40 Hz, the other located near 90 Hz. The sources are ordered according to increasing bandwidth. For a given peak (near 40 Hz or near 90 Hz), the amplitude of the intensity ratio increases with the increasing bandwidth of the source.

70. Table 4 also presents the measured sound pressure of the source types. There is not a consistent trend between the sound pressure of the sources and the resulting amplitude at the peaks of the intensity ratios. To the extent that the intensity ratio is a measure of the efficiency with which acoustic energy is coupled to the terrain, Table 4 indicates that this efficiency increases with the bandwidth of the source, but that it does not have an identifiable trend of increasing or decreasing with increasing amplitude of the source.

71. Intensity ratios derived using sensors at location 2 (Figure 1) in Tests I and II were compared to examine the extent to which the acoustic-to-seismic coupling phenomenon changed for the two testing periods. Figure 19 shows the intensity ratios for the frequency sweep tests for the 2.44-m speaker height in both Tests I and II. The dominant peaks occur around 40 and 90 Hz and appear in the intensity ratios for both tests, although there is more variation in the "90-Hz dominant peak" for Test II, and it is less apparent than for Test I. Above 140 Hz the intensity ratios differ significantly. For Test I, a

dominant peak occurs around 210 Hz with a dip between 100 and 200 Hz. For Test II, a dominant peak occurs around 150 Hz for Test II with a dip from 160 to 230 Hz. The differences in the intensity ratios between Tests I and II for the higher frequencies might be attributed to the fact that the higher frequencies have shorter wavelengths than lower frequencies. Waves interact with media changes that have dimensions on the order of a wavelength. It is possible that near-surface changes (i.e., within a metre or so of the surface) in soil moisture and vegetation (between Test I in December and Test II in March) may be greater than those changes occurring for the in situ materials at greater depths.

72. It may be conjectured that the peaks in the intensity ratio are induced by irregular frequency response of the geophones so that, for a fixed sound pressure, the geophone is more sensitive to some frequencies than others. However, such an explanation for the peaks in the intensity ratio is implausible since the dominant peaks are sensitive to the angle of incidence of the acoustic waves.

73. The seismic spectra discussed earlier are from geophones placed vertically. With each vertical geophone there are two other geophones in the horizontal plane, one oriented toward the speaker (radial) and the other perpendicular to this (horizontal). Intensity ratio results were also obtained for the radial geophones at location 2 for Test 1. Figure 20 shows the intensity ratio results for the 63-Hz and the 125-Hz octave band. The dominant peaks of the intensity ratio occur in the frequency band between 20 Hz and 40 Hz and at frequencies around 90 Hz. These results are similar to those occurring for the vertical geophone (Figure 12).

74. The frequency dependence of the intensity ratios shows that the acoustically induced component of the seismic signature is distorted by the acoustic-to-seismic coupling phenomenon. As a result, the seismic signatures of acoustic targets such as aircraft are not faithful reproductions of their acoustic signature. Furthermore, the acoustic component of the signature induced by ground targets, such as that of a cylinder firing of a vehicle, may be enhanced or suppressed relative to remaining portions of the signature. In both instances, detection and

classification algorithms using the coupled signatures will be affected. The increased efficiency of coupling for sources having energy over broader frequency bands implies that, for the same sound pressure, broadband sources such as jet aircraft will provide a greater threat of masking desired signatures than will narrow-banded sources, such as acoustic components from vehicle traffic.

75. Incident angle. The results of the investigation of the dependence of the intensity ratio spectrum on the incident angle of acoustic energy showed a shifting of the peaks and dips as a function of speaker height for frequencies below approximately 200 Hz. Such shifting is illustrated in Figure 21, which presents the intensity ratios for the 40-Hz, one-third octave band for five different speaker heights. The brackets identify the dominant peaks of the intensity ratios and serve to show that the dominant peaks shift to lower frequencies as the speaker is raised. The speaker heights and the corresponding direction of incidence (as defined by the angle γ, Figure 22) for the sensors used for measurements to determine the intensity ratio are tabulated below:

Speaker Height, m	Angle γ, deg
1.0	5.7
2.4	14.0
5.0	28.6
7.5	43.0
10.0	45.0

76. An estimate of the magnitude of the frequency shift among the intensity ratios in Figure 21 was obtained by calculating the cross-correlation between the intensity ratio for the lowest speaker height (1 m) and that of each of the higher speaker heights. The frequency corresponding to the peak of the cross-correlation function can be used as an estimate of the frequency shift between intensity ratios.

77. Before making a cross-correlation calculation, the intensity ratios were zeroed outside of the regions (identified by the brackets in Figure 21) of the dominant peaks in the signature spectra of the intensity ratio. The results of the computation of the frequency shift are presented in Figure 22, where changes in speaker height are

represented as changes in the angle γ. Although a similar analysis was not made for the higher one-third octave bands (i.e., 90 and 220 Hz), similar frequency shifts in the dominant peaks of the intensity ratios for the 90-Hz one-third octave band can be observed. For example, Plates 8, 11, and 14 show a dominant peak for the 90-Hz, one-third octave band centered at 85 Hz, 80 Hz, and 78 Hz for speaker heights of 5.0, 7.5, and 10.0 m, respectively. However, for frequencies of 250 Hz or greater, the frequency shift due to changes in speaker height, if it exists, is not nearly so evident as for the lower frequencies. This may be seen by comparing the frequency location of the dominant peaks (centered around 330 Hz) in Plates 3, 6, 9, 12, and 15. There is no obvious trend to suggest that the dominant frequencies of the intensity ratio change with speaker height for the higher frequencies (i.e., exceeding 250 Hz).

78. The fact that the coupling at each frequency depends on the angle of incidence is important. For example, when overflying aircraft could be a source of background noise, the frequencies coupled to the ground from aircraft vary as a function of the aircraft-sensor geometry. Therefore, aircraft detection and classification information derived from low frequencies (i.e., less than 250 Hz) is affected by such dependence. In addition, the masking of other signatures by aircraft noise is also affected by the aircraft-sensor geometry.

Velocity of propagation of acoustic-to-seismic coupled signatures

79. Inspection of the results of the velocity of propagation for Test I (Figure 13) and Test II (Plates 16-21) shows that this velocity is very near the velocity of sound in air. Some points of interest in the Test II results follow. Despite the fact that the phase information is extracted from different tests, the structure (i.e., peaks and dips) of the phase-difference curves above 30 Hz is very similar for each plot for which frequency overlap in such phase-difference curves occur. For example, the peak at 95 Hz, dip at 120 Hz, and peak at 145 Hz occurs for the 40-Hz (Plate 16), 60-Hz (Plate 17), 90-Hz, (Plate 18), and

135-Hz (Plate 19) one-third octave bands. These peaks and dips suggest that consistent deviations from the "constant" acoustic velocity may occur. Alternatively, the phase response of the instrumentation might be questioned, although it would seem unlikely that the average values from five geophones would converge in such a repeatable pattern for each test.

80. The phase differences in the 20- to 80-Hz frequency range are, in general, somewhat smaller than would be expected for the acoustic velocity (Plate 16). The smaller phase differences suggest that the energy was moving with a somewhat faster velocity in this frequency range than the acoustic velocity (since smaller phase differences imply shorter travel times). However, this may be due to the fact that the amplitude of the background noise in this frequency range was somewhat competitive with that of the ground motion induced by the source because of the presence of the roadway (approximately 220 m northwest of Porter's Chapel Road, paragraph 37). Inasmuch as the direction of arrival of propagating signatures from Porter's Chapel Road was not parallel to the line of the geophones used for the velocity calculation, the spacing of the geophones was effectively less for such signatures; hence the signatures would appear to be traveling with higher velocities then they actually were. The combination of such background noise with the signature induced by the source could effectively increase the velocity measured, using the geophone configuration in Figure 1. In summary, this analysis shows that the velocity of propagation of acoustic-to-seismic coupling energy is close to the velocity of sound in air.

Separation of seismic signature components

81. As noted in paragraphs 8 and 9, two potential techniques for separating the acoustic-to-seismic coupled component of the seismic signature from the component induced by surface contact were investigated. In order for these techniques to be applicable, it must be demonstrated that:

a. The predominant portion of the component of the signature induced by an acoustic wave moving parallel to the surface moves at or near the velocity of sound in air.

b. For an acoustic source, there exists a high degree of correlation between the microphone and geophone measured signatures.

To address the first requirement, an impulsive source was used so that time of arrival of the acoustic-to-seismic coupled signature could be used to compare the velocity of propagation with the acoustic signal. For evaluating the extent to which the second requirement was met, the correlation between microphone and geophone signatures was determined using coherence.

82. Separation using velocity of propagation. The appearance of the time domain seismic and acoustic signature resulting from the impulsive source was very similar, and therefore most of the seismic signature can be considered closely correlated with the acoustic signature. Further, the dominant peak of the seismic signature arrived at exactly the same time as the acoustic signature. To investigate the possibility that the trailing pulse in the seismic signatures contained information obscured in the dominant peak, a comparison of the velocity of the trailing pulse with acoustic and seismic surface wave velocities was made. The seismic wave velocity of the trailing pulse was made by zeroing out the time domain signatures up to the trailing pulse for two signals measured by geophones separated by 0.75 m (see Figure 23). Then, phase differences between these two signatures were calculated. The resulting phase-difference plot (Figure 24) shows that the velocity of the trailing pulse is less than the acoustic but greater than the Rayleigh wave velocity. Perhaps the trailing pulse can be associated with the wave form discussed by Jardetsky and Press.[4] They investigated acoustic-to-seismic coupled waves induced by an impulsive acoustic point source over a layered solid (one layer over an infinite half-space). They give a general expression for the dispersion curve of the induced Rayleigh wave for a particular condition (Poisson's ratio = 0.25 for both layers). However, they do not present theoretically derived calculations of the amplitudes of the seismic wave induced by acoustic

waves because of the numerical difficulties encountered in obtaining such results. For instances for which the velocity of the Rayleigh wave is less than the acoustic velocity, the researchers show that, in addition to the usual waves (compression, shear, and Rayleigh waves) induced in terrain by surface disturbances, a wave form can occur that has dispersive properties different from the Rayleigh wave. The latter wave form results in a seismic signature from an impulse source that has an approximately constant frequency wave train arriving at a time corresponding to the arrival of the acoustic wave and lasting for a time dependent on the distance to the source and the shear and compression properties of the medium.

83. Separation using coherence techniques. Figure 15 presents the autospectra for the seismic and acoustic signatures (for the 63- and 125-Hz octave bands) used for a calculation of correlation at each frequency (coherence). The seismic autospectra for both octave bands contain a considerably higher precentage of power in the 0- to 40-Hz region than do the acoustic autospectra in the same region. This power can be attributed to background noise from traffic, wind noise, etc., within a kilometre of the data collection site. The acoustic spectra also have a discernible amount of power below 40 Hz that can likely be associated both with background traffic noise and small amounts of wind noise.

84. The squared coherence was computed (see Appendix A) to provide a measure of the correlation at each frequency between the seismic and acoustic signatures. The resulting computations for Test I are presented in Figures 16a and 16b for the 63- and 125-Hz octave bands, respectively. The squared coherence is high (i.e., exceeds 0.6) for most of the acoustic source frequency regions (45-90 Hz in Figure 16a and 90-180 Hz in Figure 16b). In fact, the squared coherence remains high, even though the acoustic power is low for frequencies above 90 Hz for the 63-Hz octave band source. This indicates that the signal level is above the random noise level (induced by the electronics and background noise) despite the low power level of the source. However, the squared coherence is generally below 0.6 for frequencies below 40 Hz,

even though both the acoustic and seismic power are discernible in the autospectra in this frequency region.

85. The coherence between seismic and acoustic signals in the source frequency range was very high (greater than 0.9) using the one-third octave band pink noise sources of Test II. An example of this is shown in Figures 17 and 18 for the 40- and 90-Hz one-third octave bands with a 2.44-m speaker height and sensors at the 10-m location. Figure 17 shows the autospectra for the measured seismic and acoustic signals, and Figure 18 shows the coherence between the seismic and acoustic signals for the two sources in Figure 17.

86. The coherence between the seismic and acoustic signatures for the seismic component induced by the acoustic source (thereby attributable to acoustic-to-seismic coupling) suggests that a signal processing technique could be implemented to remove the component, allowing better detection of the propagating seismic energy induced by surface contact of an intruder. The signal processing technique would consist of the monitoring of the coherence between the seismic and acoustic signatures. When the power of the seismic signature is at a sufficient level appropriate for an intruder, the coherent signature components could be subtracted from the noncoherent components and the resultant signature processed by the sensor logic for intruder detection.

Theoretical Results

87. As noted in paragraph 6, little has been done to quantify the interaction between acoustic and seismic wave forms. In this study, an effort was made to use plane wave theory to derive the intensity ratio for the microphone-geophone geometry used in the field data collection. A simplified description of the interaction between an incident compression wave impinging on a flat surface over infinitely deep, homogeneous ground is illustrated in Figure 25. When a compression wave is incident on the surface of a solid medium, two kinds of waves are transmitted into the solid--compression waves and vertically polarized shear waves. The directions of propagation of the incident and reflected

compression waves in air and the transmitted compression and shear waves in the ground are identified by the angles γ , γ , γ' , and δ' , respectively, as shown in the figure.

88. A theoretical description relating the amplitudes and phases of the reflected and transmitted waves to the amplitude and phase of the incident wave is presented in Appendix C. The assumptions made in this derivation were:

a. The ground surface is perfectly flat and the motion of air over the surface (i.e., caused by pressure differentials induced by the source) is frictionless. That is, the horizontal component of stress (x-direction in Figure 25) vanishes at the interface ($z = 0$).

b. The ground consists of infinitely deep, homogeneous material (no layering).

c. Air is a perfect liquid (i.e., has no shear strength).

89. To derive the relation between the amplitude and phase of the incident wave and the refracted waves, boundary conditions specifying continuity of vertical displacement and vertical stresses of the air and soil surface at the interface are applied. However, slippage is allowed between the ground surface and the air (i.e., the horizontal displacements of the ground at the surface are not the same as those of the air at the surface). The existence of slippage at the surface is reasonable, since air is assumed to have no shear strength.

90. The medium properties used to compute the reflection and transmission coefficients (i.e., coefficients defining percent of amplitude reflected or transmitted and appropriate phase) were:

α = compression wave velocity in air, 340 m/sec

α' = compression wave velocity in the soil, 340 m/sec

β' = shear wave velocity in the soil, 160 m/sec

ρ = density of air, 1 kg/m^3

ρ' = density of soil, 2×10^3 kg/m^3

The compression and shear wave velocity measurements in the soil are approximate values for the top layer measured during Tests I and II (Table 2).

91. The theoretical reflection and transmission coefficients for

an incident compression wave in air are derived in Appendix C and are given by:

Reflected compression wave

$$\frac{-\rho a' c^4}{\beta'^2} + \frac{\rho' \beta'^2 a \left[(c^2/\beta'^2 - 2)^2 + 4a'b' \right]}{\rho' \beta'^2 a \left[(c^2/\beta'^2 - 2)^2 + 4a'b' \right]} \tag{4}$$

Transmitted compression wave

$$\frac{2\rho a c^2 (c^2/\beta'^2 - 2)}{\rho a' c^4/\beta'^2 + \rho' \beta'^2 a \left[(c^2/\beta'^2 - 2)^2 + 4a'b' \right]} \tag{5}$$

Transmitted shear wave

$$\frac{4\rho a a' c^2}{\rho a' c^4/\beta'^2 + \rho' \beta'^2 a \left[(c^2/\beta'^2 - 2)^2 + 4a'b' \right]} \tag{6}$$

where c is the apparent velocity of the incident compression wave along the direction of the boundary (x-direction) (paragraph 6 of Appendix C) and a, a', and b' are functions of c and the velocities α, α', or β'. As shown in Appendix C, a' and b' can be either real or imaginary numbers.

92. The apparent velocity c is related to the direction of the incoming plane wave by the relation

$$c = \frac{\alpha}{\cos \gamma} \tag{7}$$

The directions of the refracted shear and compression waves are constrained by the fact that the refracted waves have the same apparent velocity when leaving the boundary as that of the incident compression

wave. Therefore, the following relations hold:

$$c = \frac{\alpha}{\cos \gamma} = \frac{\alpha'}{\cos \gamma'} = \frac{\beta'}{\cos \delta'} \tag{8}$$

Since the maximum value of the cosine is unity, the above relations can be satisfied only for selected ranges of γ , γ' , and δ' . For the compression and shear wave velocities presented in paragraph 90, the relations can be satisfied only for values of δ' from 61.9 to 90.0 deg (as γ varies from 0.0 to 90.0 deg).

93. The expressions for the reflection and transmission coefficients presented in paragraph 91 can be used to calculate the particle displacement or velocity in the ground for a given amplitude of particle displacement or velocity in the air. However, field measurements of air pressure, not particle velocity, have been obtained. As shown in Appendix C, pressure (P) can be related to particle velocity (v) by the relation $P = \rho \alpha v$.

94. Using the above relation and the coefficients in paragraph 91, the intensity ratio can be computed. To compare the measured intensity ratio with the theoretically computed one, the geometry of the field measurements (i.e., location of the microphone and geophone relative to the boundary between the air and soil) must be taken into account in the computations. For such computations, it is assumed that the geophones measure the particle velocity at the boundary. However, the height of the microphone above the ground surface was varied during the tests (Table 3). Therefore, it was necessary to include microphone height as a variable in the derivation of the intensity ratio. The resulting expression for the intensity ratio is quite lengthy and is presented in Equations C55 and C56 of Appendix C. The theoretical expression for the intensity ratio is independent of frequency, if the microphone is on the ground ($z = 0$).

95. The computed intensity ratio as a function of direction of incidence of the acoustic wave, using the compression and shear wave velocities and densities in paragraph 90, is presented in Figure 26 for the microphone on the ground. The computed intensity ratio is

independent of frequency for the microphone on the ground. The amplitude of the intensity ratio is very sensitive to the direction of incidence of the acoustic wave. The intensity ratios for a microphone height of 1 m are presented in Plates 22-26 for directions of incidence corresponding to angles, γ, of 5, 15, 25, 35, and 45 deg, respectively. Because of destructive interference between the direct and reflected waves received at the microphone, the computed amplitude approaches zero for some frequencies, with the result that the intensity ratio approaches infinity. The curves indicating the amplitude of the intensity ratios as a function of frequency in Plates 22-26 are broken in the frequency regions in which intensity ratio becomes too large due to such interference.

96. In order to limit the discussion of the differences between the measured and computed intensity ratios, only measured intensity ratios below 80 Hz were compared with computed intensity ratios. Although a broader range of frequencies could have been included, the region below 80 Hz provides sufficient data for discussion of the significant differences between the measured and computed intensity ratios. Figure 26 presents the computed intensity ratios for direction of incidence below 80 deg. For the direction of incidence for which $\gamma \approx 14.0$ deg (i.e., speaker height is 2.44 m), the computed intensity ratio (Figure 26) is approximately 0.00007 (in units of $(10^{-3}$ cm/sec/μbar$)^2$). The measured intensity ratio for this speaker-sensor geometry is frequency-dependent (Plate 4) and varies from 0.0002 to 0.005 (same units). Therefore, the measured intensity ratio is from 2.5 to 62.5 times larger than the computed value, depending on frequency. Since the intensity ratio is proportional to the square of the ratio of the amplitude of the seismic wave to the amplitude of the sound pressure, the measured amplitude of the seismic wave would be between 1.2 and 7.9 times larger than the computed amplitudes for the same sound pressure. For a larger angle γ of 45 deg (i.e., speaker height of 10 m), the computed intensity ratio is 0.0004. In this case, the measured amplitude of the seismic wave would be between 0.7 and 3.2 times larger than the computed amplitudes for the same sound pressure.

97. There are several deficiencies apparent in the theoretical treatment using plane waves to describe the acoustic-to-seismic coupling phenomenon. Among these deficiencies are:

a. The measured intensity ratios for the microphone on the ground surface are functions of frequency, whereas the computed intensity ratios are not.

b. The amplitude of the predominant peaks of the measured intensity ratios are not very sensitive to the direction of incidence of the acoustic wave, whereas the computed intensity ratios are very sensitive to such changes. For example, the intensity ratios for the dominant peaks identified in Figure 21 are assumed values between 0.04 and 0.06. However, for the same range in values of γ (from 5.7 to 45 deg), the computed intensity ratio varies from 0.00003 to 0.0004.

c. The computed intensity ratio is from 0.7 to 62.5 times smaller than that of the measured intensity ratios (i.e., for the discussed intensity ratios below 80 Hz.)

98. The deficiencies of the theoretical treatment using plane wave theory can be related, at least in part, to the assumptions listed in paragraph 88. The assumptions that ground surface is flat and that the horizontal component of the stress vanishes in soil at the surface is particularly questionable. The fact that the intensity ratio for the measured data is rather insensitive to the direction of incidence of the sound may be the acoustic-to-seismic analog of the air-ocean results observed by Lubard and Hurdle.[5] They made measurements of acoustic transmission from a source in air to a hydrophone in a wind-roughened ocean. They showed that more energy reaches the hydrophone for a rough ocean than predicted by the smooth surface theory, with the excess increasing for decreasing angle between the acoustic wave and the water surface. They also found that the efficiency of transmission of energy from air to the ocean increased with increasing frequency and was independent of the height of the source above the ocean surface.

99. The frequency dependence of the acoustic-to-seismic coupling at the boundary is not accounted for using plane wave theory with homogeneous half-spaces. To incorporate physical factors that will introduce frequency dependence into a theoretical formulation, it would be desirable to include layering effects in the soil half-space and a

description of the spatial distribution of surface roughness (including the effects of surface vegetation and topography).

100. Perhaps the theoretical treatment can best be served by an improved analysis of the character of the particle motion in the soil. Two unanswered questions about the nature of the particle motion induced by acoustic-to-seismic coupling are:

a. Is the nature of the soil vibrations near the surface induced by the acoustic energy the same as it is one or two metres beneath the surface?

b. Are there consistent phase or amplitude relations between the vertical and horizontal components of ground motion?

PART IV: CONCLUSIONS AND RECOMMENDATIONS

Conclusions

101. As identified in the approach (paragraph 7), the measured data were to be used to:

a. Evaluate the theoretical model used to predict acoustic-to-seismic coupling.

b. Identify factors influencing acoustic-to-seismic coupling.

c. Evaluate two techniques for separating the acoustic-to-seismic coupled signal from that part of the seismic signal induced by surface contact.

102. Conclusions pertaining to a, b, and c above follow:

a. Evaluation of theoretical model. The plane wave model that was investigated was not satisfactory in predicting the amplitude of the intensity ratio as a funciton of the angle of incidence or as a function of frequency (paragraph 97).

b. Properties of acoustic-to-seismic coupling and factors affecting their characteristics.

(1) The velocity of propagation as determined from the octave band pink noise sources was very near the velocity of sound in air (paragraph 79).

(2) The frequencies at which peaks and dips occur in the intensity ratio do not depend on the type of source used (i.e., they are independent of source amplitude and bandwidth) (paragraph 69).

(3) The amplitude of the peaks of the intensity ratio increases with increasing bandwidth of the source (paragraph 70).

(4) There is a shift to lower frequencies for the frequencies at which peaks and dips occur in the intensity ratio due to a change of incident angle caused by increasing the source height (paragraph 75).

(5) The intensity ratio results were repeatable for frequencies below approximately 140 Hz for measurements taken at two different times of the year (March and December) (paragraph 71).

c. Separation of seismic signatures. Separation using velocity of propagation required that the acoustic-to-seismic coupled signature travel with a velocity near the velocity of sound in air. Although the impulse

signature could be separated into parts traveling with different velocities (paragraph 82), most of the energy of the acoustic-to-seismic coupled signal arrived at the same time as the sound wave in air. Therefore, it appears that such separation can be implemented if the seismic velocities are different from the acoustic velocity. Separation using coherence techniques also seems a viable method, since the measured data showed there was good coherence between the seismic and acoustic signatures in the frequency range of the source (paragraphs 84 and 85).

Recommendations

103. The recommendations addressing a, b, and c (paragraph 101) are:

a. Evaluation of theoretical model. Since the plane wave treatment used in this study did not adequately model experimental conditions, an additional investigation is needed to develop ways to predict acoustic coupling for most naturally occurring seismic conditions.

b. Identification of factors influencing acoustic-to-seismic coupling. Similar tests for looking at the intensity ratio spectrum should be run for other seismic conditions (i.e., different layering, different seismic velocities, different surface cover).

c. Separation of seismic signatures. Separation of the seismic signature using velocity of propagation and coherence analysis should be evaluated in different acoustic and seismic environments. An analysis of the feasibility of implementing sensor configurations and algorithms to exploit such separation tehcniques should be conducted.

REFERENCES

1. Cress, D. H., "Terrain Considerations and Data Base Development for Design and Testing of Devices to Detect Intruder-Induced Ground Motion," Technical Report M-78-1, May 1978, U. S. Army Engineer Waterways Experiment Station, CE, Vicksburg, Miss.

2. Lundien, J. R. and Nikodem, H., "A Mathematical Model for Predicting Microseismic Signals in Terrain Materials," Jun 1973, U. S. Army Engineer Waterways Experiment Station, CE, Vicksburg, Miss.

3. Kinsler, L. E. and Frey, A. R., Fundamentals of Acoustics, John Wiley and Sons, Inc., New York, 1962.

4. Jardetsky, W. S. and Press, F., "Rayleigh-Wave Coupling to Atmospheric Compression Waves," Bulletin, Seismological Society of America, Vol 42, 1952, pp 135-144.

5. Lubard, S. C. and Hurdle, P. M., "Experimental Investigation of Acoustic Transmission From Air Into a Rough Ocean," Journal, Acoustical Society of America, Vol 60, No. 5, Nov 1976, p 1048.

6. Embleton, T. F. W., Piercy, J. E., and Olson, N., "Outdoor Sound Propagation Over Ground of Finite Impedance," Journal, Acoustical Society of America, Vol 59, 1976, pp 268-277.

7. Donato, R. J., "Propagation of a Spherical Wave Near a Plane Boundary with a Complex Impedance," Journal, Acoustical Society of America, Vol 60, 1976, pp 34-39.

8. Piercy, J. E. and Sutherland, L. C., "A Review of Noise Propagation in the Atmosphere," unpublished (April 1976).

9. Morse, Philip M. and Ingrad, Umo K., Theoretical Acoustics, McGraw-Hill, New York, 1968.

10. Ewing, W. M., Jardetsky, W. S., and Press, R., Elastic Waves in Layered Media, McGraw-Hill, New York, 1957, Chapter 3.

11. Olson, H. F., Accustical Engineering, D. Van Nostrand Company, Inc., Princeton, New Jersey, 1957, Chapter 1.

12. West, H. W. "Effects of Environment on Microseismic Wave Propagation Characteristics in Support of SID Testing at Fort Bragg, N. C.," Technical Report M-73-2, Jun 1973, U. S. Army Engineer Waterways Experiment Station, CE, Vicksburg, Miss.

13. Dickinson, P. R. and Doak, P. E., "Measurements of the Normal Acoustic Impedance of Ground Surface," Journal, Sound Vibrations, Vol 13, 1970, pp 309-322.

14. Piercy, J. E. and Embleton, T. F. W., SAE Transactions, Sec. 1, Vol 83, 1976, pp 83, 928.

15. Embleton, T. F. W., "Sound Propagation in Homogeneous Deciduous and Evergreen Woods," Journal, Acoustical Society of America, Vol 35, 1963, pp 1119-1125.

16. Aylor, D., "Noise Reduction by Vegetation and Ground," Journal, Acoustical Society of America, Vol 51, 1972, pp 201-209.

17. Bolen, L. N., Bass, H. E., and Lucy, E., "Sound Attenuation over Homogeneous Ground Cover," Journal, Acoustical Society of America, Vol 56, 1974, p 524.

18. Pao, S. P. and Evans, L. B., "Sound Attenuation over Simulated Ground Cover," Journal, Acoustical Society of America, Vol 49, 1971, p 1069.

19. Chessell, C. I., Journal, Acoustical Society of America, Vol 62, 1977, p 825.

Table 1

Characterisitics of Octave and 1/3-Octave Band Pink Noise

Source	Center Frequency, Hz	Half-Power Points, Hz
Octave band pink noise	63	44, 88
	125	88, 177
	250	177, 354
	500	354, 707
	1000	707, 1414
1/3-octave band pink noise	25	22, 28
	40	36, 45
	60	53, 67
	90	63, 80
	135	120, 152
	220	196, 247
	440	392, 494
	880	784, 988
	1760	1568, 1976

Table 2

Compression and Shear Wave Velocities for Test Site

			Compression Wave			Shear Wave		
Test	Location	Refraction Line	Layer No.	Layer Depth, m	Velocity m/sec	Layer No.	Depth, m	Velocity m/sec
I	1	1	1	0.00-6.30	350	1	0.00+	150
			2	6.30+	2040			
		2	1	0.00-6.90	340	1	0.00+	153
			2	6.90+	2000			
I	2	1	1	0.00-6.10	340	1	0.00+	153
			2	6.10+	1830			
		2	1	0.00-5.30	340	1	0.00+	159
			2	5.30+	1150			
I	3	1	1	0.00-6.10	340	1	0.00+	159
			2	6.10+	1525			
		2	1	0.00-5.30	340	1	0.00+	160
			2	5.30+	1160			
II	2	1	1	0.00-5.30	350		(no data)	
			2	5.30+	950			

Table 3

Summary of Measurements

	Test I						Test II					
		Sensors						Sensors				
		Microphones			Geophones			Speaker	Microphones			Geophones	
Measurement	Source Type*	Type	Symbol,** Location	Height m(in.)	Symbol,** Location	Axes	Source Type	Height, m	Type	Symbol,** Location	Height, m	Symbol,** Location	Axes†
Dependence of coupling on source type and incident angle	Sweep 20-300 Hz 2 Hz/sec	B&K	B,30 m	1.0 (39.4)	d,30 m	Vertical	Log sweep 20-700 0.5 decades/min	2.44	B&K	B,30 m	0	g,30 m	Vertical
	Octave band pink noise	B&K	A,30 m	0	d,30 m	Vertical and radial	1/3-octave band pink noise	1,2.44, 5, 7.5, 10 m	B&K	A,10 m	0	d,10 m	Vertical
								2.44	B&K	B,30 m	0	g,30 m	Vertical
	Impulse	B&K	B,30 m	1.0 (39.4)	d,30 m	Vertical			(Impulse not processed)				
Velocity of propagation of acoustic-to-seismic coupled signatures	Octave band pink noise		N.A.		c,28.5 m e,30.0 m g,31.5 m h,33.0 m i,34.5 m j,36.0 m	Vertical	1/3-octave band pink noise and broad band white noise	1, 2.44, 5, 7.5, 10 m		N.A.		a, 9.25 m b, 9.25 m c, 9.25 m d,10.00 m e,10.00 m f,10.00 m	Vertical
Separation of seismic signatures													
by velocity	Impulse		N.A.		b,28.50 m c,29.25 m d,30.00 m e,30.75 m f,31.50 m g,31.25 m	Vertical			(Data were not analyzed)				
by coherence technique	Octave band pink noise	B&K	A,30 m	0	d,30 m		1/3-octave band pink noise	1, 2.44 5, 7.5, 10 m	B&K	B,30 m	0	g,30 m	Vertical
Coherence length, lateral	Band limited white noise 45-1800 Hz	B&K	B,30 m	0.91 (36)	N.A.	N.A.	Band limited white noise 45-1800 Hz	2.44 m	B&K	I,30 m	1.26	N.A.	N.A.
		B&K	B-H,30 m	0.91 (36)					B&K	D,30 m	1.26		
		B&K	I-L,30 m	0.91 (36)					B&K	E,30 m	1.26		
		B&K	D,60 m	0					B&K	F,30 m	1.26		
		B&K	M-P,60 m	0									
		B&K	Q-T,60 m	0									
Coherence length, radial	Octave band pink noise	B&K	A,30 m	0			1/3-octave band pink noise		B&K	B,30 m	0	N.A.	N.A.
		B&K	D,60 m	0					B&K	C,60 m	0		
Ground surface impedance	Pure tones at octave band intervals 25, 50, 100... 1600 Hz	B&K	A,30 m	0.0-0.76 (0-30)	N.A.	N.A.	1/3-octave band pink noise and broadband white noise	2.44 m	GR	G,10 m	0	N.A.	N.A.
		B&K	B,30 m	0.91-1.68 (36-66)					B&K	H,20 m	0.91		
									B&K	I,30 m	0.91		
									B&K	J,40 m	0.91		
		B&K	D,60 m	0.0-0.76 (0-30)					B&K	K,43 m	0.91		
									B&K	L,50 m	0.91		
		B&K	U,60 m	0.91-1.68 (36-66)					B&K	M,60 m	0.91		
									B&K	N,63 m	0.91		
	Octave band pink noise	GR	V,10 m	0									
		B&K	A,30 m	0									
		B&K	D,60 m	0									

* Speaker at 2.44 m for all Test I measurements.

** Symbols are from Figure 1 (Test I) and Figure 2 (Test II).

† Radial geophone signals were measured but not analyzed.

Table 4

Peak Intensity Ratio Values for Frequencies Below 100 Hz

Test	Source Type	Frequency at Peak Hz	Intensity Ratio, v^2/p^2 $(10^{-3}$ cm/sec/μbar$)^2$	Sound Pressure μbars
I	Sweep (linear)	39	9.31×10^{-3}	1.3
		94	2.47×10^{-3}	1.8
	Octave band pink noise 63-Hz band	39	0.79	3.2×10^{-1}
		92	0.13	5.5×10^{-1}
	125-Hz band	92	0.20	4.0×10^{-2}
	Impulse	39	2.6	7.2×10^{-2}
		92	1.5	9.1×10^{-2}
II*	Sweep (logarithmic)	39	5.41×10^{-3}	1.8
		93	8.32×10^{-4}	2.3
	1/3-octave band noise 40-Hz band	39	8.0×10^{-2}	1.4×10^{-1}
	90-Hz	92	6.0×10^{-3}	3.6×10^{-1}
	Impulse (not evaluated)			

* Speaker height is the same as for Test I (i.e., 2.44 m).

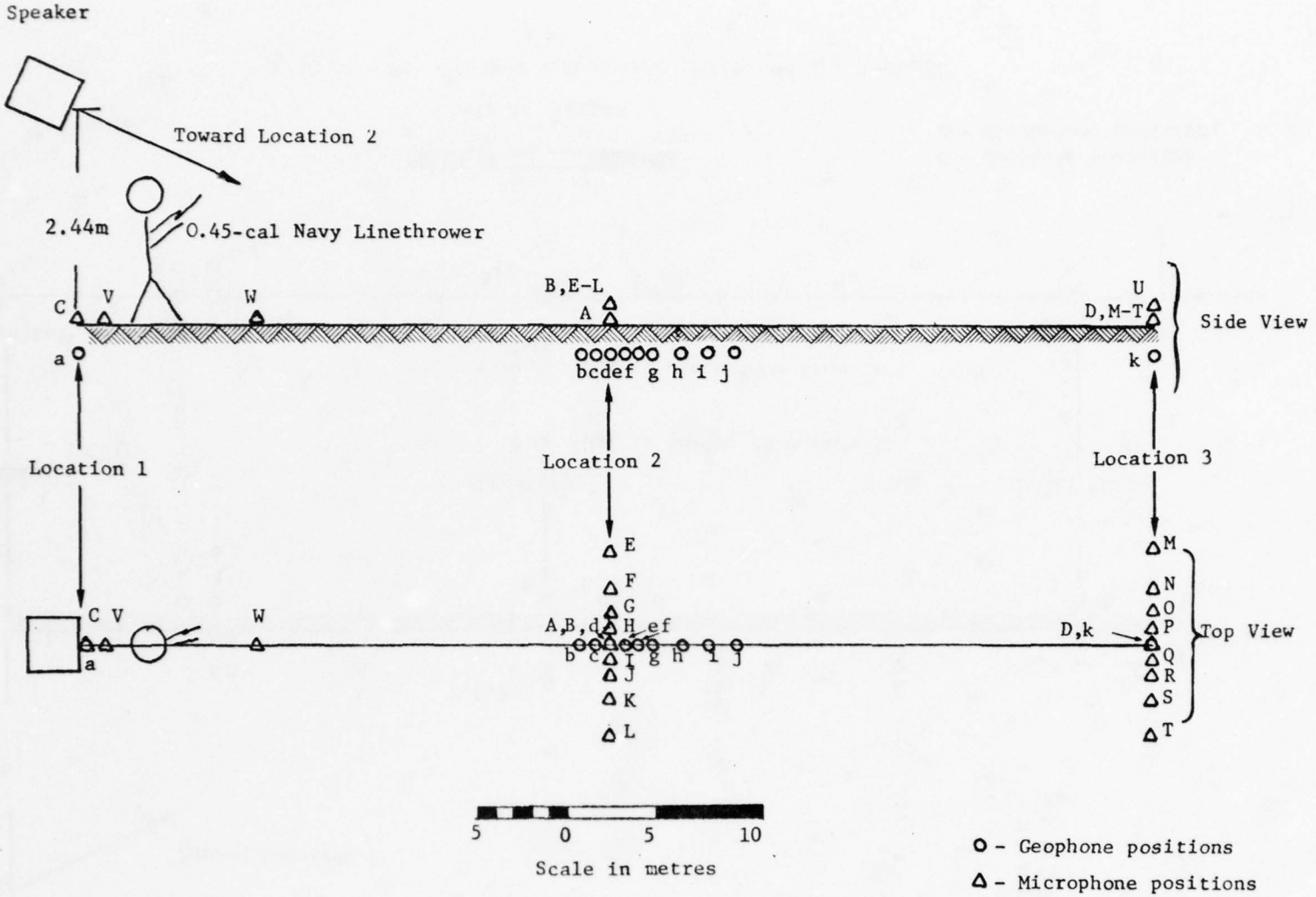

Figure 1. Speaker and sensor positions for Test I

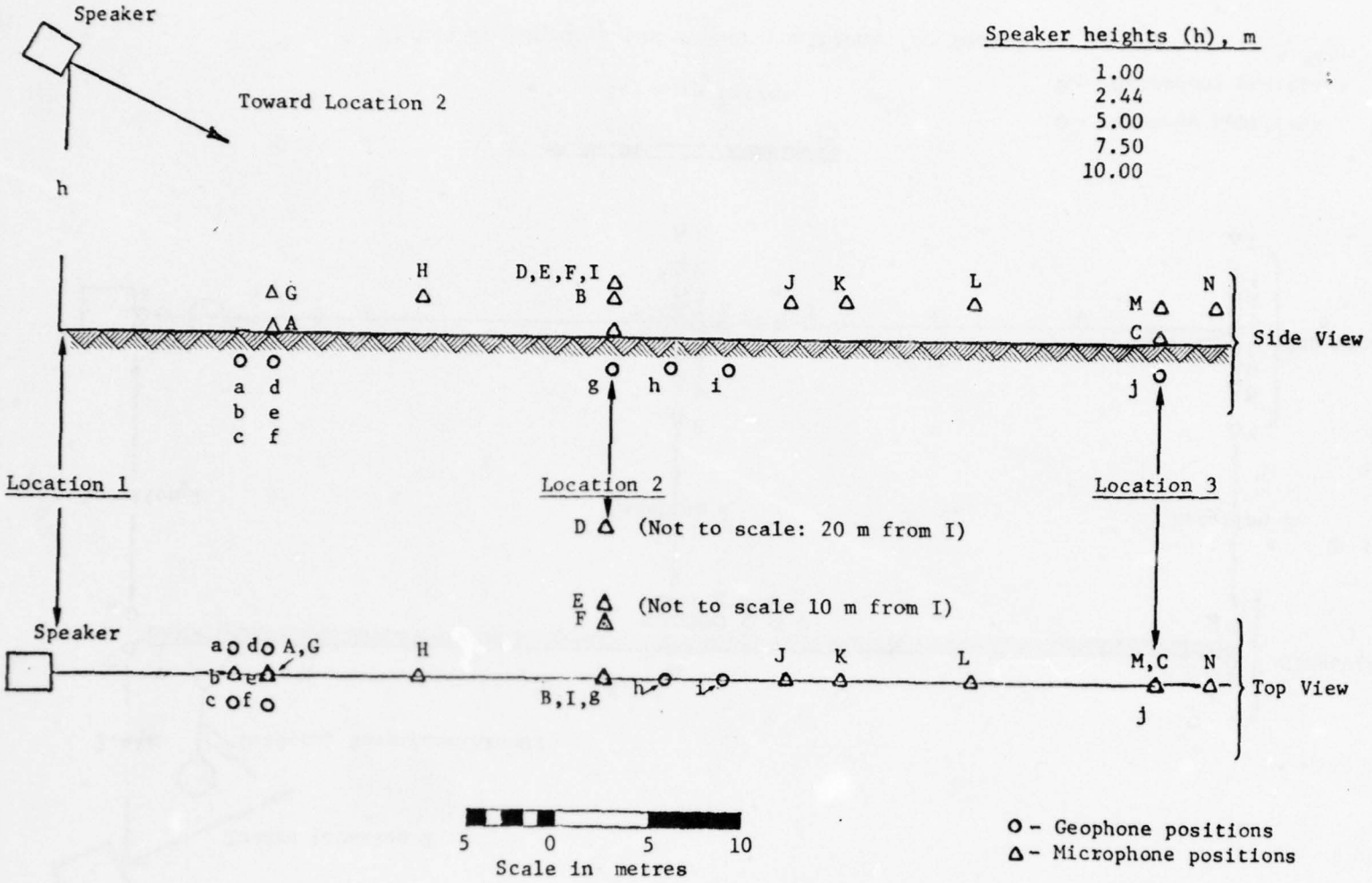

Figure 2. Speaker and sensor positions for Test II

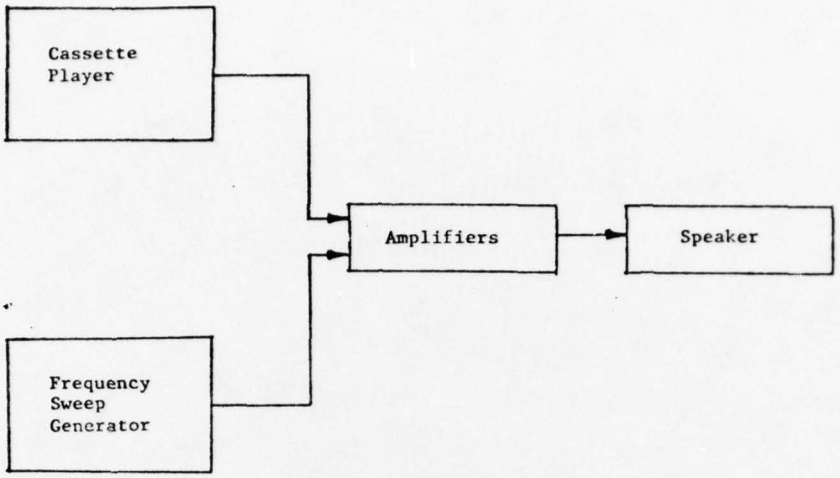

a. Speaker system

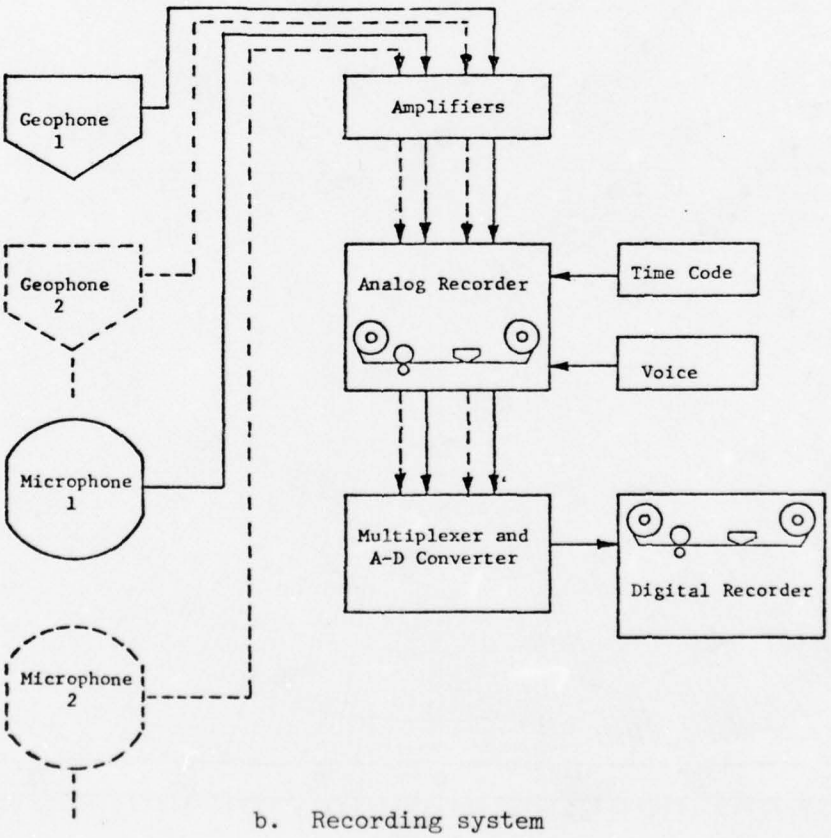

b. Recording system

Figure 3. Speaker and recording systems for experimental program

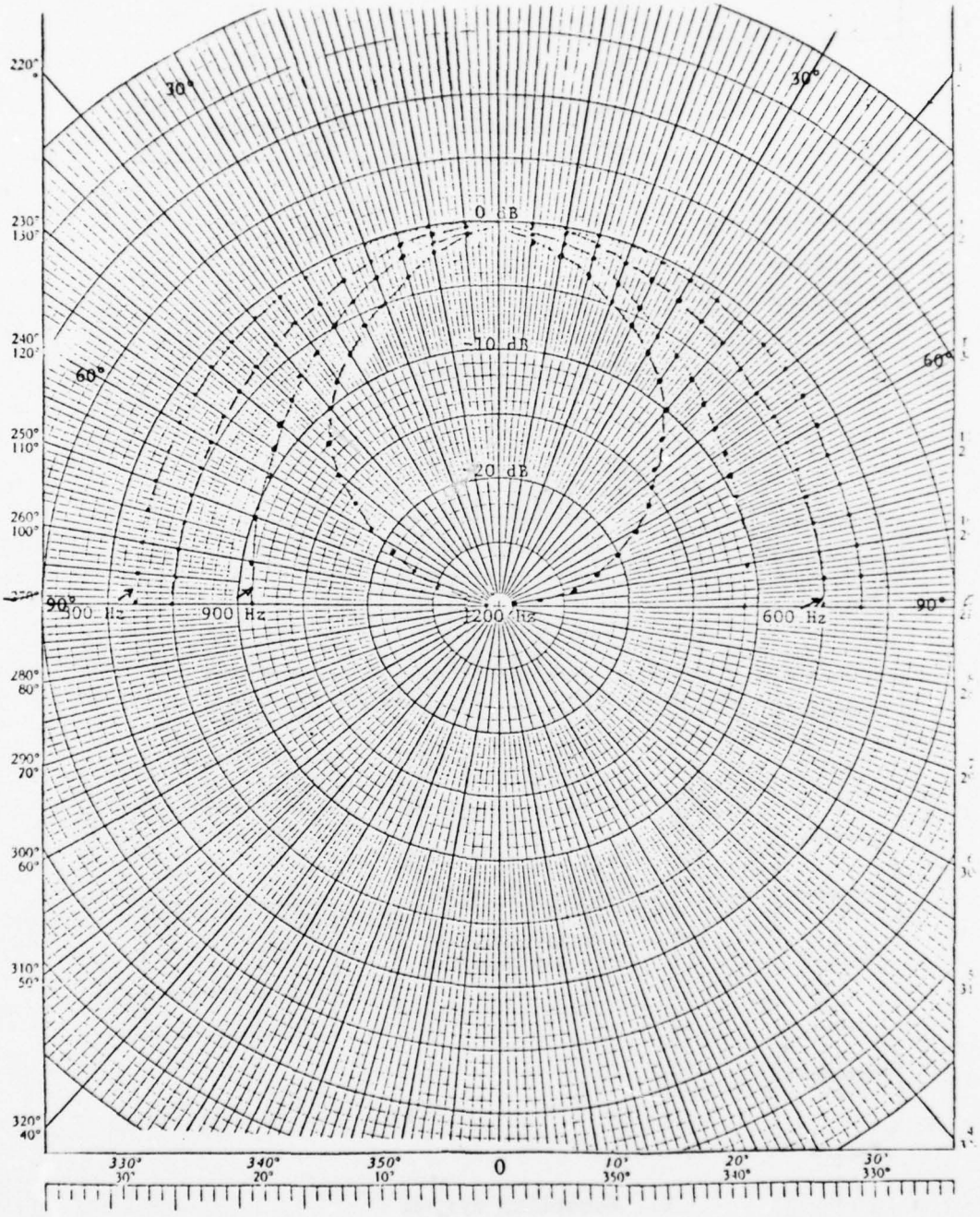

Figure 4. Directivity pattern of speaker

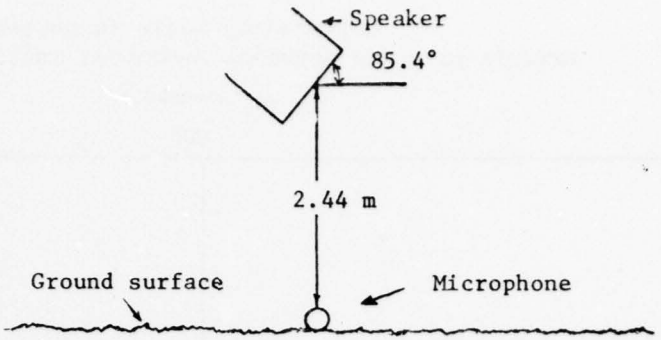

a. Speaker and microphone positions for frequency response

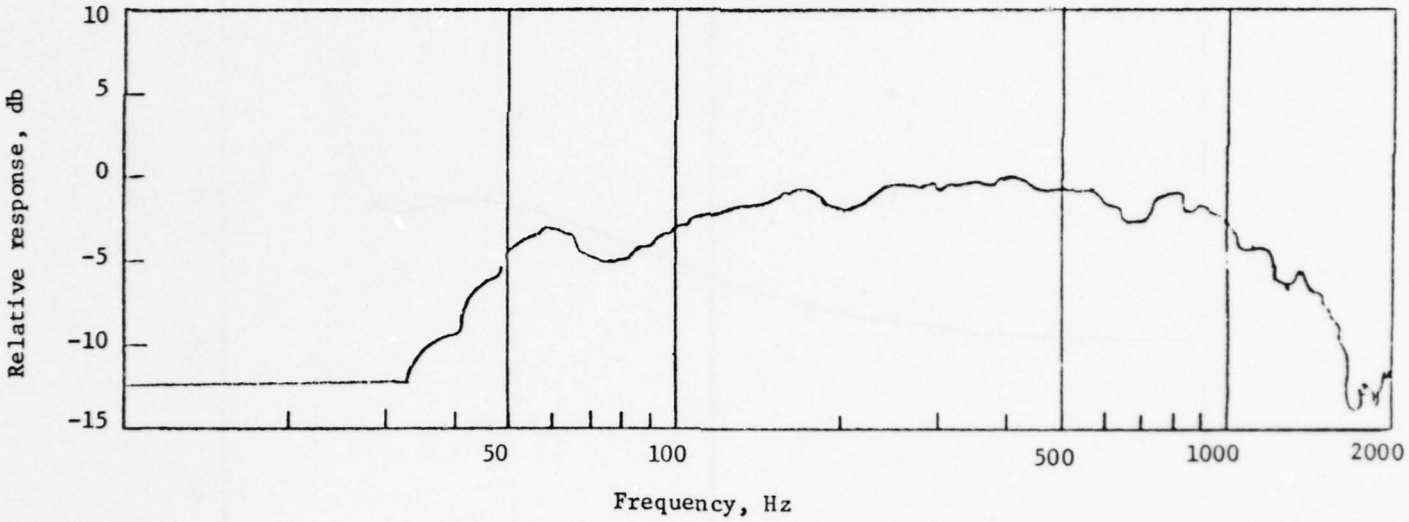

b. Frequency response of speaker referenced to peak speaker response

Figure 5. Frequency response of speaker as measured by a microphone under the speaker

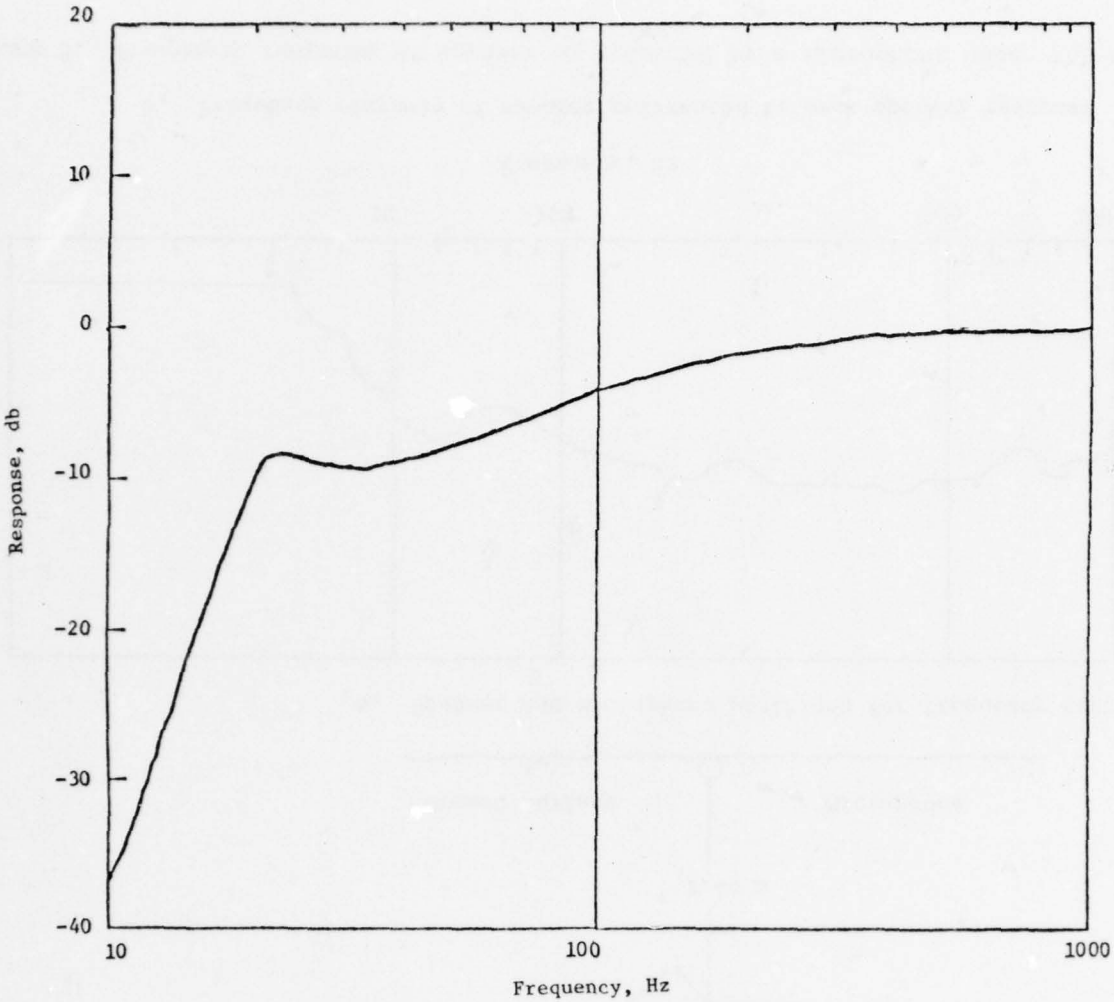

Figure 6. Theoretical frequency response curve of speaker provided by Altex Corporation

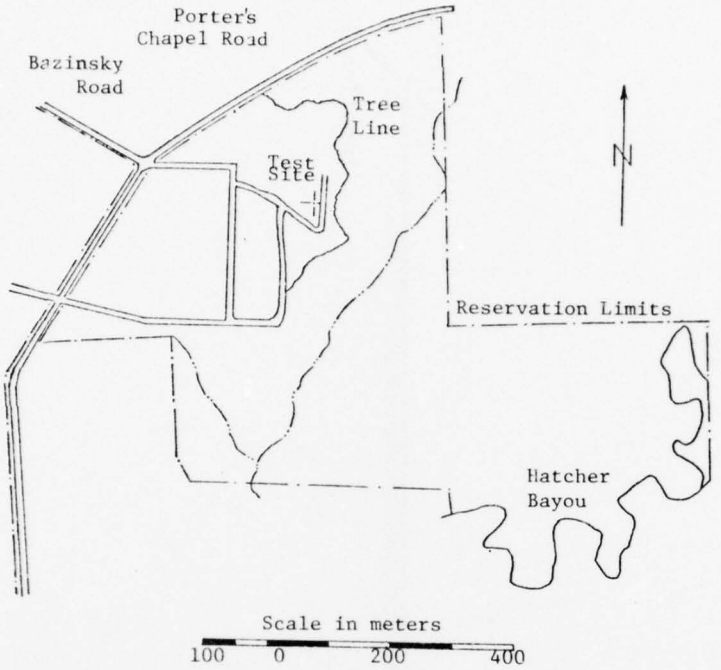

a. Location of test site

b. View of test site

Figure 7. Test site

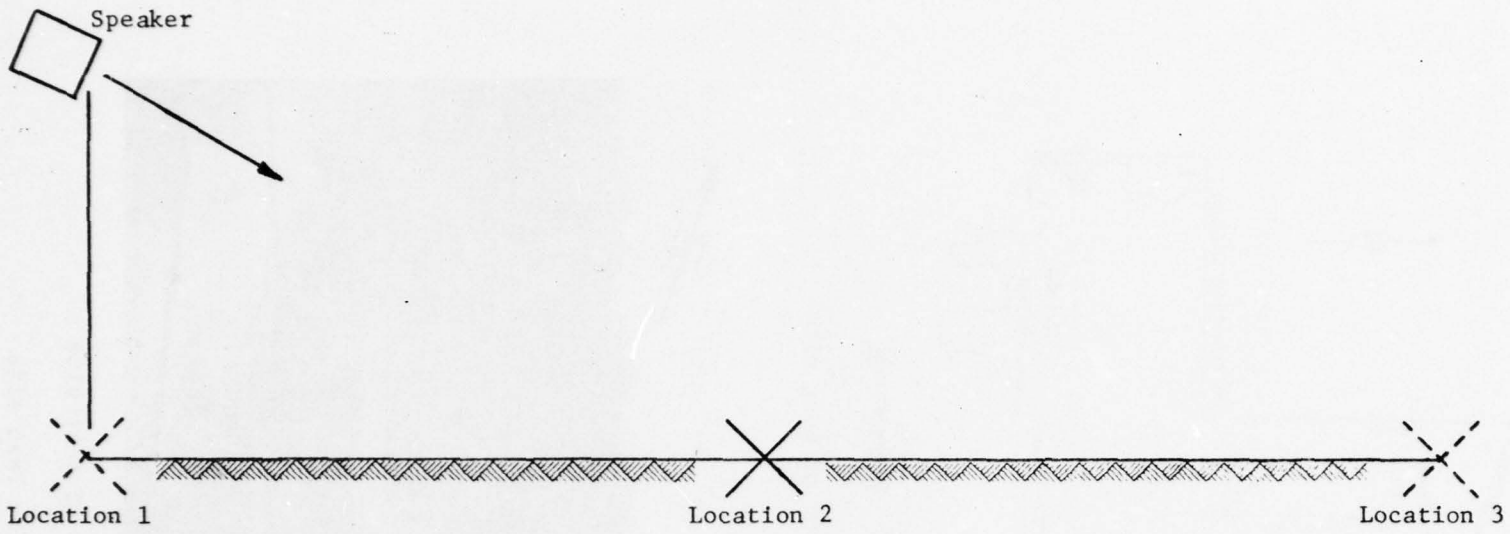

- Location of compression and shear wave velocity measurements

- Location of compression and shear and Rayleigh wave velocity measurements

Note: Seismic velocity measurements were taken at Locations 1, 2, and 3 for Test I but only at Location 2 for Test II.

Figure 8. Locations of seismic velocity measurements

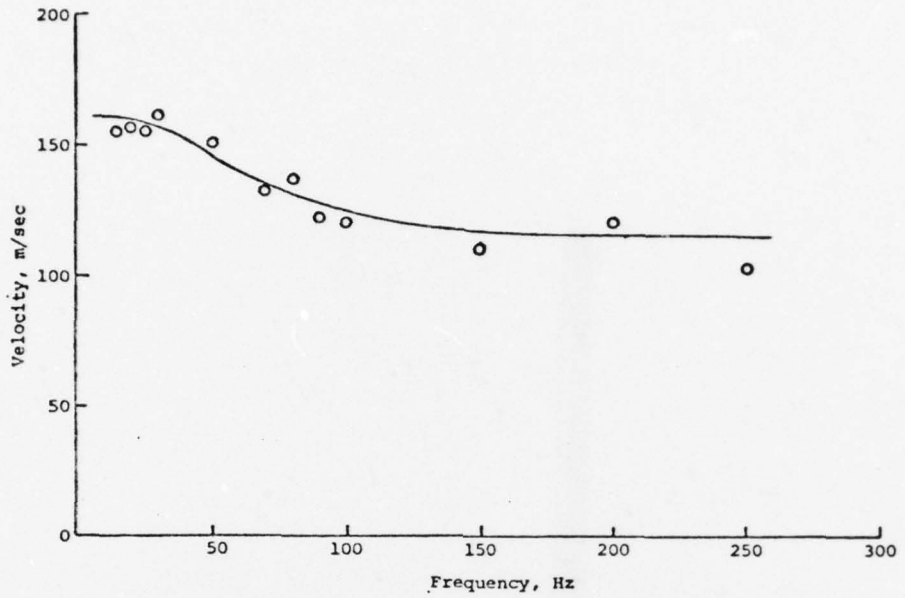

a. Test I

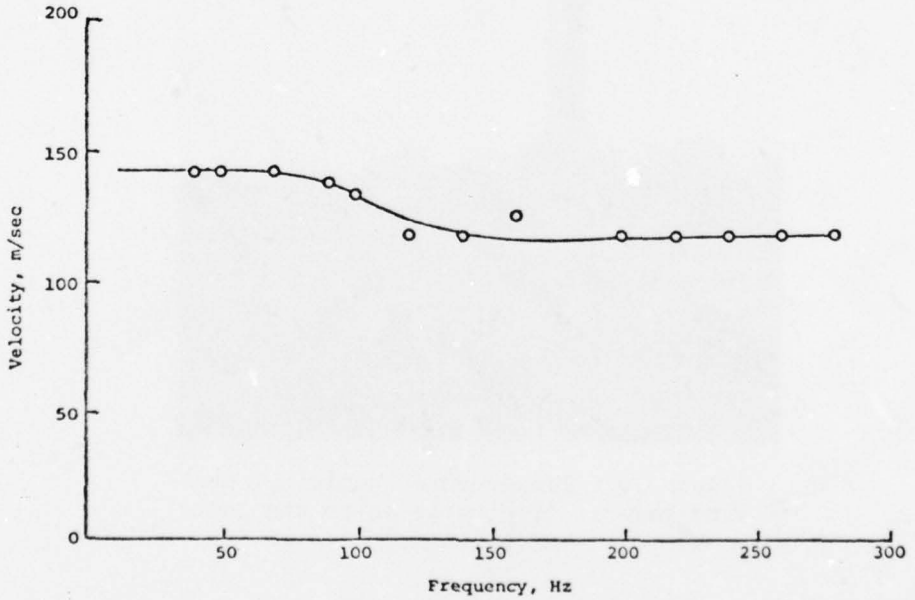

b. Test II

Figure 9. Measured Rayleigh wave velocities at location 2 (Figure 7) for Test I and Test II

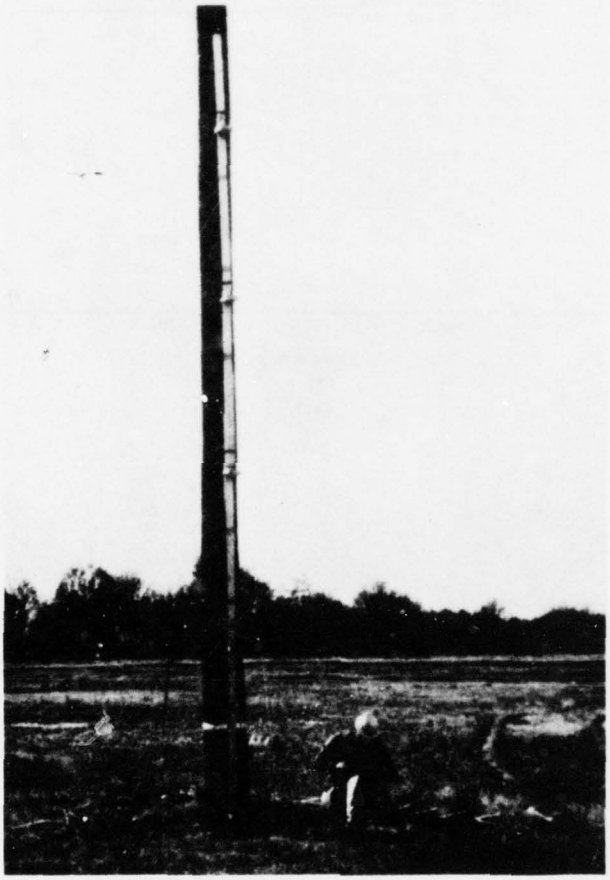

Figure 10. Temperature, humidity, and wind gages. (Test site is to the left of picture.)

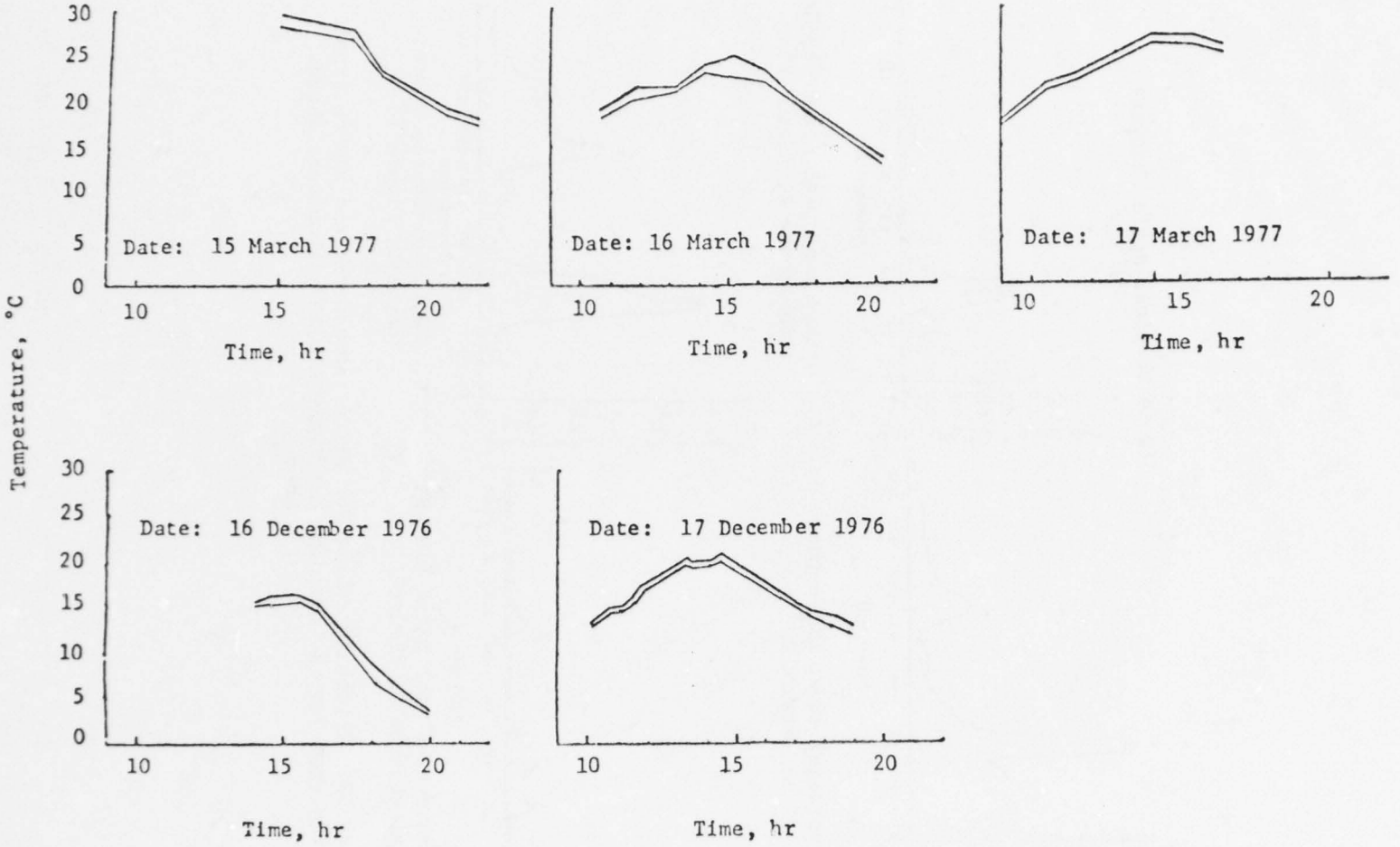

Figure 11. Minimum and maximum temperatures during testing periods (time based on 24-hour day)

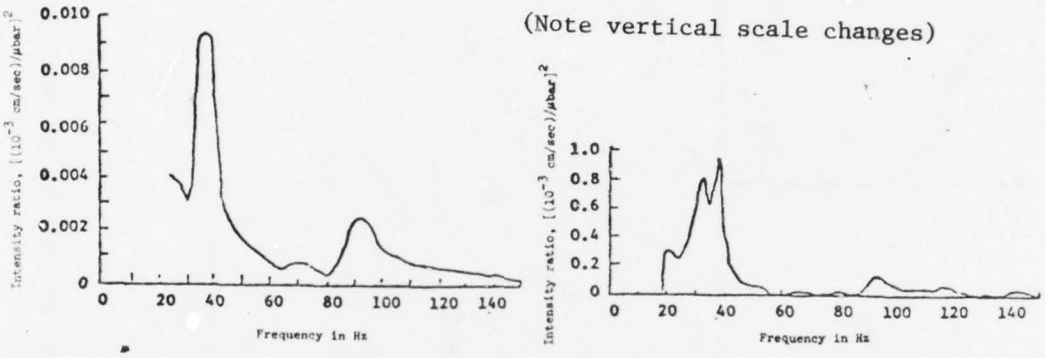

a. Frequency sweep (microphone B, Figure 1)

b. Octave band pink noise (63-Hz) (microphone A, Figure 1)

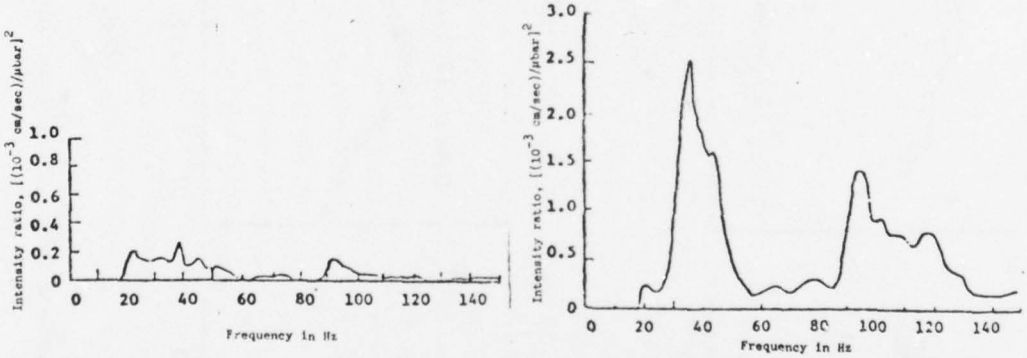

c. Octave band pink noise (125-Hz) (microphone A, Figure 1)

d. Impulsive source (microphone B, Figure 1)

Figure 12. Intensity ratios for different sources and source types derived from Test I (geophone d, Figure 1 with microphones shown above)

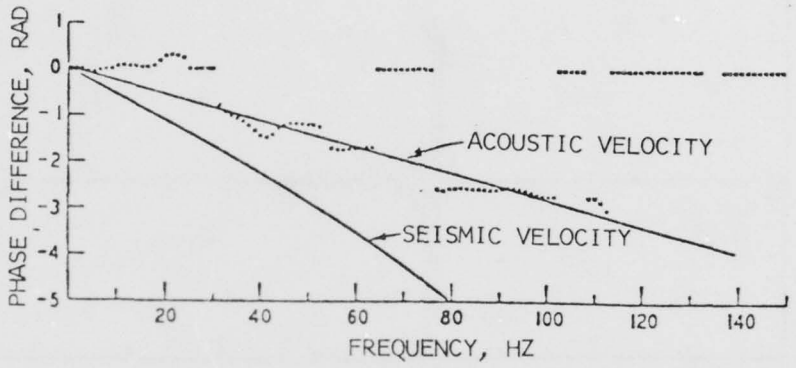

a. 63-Hz octave band noise

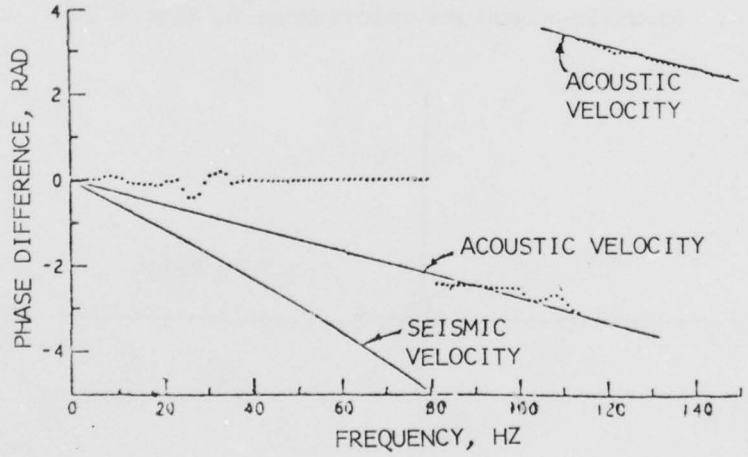

b. 125-Hz octave band noise

Figure 13. Phase difference for Test I, location 2, averaged over five pairs of geophones (ce, eg, gh, hi, and ij in Figure 1)

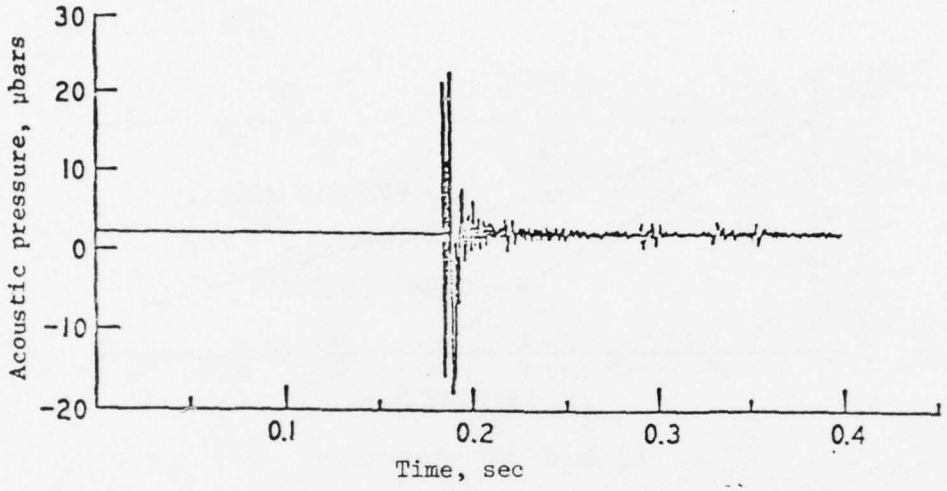

a. Acoustic signature (microphone B, Figure 1)

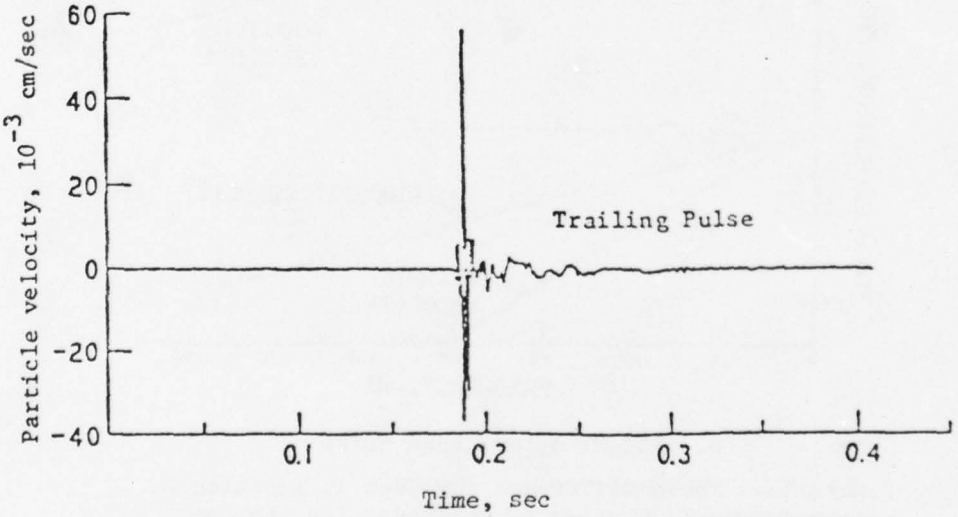

b. Seismic signature vertical (geophone d, Figure 1)

Figure 14. Acoustic and seismic time domain signatures for acoustic impulse

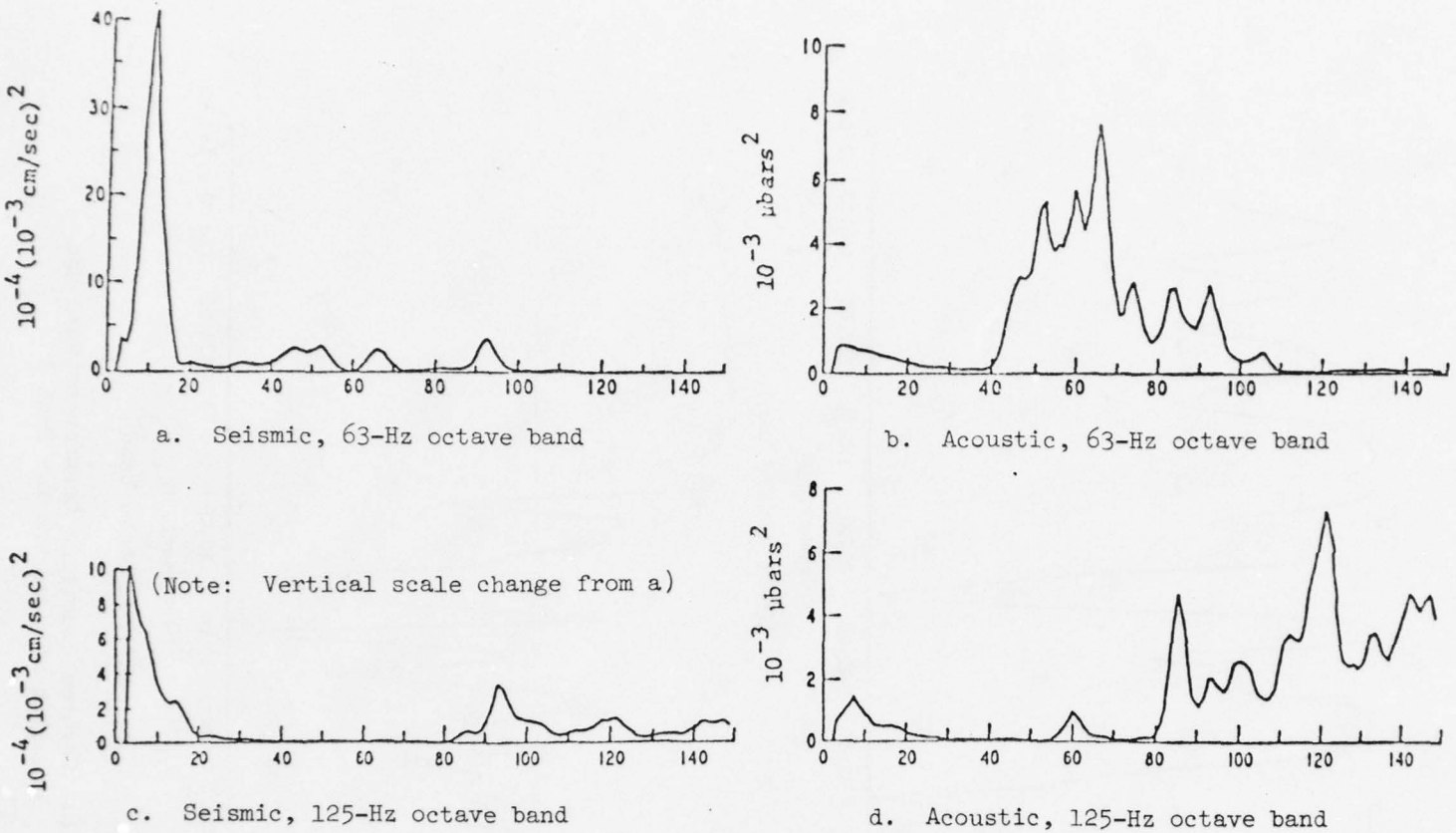

a. Seismic, 63-Hz octave band

b. Acoustic, 63-Hz octave band

c. Seismic, 125-Hz octave band

d. Acoustic, 125-Hz octave band

Figure 15. Seismic and acoustic autospectra used in calculating the squared coherence in Figure 16 (using geophone d and microphone A, Figure 1)

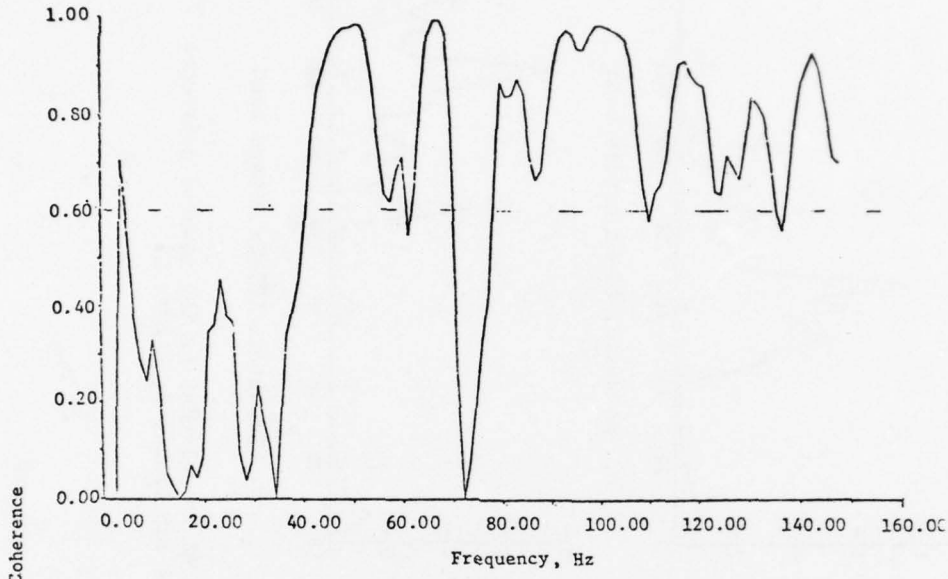

a. 63-Hz octave band

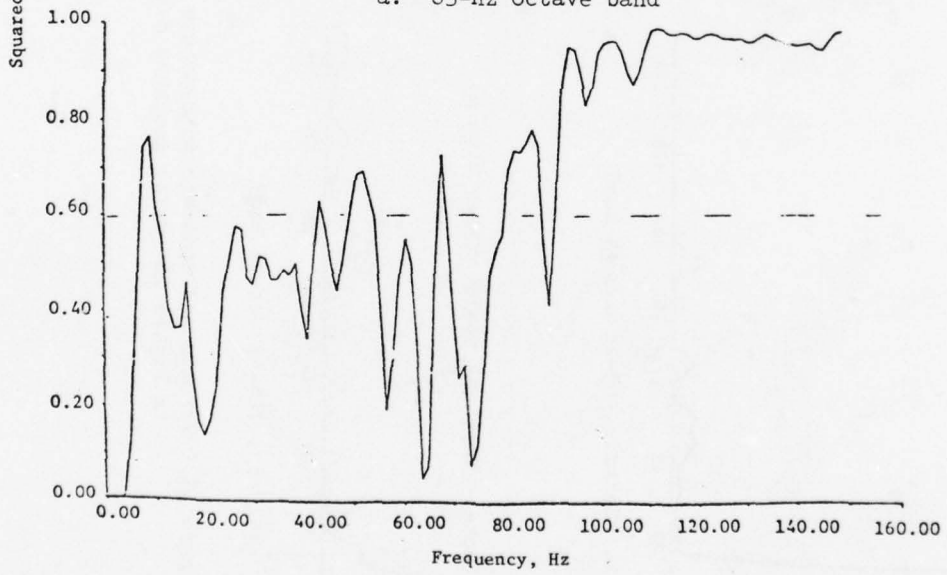

b. 125-Hz octave band

Figure 16. Squared coherence between seismic and acoustic autospectra for Test I

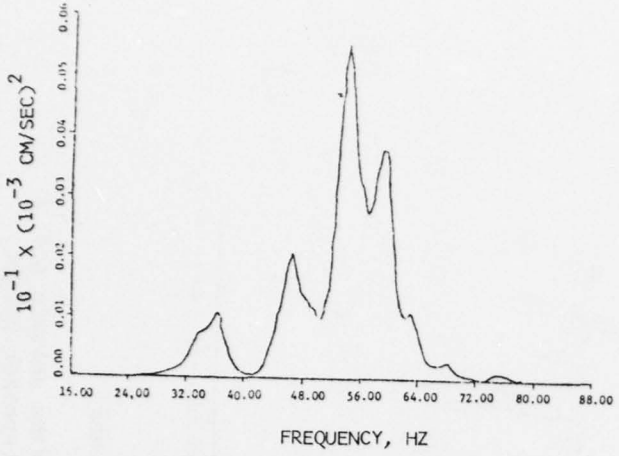

a. Seismic, 40-Hz 1/3-octave band

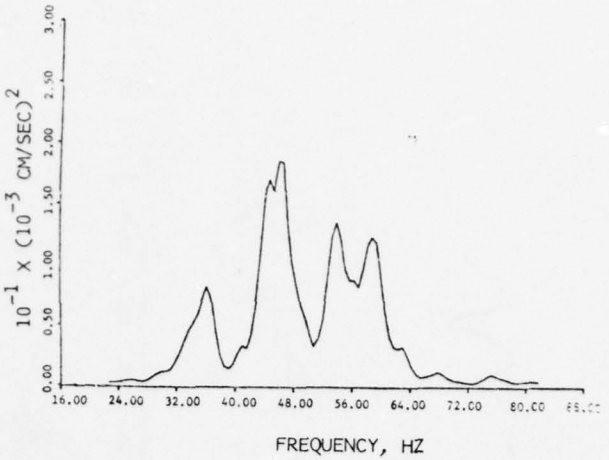

b. Acoustic, 40-Hz 1/3-octave band

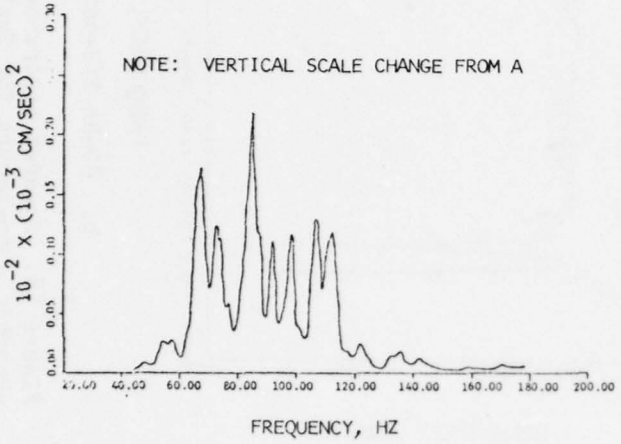

c. Seismic, 90-Hz 1/3-octave band

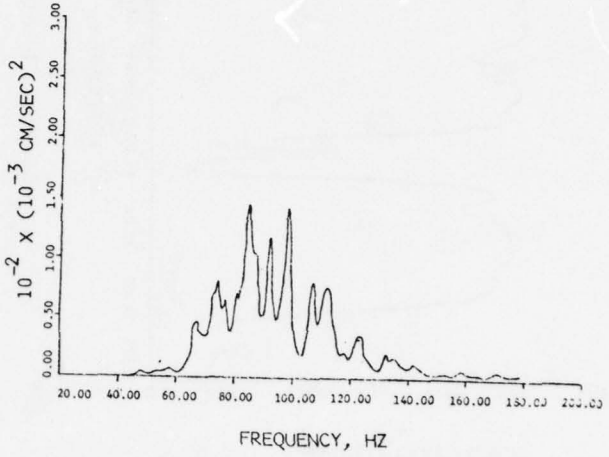

d. Acoustic, 90-Hz 1/3-octave band

Figure 17. Seismic and acoustic autospectra used in calculating the squared coherence in Figure 18 (using geophone d and microphone A, Figure 2)

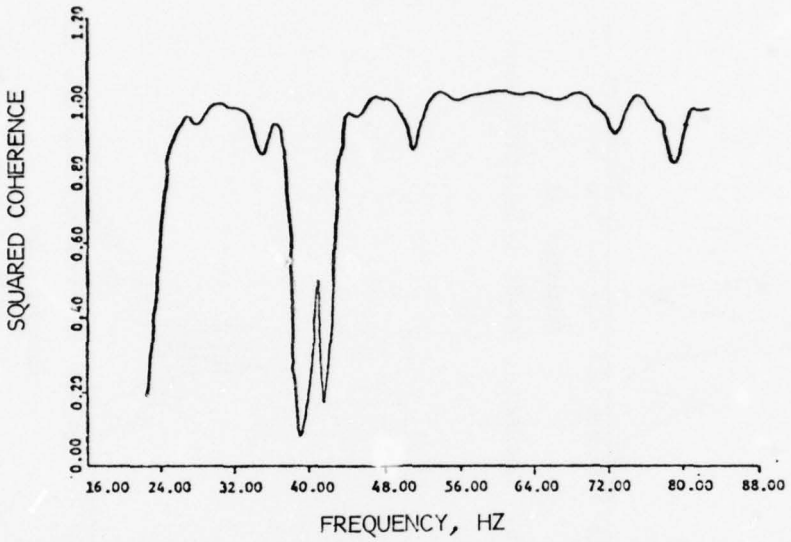

a. 40-Hz 1/3-octave band

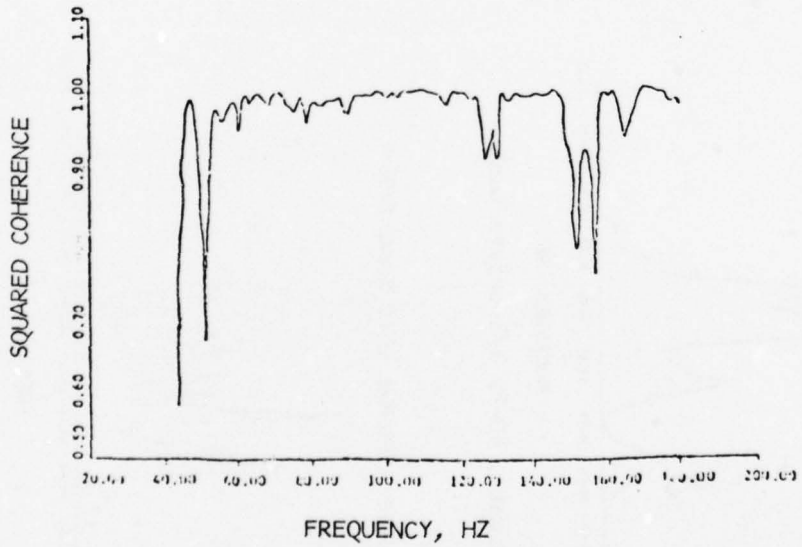

b. 90-Hz 1/3-octave band

Figure 18. Squared coherence between seismic and acoustic autospectra for Test II (speaker height, 2.44 m, with sensors at 10-m location)

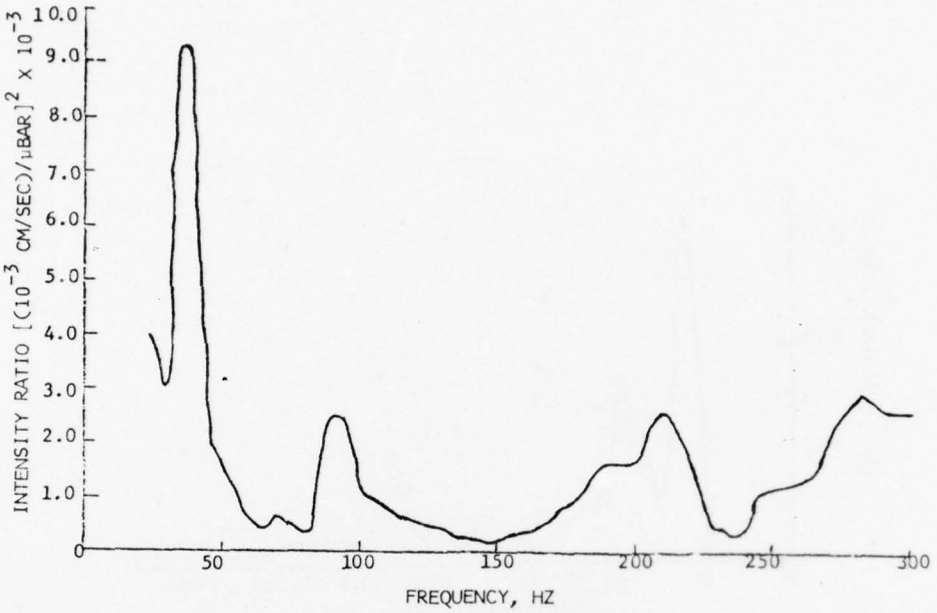

a. Test I (geophone d and microphone B)

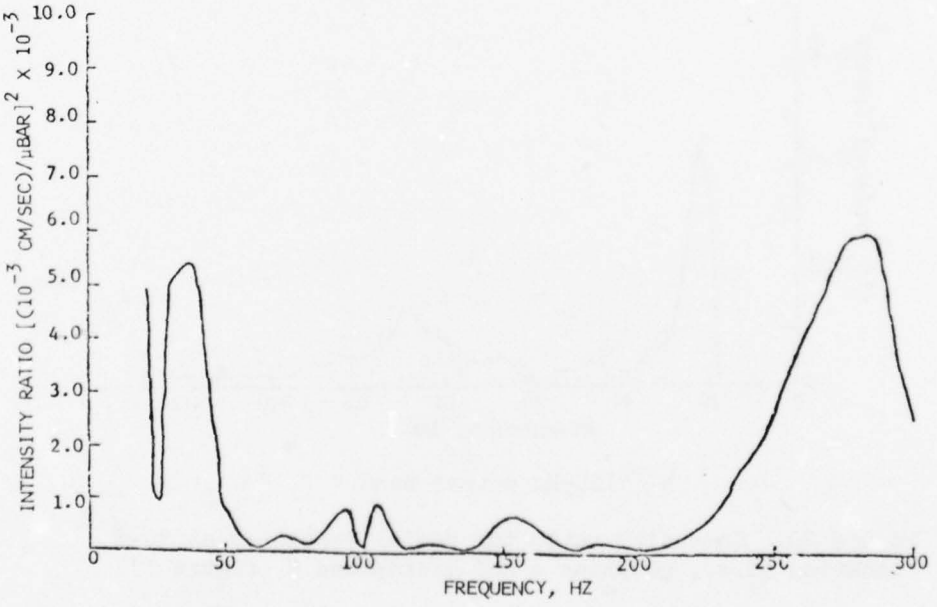

b. Test II (geophone g and microphone B)

Figure 19. Intensity ratio results for frequency sweeps in Tests I and II

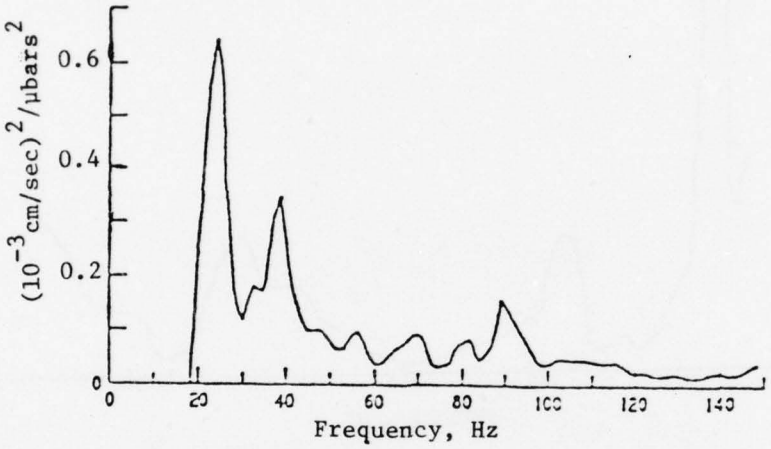

a. 63-Hz octave band

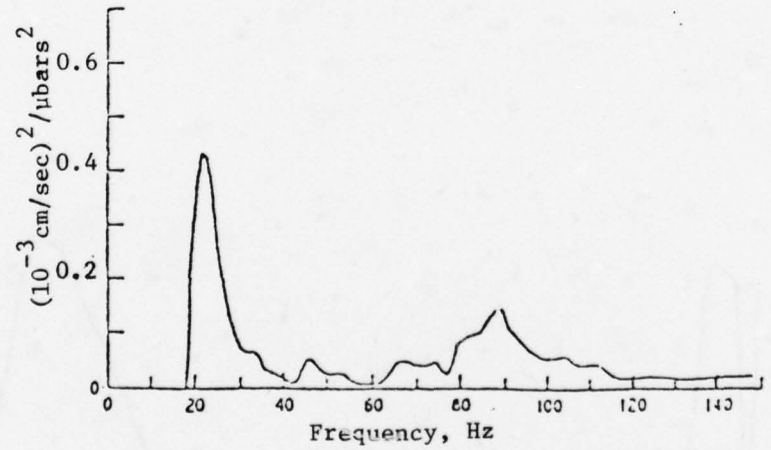

b. 125-Hz octave band

Figure 20. Intensity ratio for radial geophones at 30-m location (i.e., geophone d and microphone B, Figure 1)

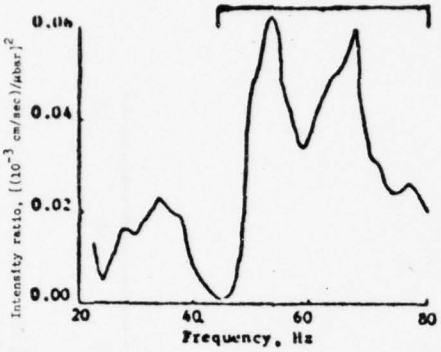

a. Speaker height: 1 m

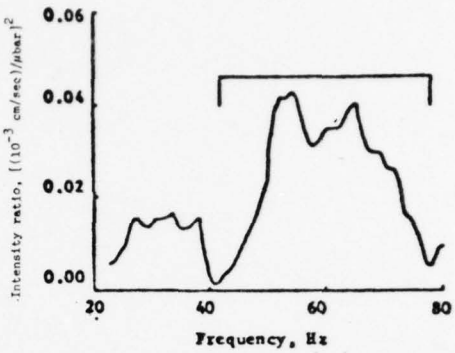

b. Speaker height: 2.44 m

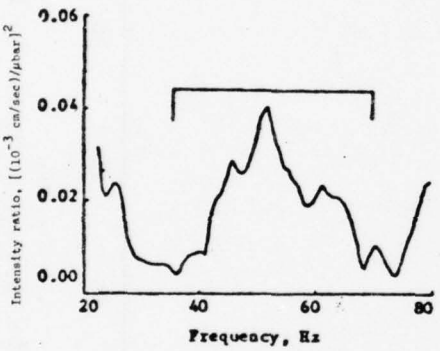

c. Speaker height: 5 m

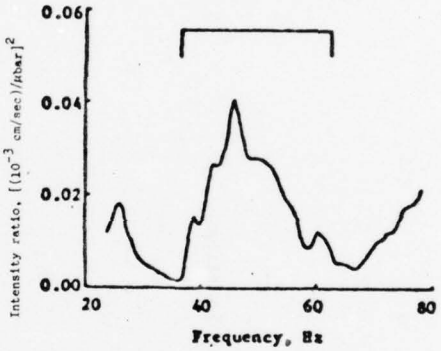

d. Speaker height: 7.5 m

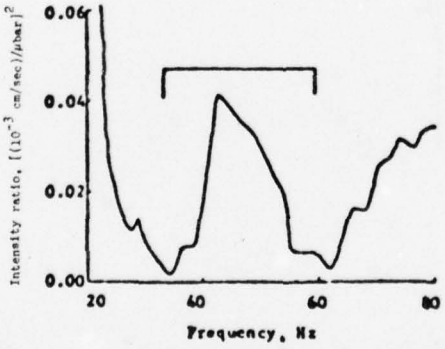

e. Speaker height: 10 m

Figure 21. Shift in dominant peaks of intensity ratio spectra as a function of speaker height (using microphone A and geophone d, Figure 2)

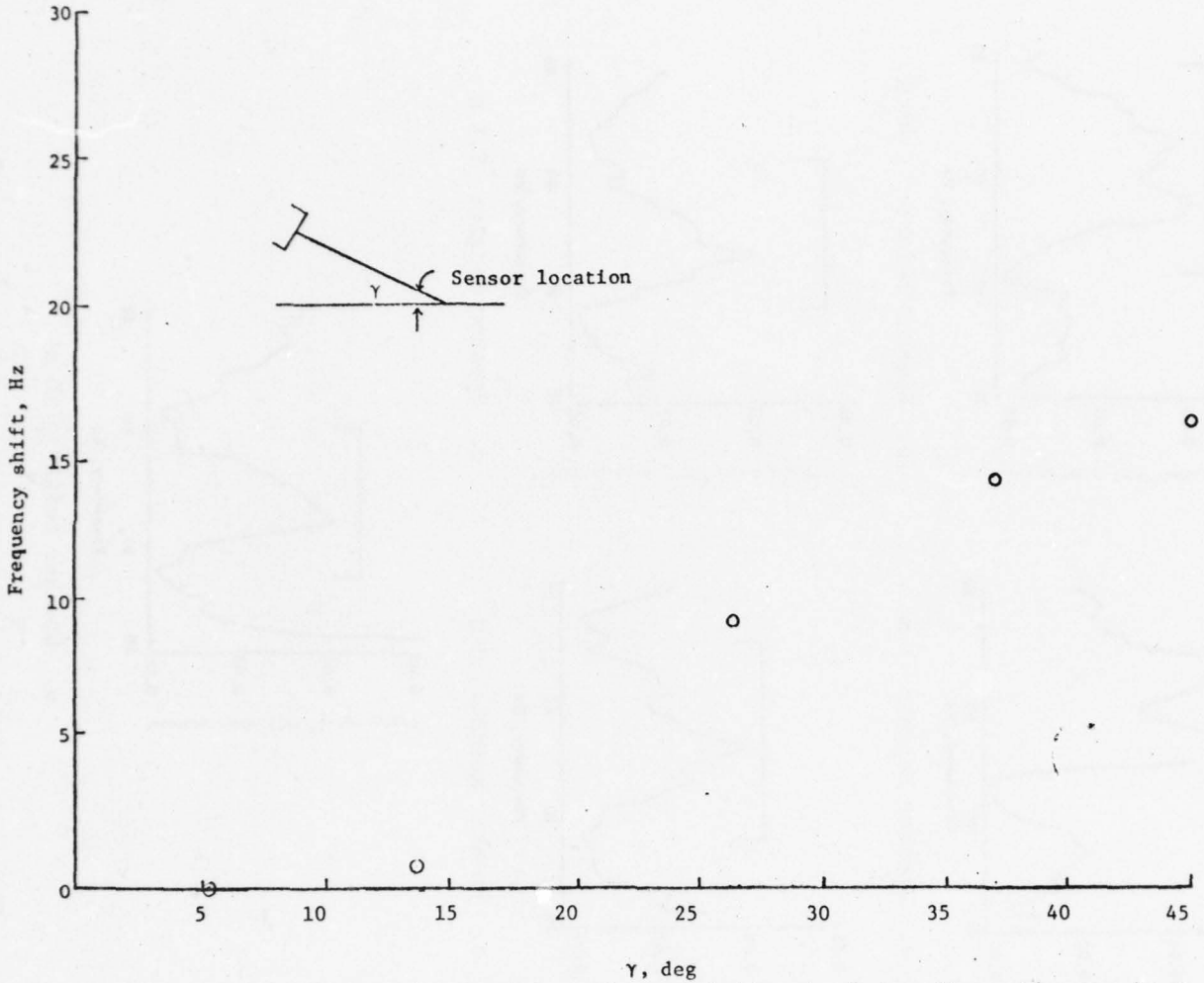

Figure 22. Shift of intensity ratio spectrum relative to intensity ratio spectrum for lowest source height (1 m, γ = 5.7 deg) and the 40-Hz 1/3-octave band

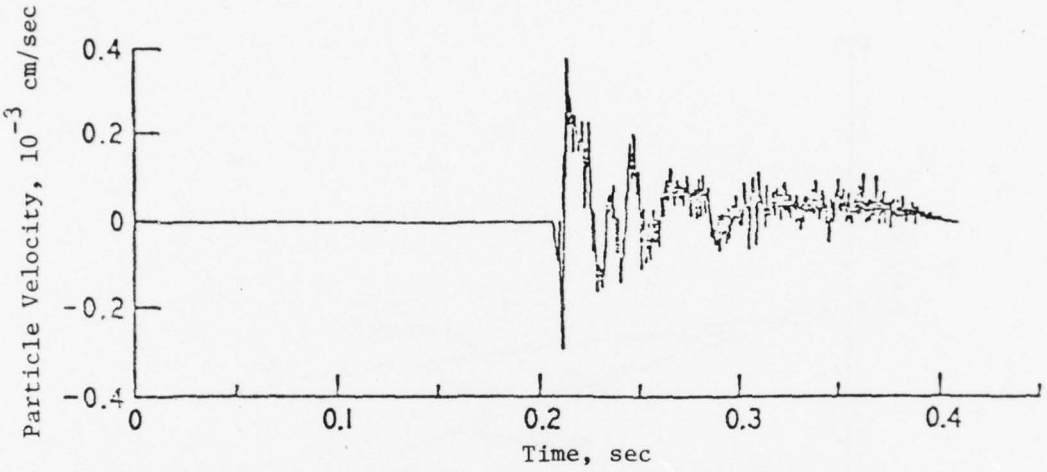

a. Signature at 28.5 m from source location (geophone b)

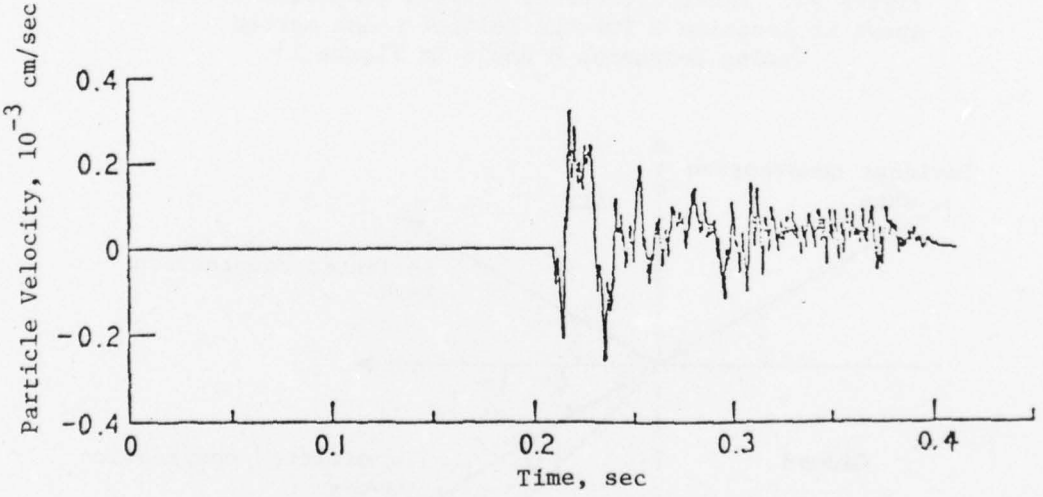

b. Signature at 29.25 m from source location (geophone c)

Figure 23. Geophone signatures after zeroing initial pulse

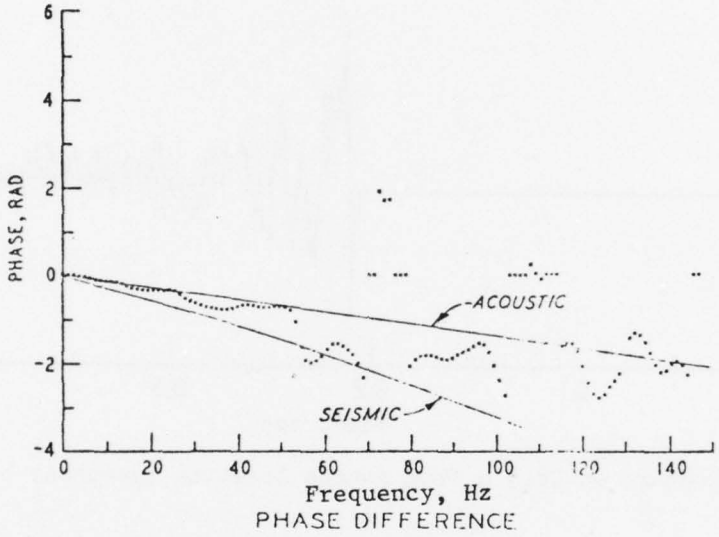

Figure 24. Phase difference between geophones 0.75 m apart at location 2 for the initial pulse zeroed (using geophones b and c in Figure 1)

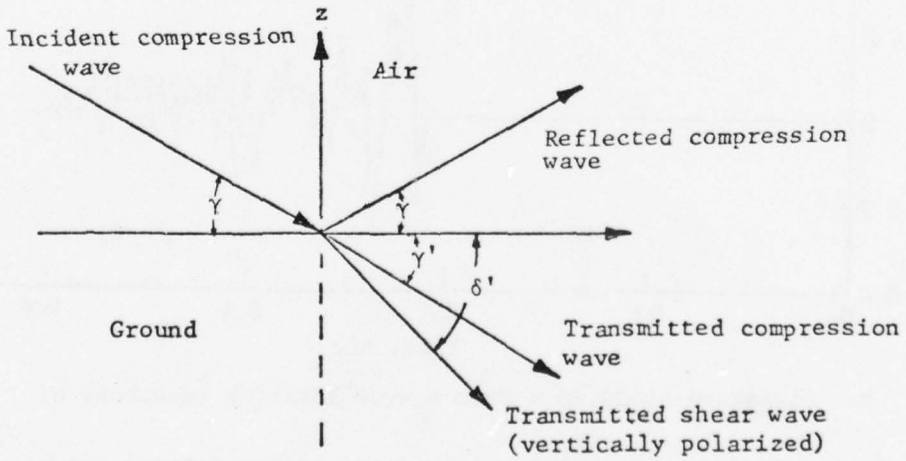

Figure 25. Reflection and transmission of incident sound wave

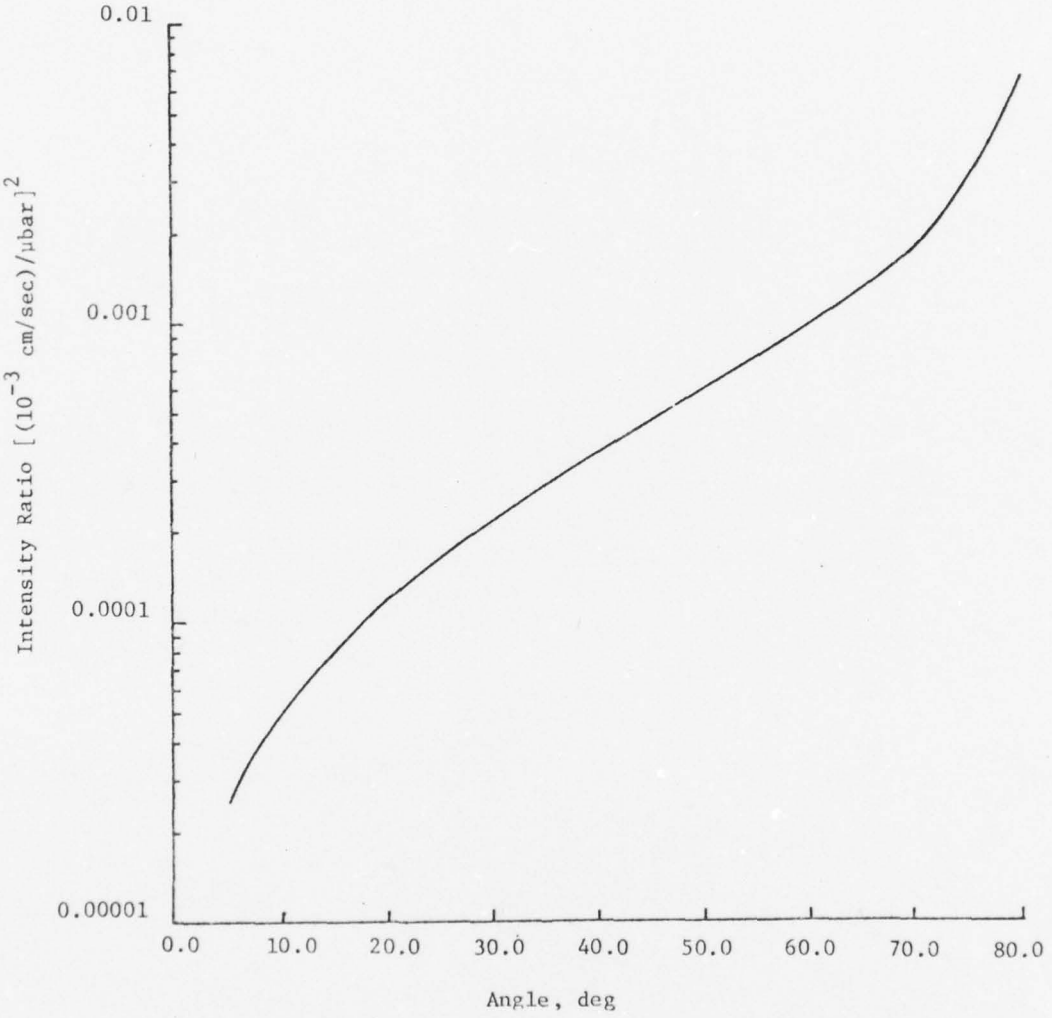

Figure 26. Theoretical intensity ratio for incident plane wave as a function of incident angle

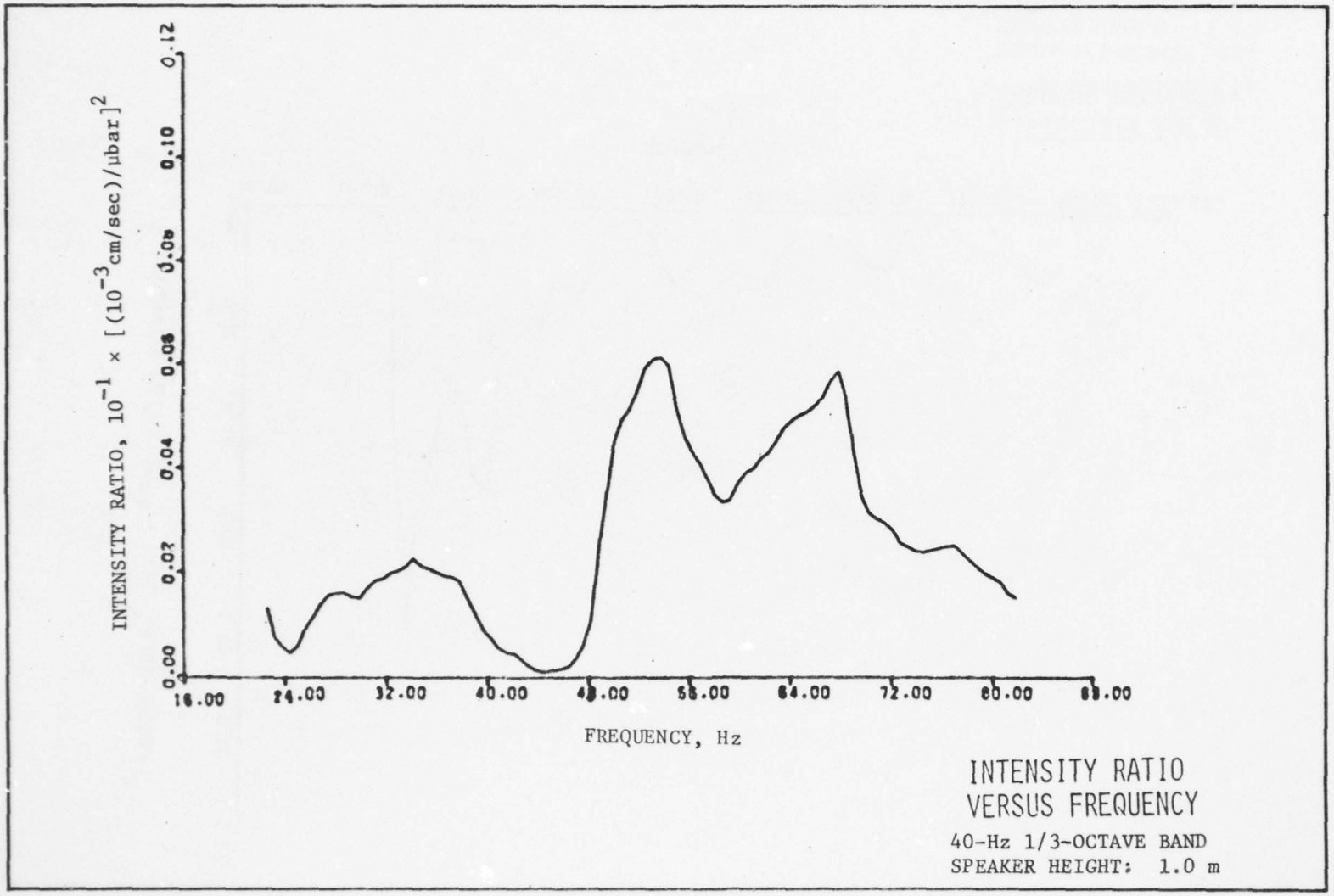

INTENSITY RATIO
VERSUS FREQUENCY

40-Hz 1/3-OCTAVE BAND
SPEAKER HEIGHT: 1.0 m

PLATE 1

PLATE 2

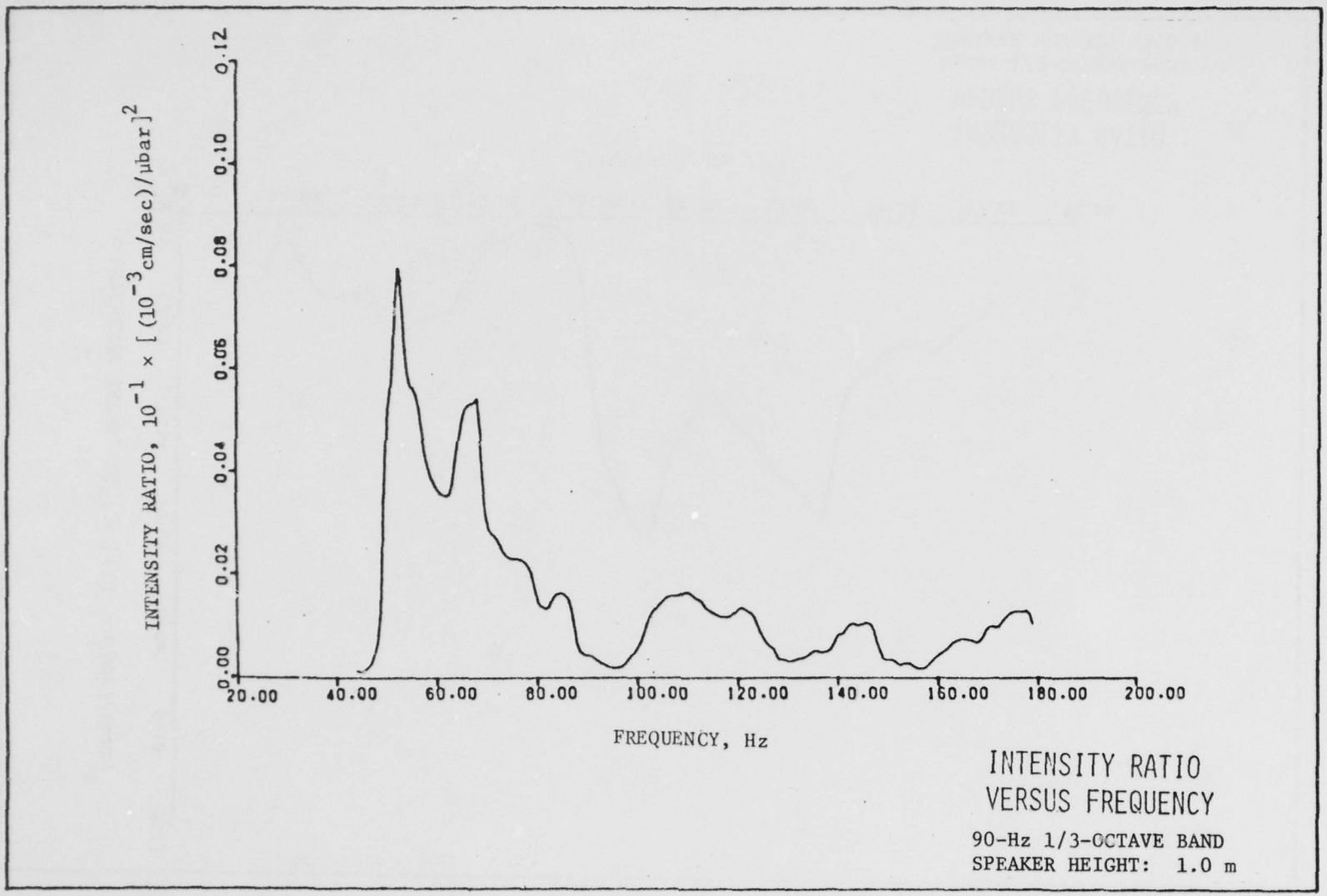

INTENSITY RATIO
VERSUS FREQUENCY

90-Hz 1/3-OCTAVE BAND
SPEAKER HEIGHT: 1.0 m

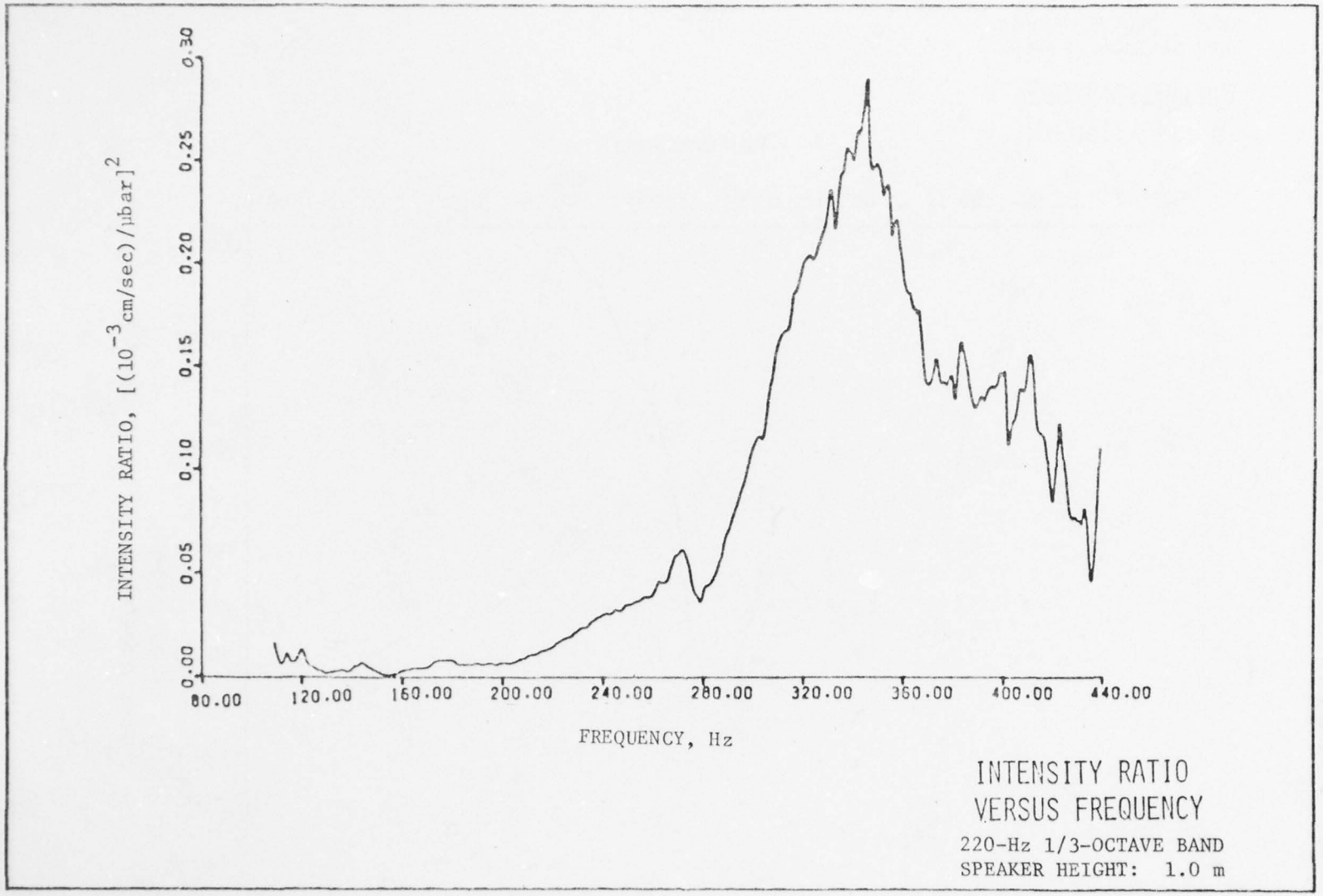

INTENSITY RATIO
VERSUS FREQUENCY

220-Hz 1/3-OCTAVE BAND
SPEAKER HEIGHT: 1.0 m

PLATE 3

PLATE 4

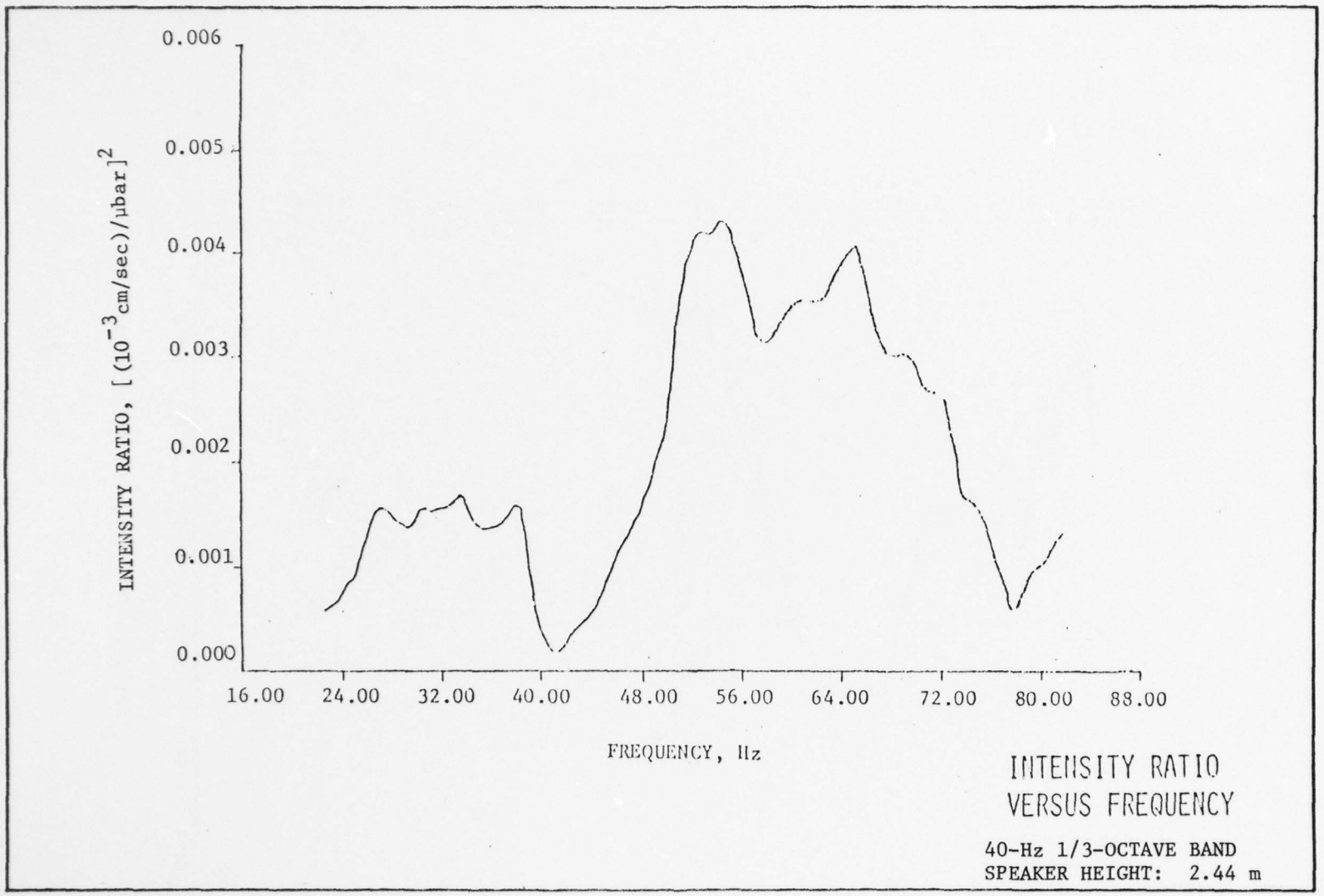
0.006
0.005
0.004
0.003
0.002
0.001
0.000
INTENSITY RATIO, [(10^-3 cm/sec)/μbar]^2
16.00
24.00
32.00
40.00
48.00
56.00
64.00
72.00
80.00
88.00
FREQUENCY, Hz
INTENSITY RATIO
VERSUS FREQUENCY
40-Hz 1/3-OCTAVE BAND
SPEAKER HEIGHT: 2.44 m

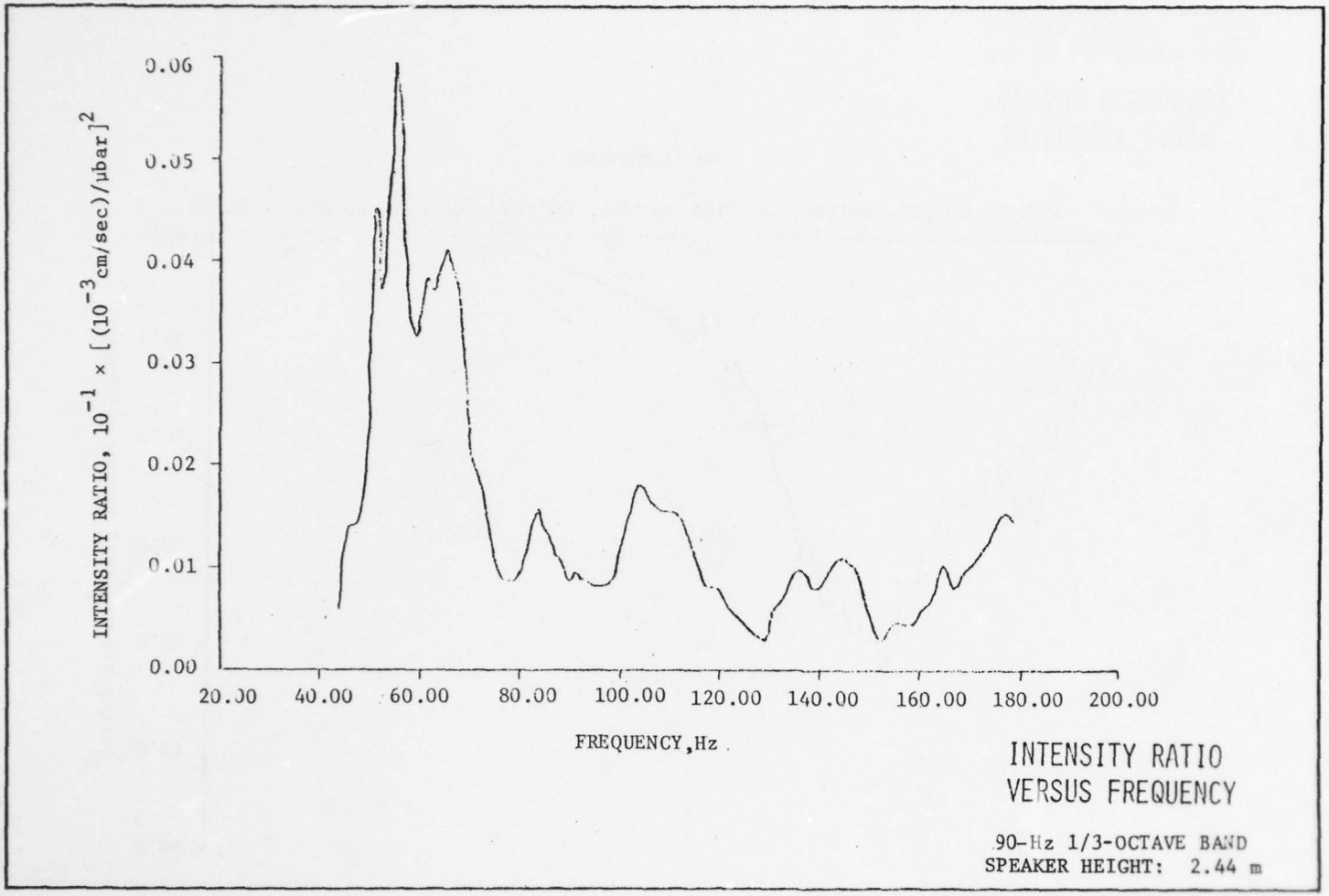

INTENSITY RATIO
VERSUS FREQUENCY

90-Hz 1/3-OCTAVE BAND
SPEAKER HEIGHT: 2.44 m

PLATE 5

PLATE 6

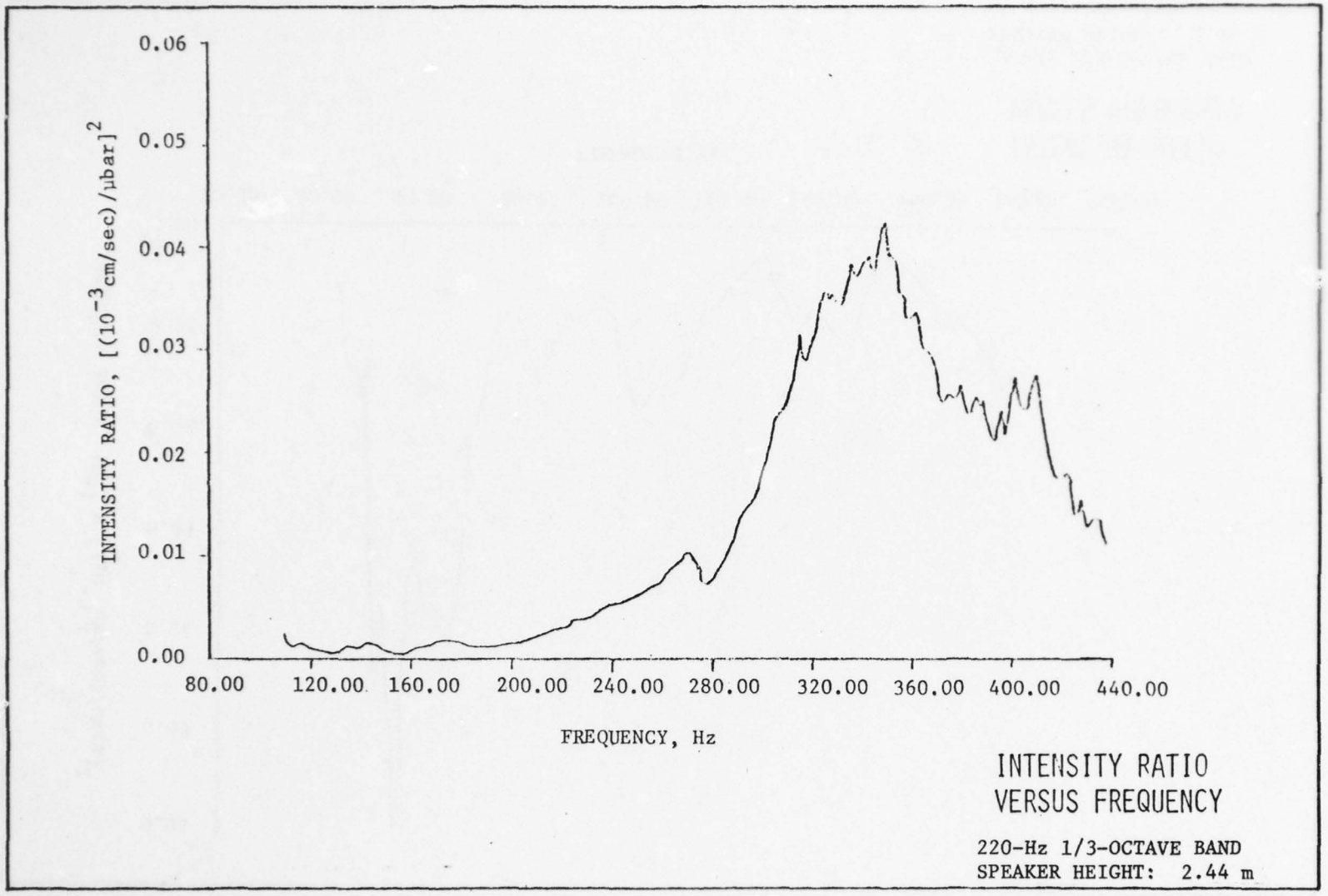

INTENSITY RATIO
VERSUS FREQUENCY

220-Hz 1/3-OCTAVE BAND
SPEAKER HEIGHT: 2.44 m

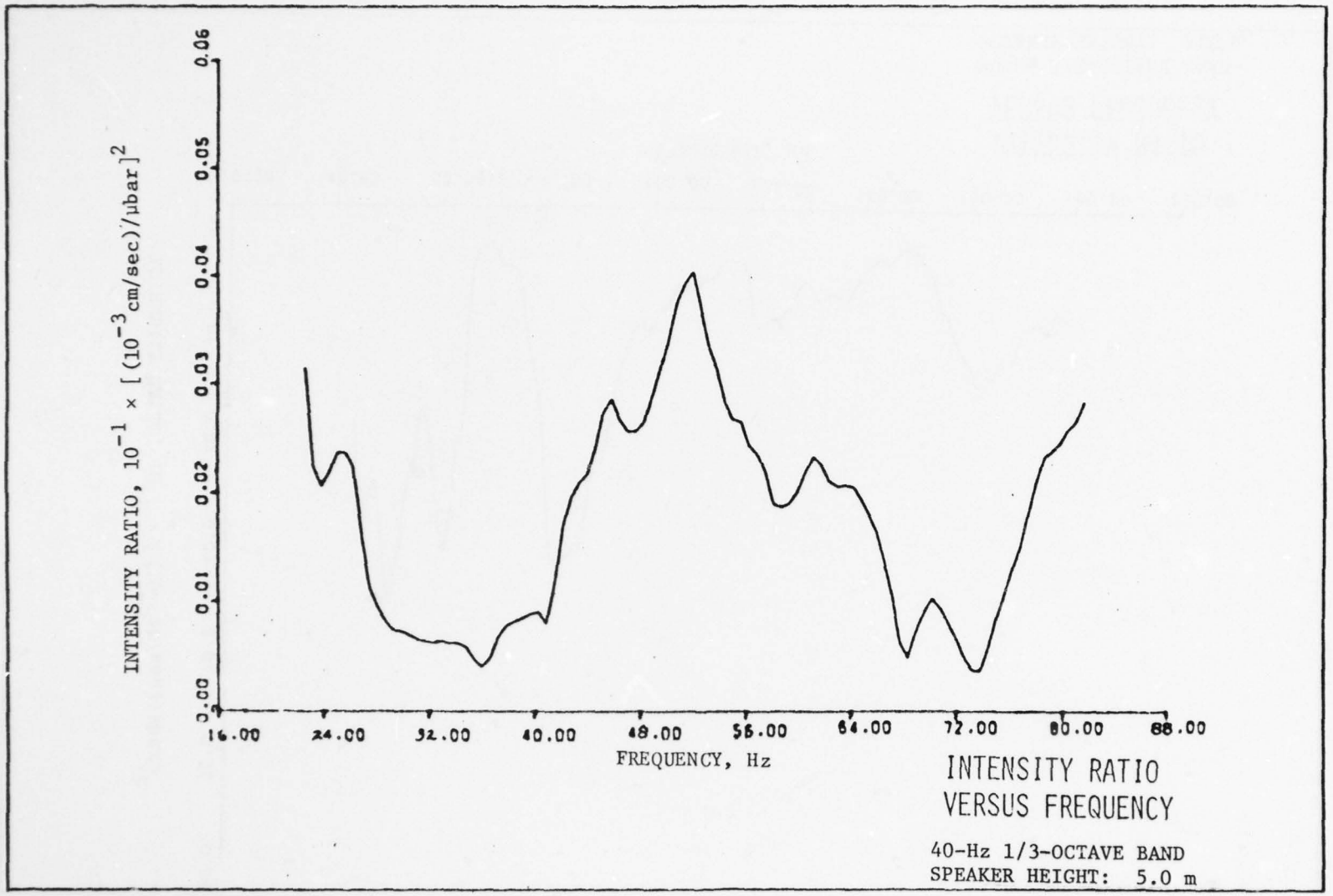
INTENSITY RATIO, $10^{-1} \times [(10^{-3}$ cm/sec)/μbar$]^2$
0.00
0.01
0.02
0.03
0.04
0.05
0.06
16.00
24.00
32.00
40.00
48.00
56.00
64.00
72.00
80.00
88.00
FREQUENCY, Hz
INTENSITY RATIO
VERSUS FREQUENCY
40-Hz 1/3-OCTAVE BAND
SPEAKER HEIGHT: 5.0 m

PLATE 7

PLATE 8

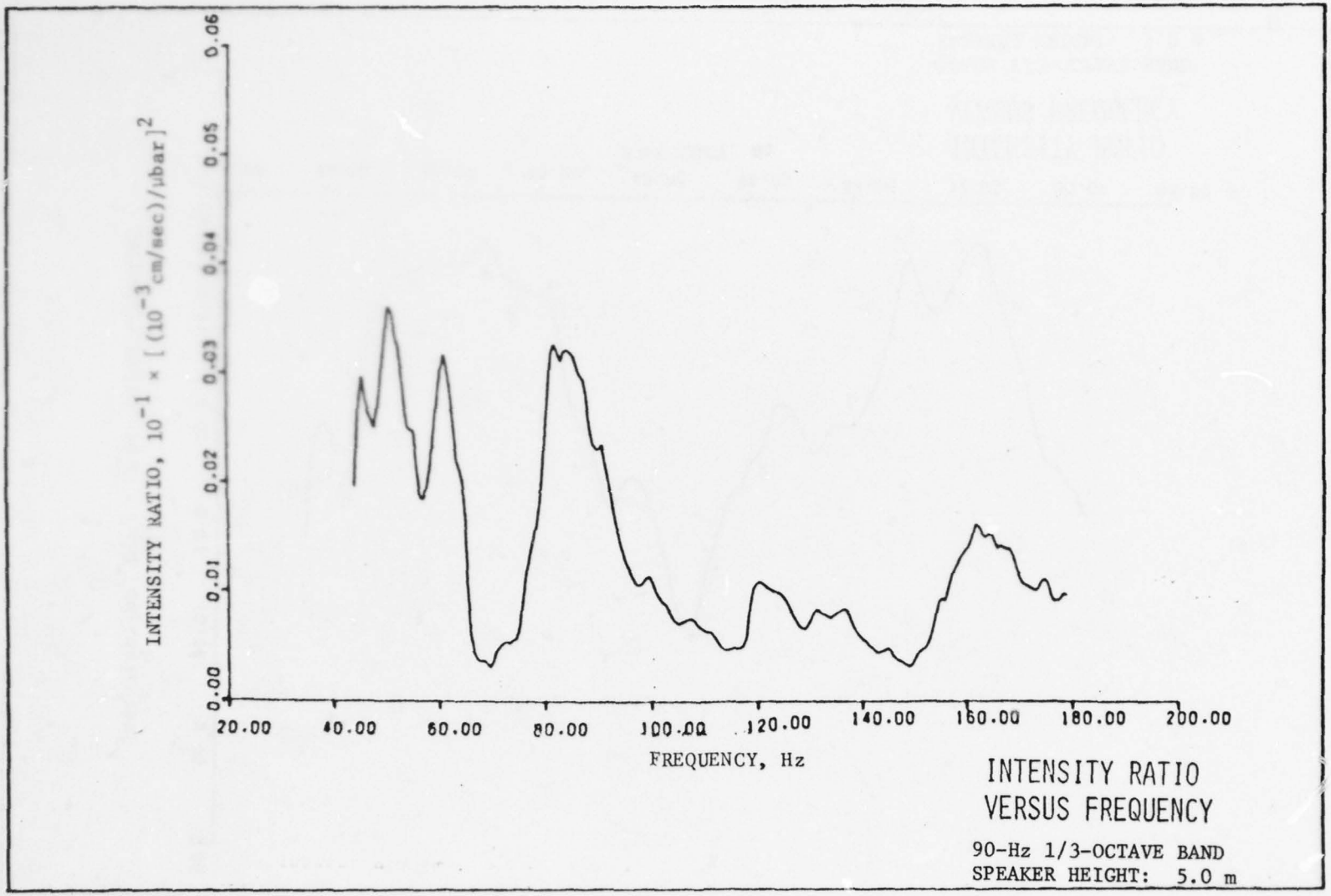

INTENSITY RATIO
VERSUS FREQUENCY

90-Hz 1/3-OCTAVE BAND
SPEAKER HEIGHT: 5.0 m

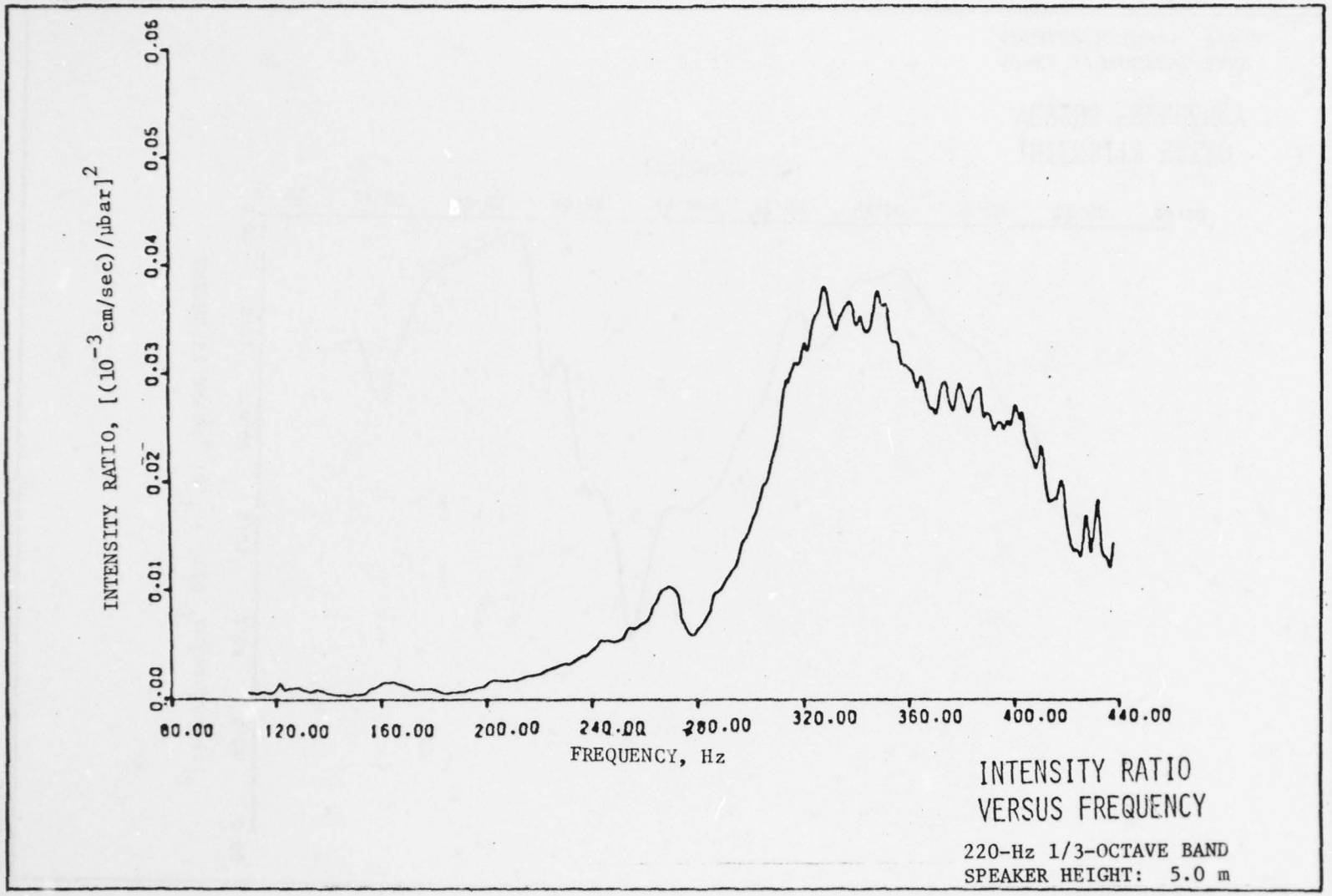
INTENSITY RATIO, [(10^{-3}cm/sec)/μbar]^2
0.00
0.01
0.02
0.03
0.04
0.05
0.06
80.00
120.00
160.00
200.00
240.00
280.00
320.00
360.00
400.00
440.00
FREQUENCY, Hz
INTENSITY RATIO
VERSUS FREQUENCY
220-Hz 1/3-OCTAVE BAND
SPEAKER HEIGHT: 5.0 m

PLATE 9

PLATE 10

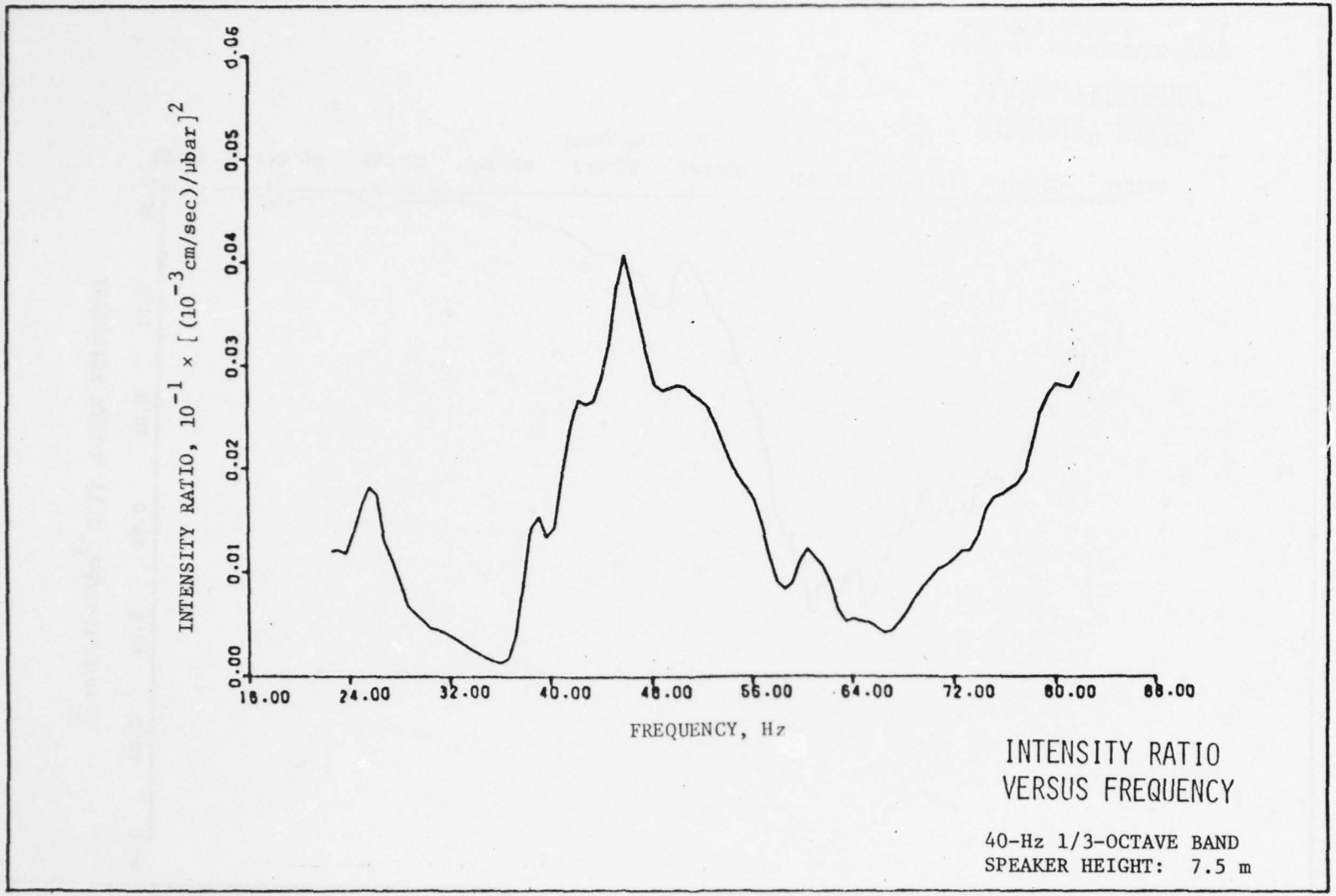

INTENSITY RATIO
VERSUS FREQUENCY

40-Hz 1/3-OCTAVE BAND
SPEAKER HEIGHT: 7.5 m

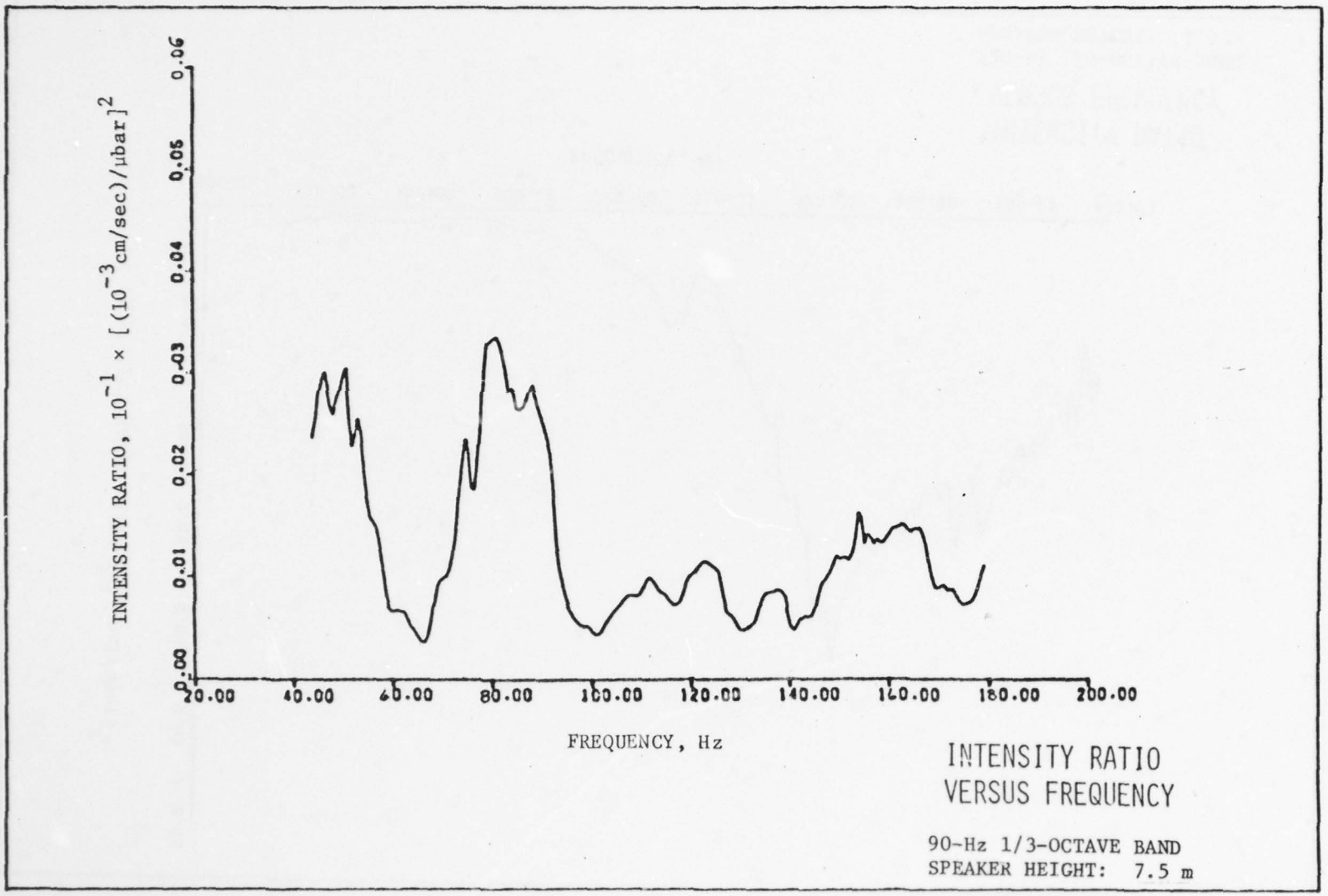

INTENSITY RATIO
VERSUS FREQUENCY

90-Hz 1/3-OCTAVE BAND
SPEAKER HEIGHT: 7.5 m

PLATE 11

PLATE 12

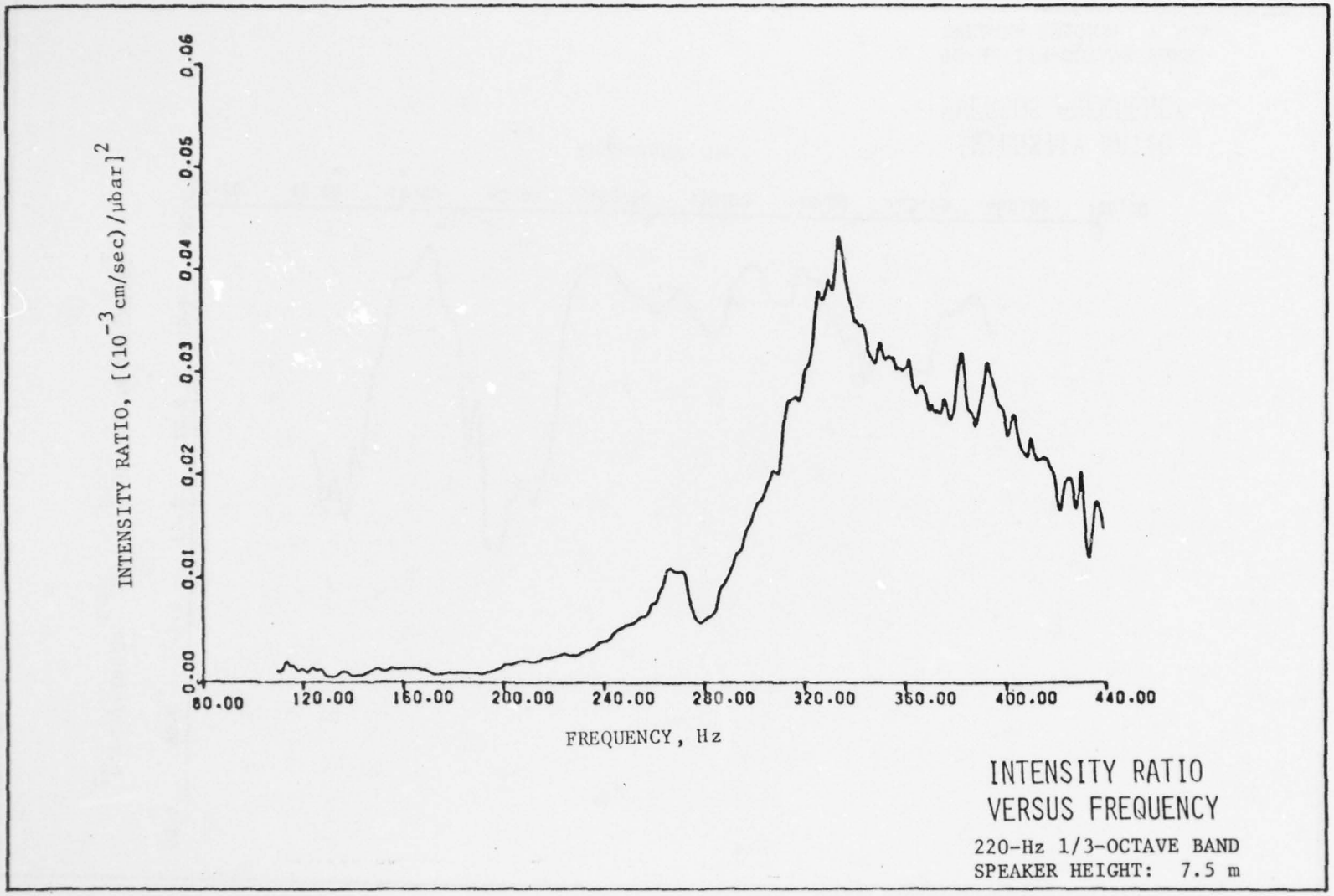

INTENSITY RATIO
VERSUS FREQUENCY

220-Hz 1/3-OCTAVE BAND
SPEAKER HEIGHT: 7.5 m

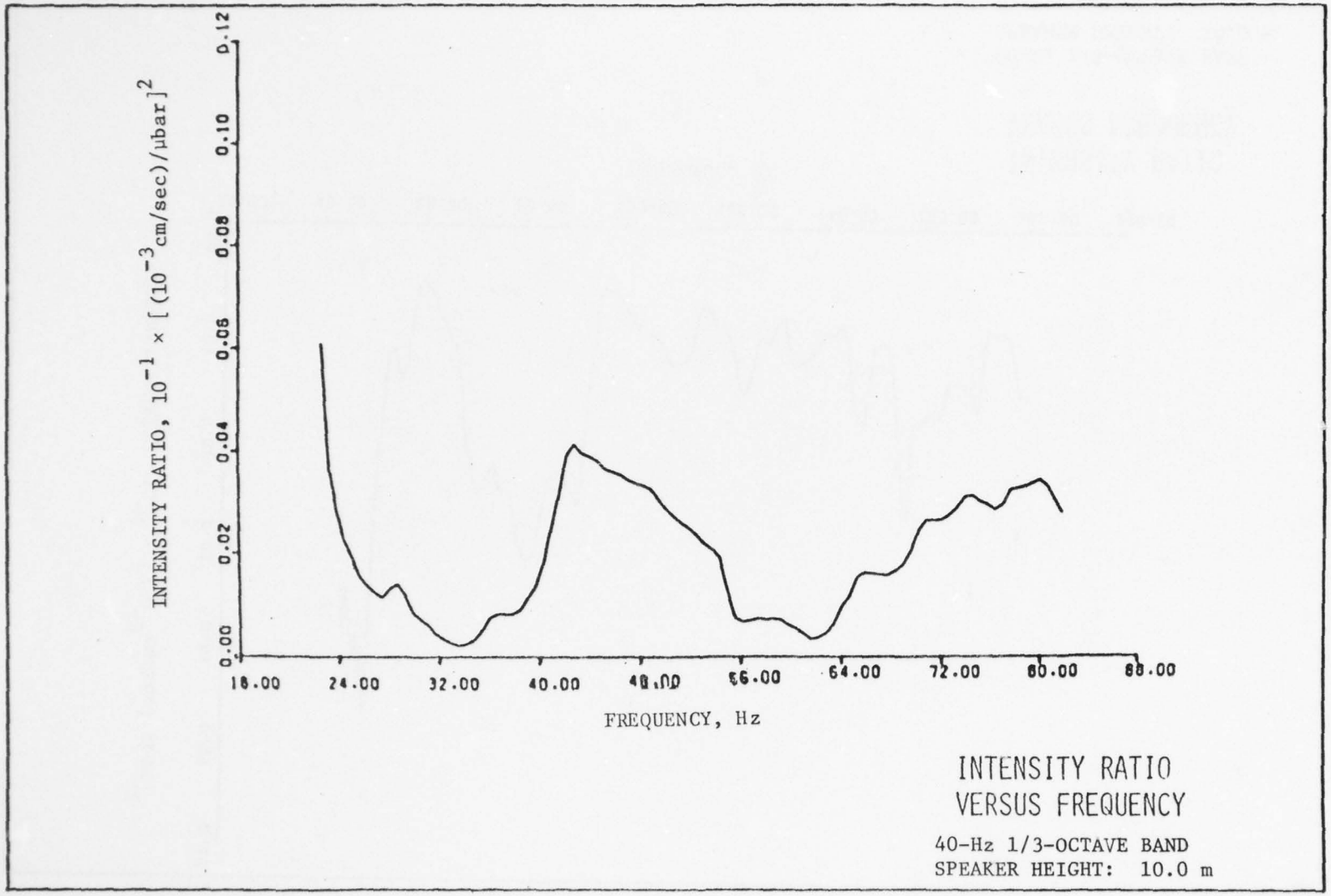

INTENSITY RATIO
VERSUS FREQUENCY

40-Hz 1/3-OCTAVE BAND
SPEAKER HEIGHT: 10.0 m

PLATE 13

PLATE 14

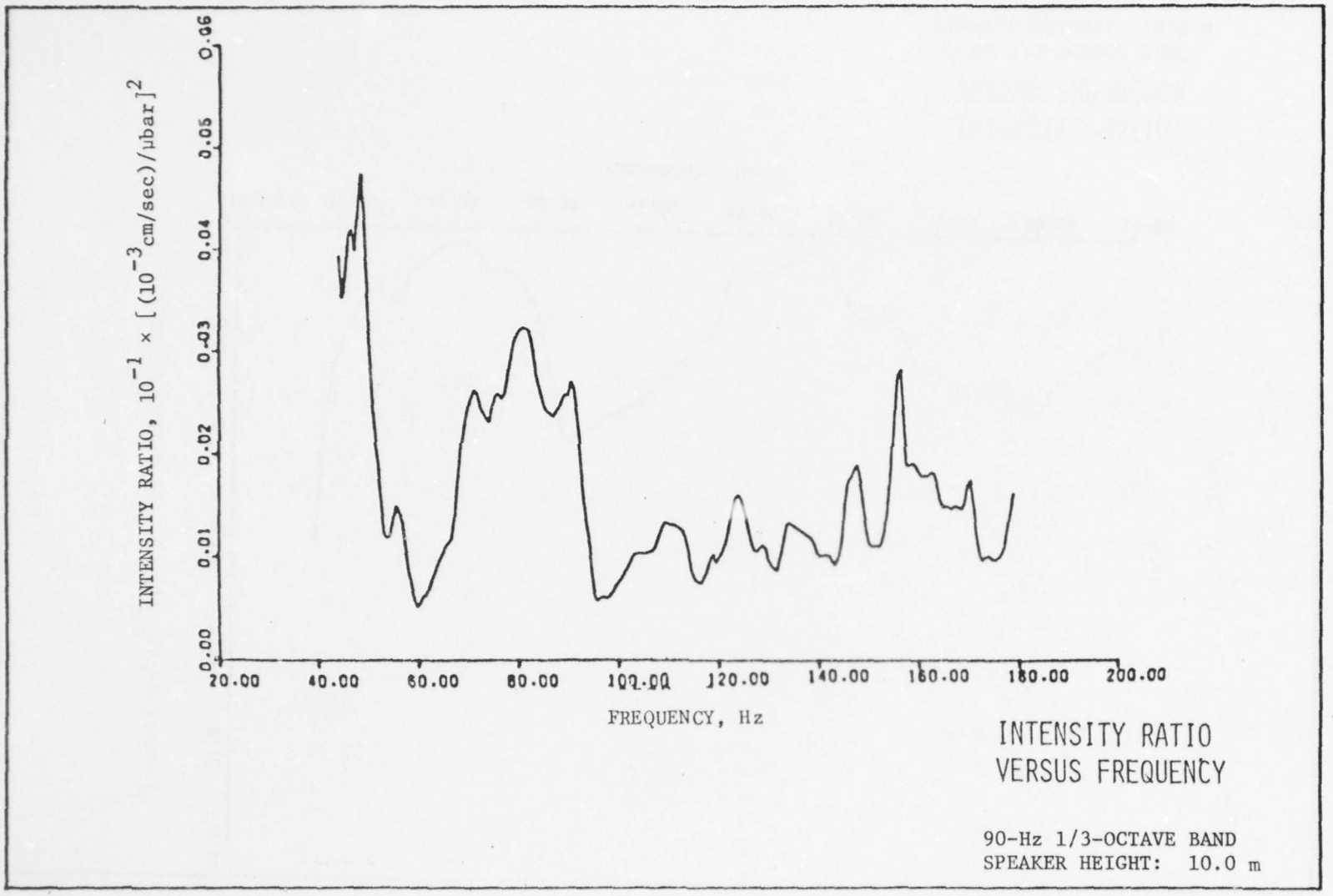
INTENSITY RATIO, $10^{-1} \times [(10^{-3}$cm/sec)/μbar$]^2$
0.00
0.01
0.02
0.03
0.04
0.05
0.06
20.00
40.00
60.00
80.00
100.00
120.00
140.00
160.00
180.00
200.00
FREQUENCY, Hz
INTENSITY RATIO
VERSUS FREQUENCY
90-Hz 1/3-OCTAVE BAND
SPEAKER HEIGHT: 10.0 m

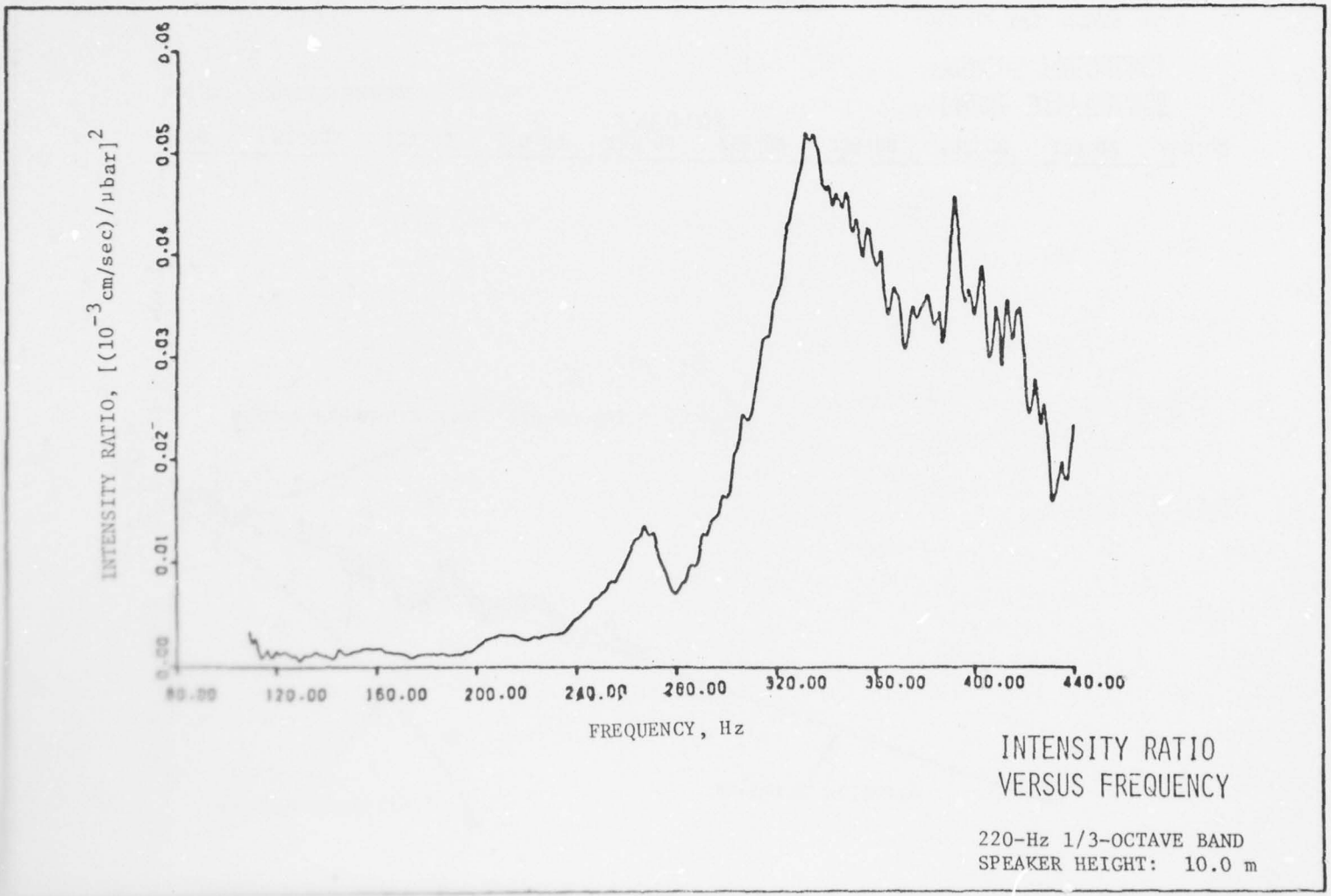

INTENSITY RATIO
VERSUS FREQUENCY

220-Hz 1/3-OCTAVE BAND
SPEAKER HEIGHT: 10.0 m

AD-A067 348 ARMY ENGINEER WATERWAYS EXPERIMENT STATION VICKSBURG MISS F/G 17/1
ACOUSTIC-TO-SEISMIC COUPLING: PROPERTIES AND APPLICATIONS TO SE--ETC(U)
FEB 79 M D FLOHR, D H CRESS

UNCLASSIFIED WES-TR-EL-79-1 NL

2 OF 2
AD
A067348

END
DATE
FILMED
6-79
DDC

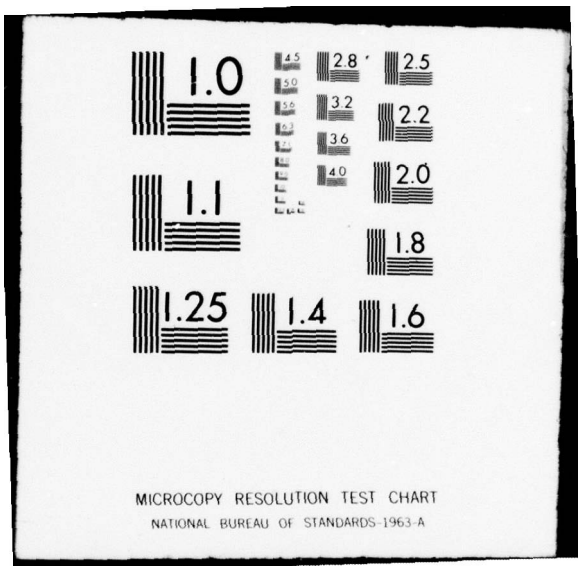
1.0
1.1
1.25
1.4
1.6
1.8
2.0
2.2
2.5
2.8
3.2
3.6
4.0
4.5
5.0
5.6
MICROCOPY RESOLUTION TEST CHART
NATIONAL BUREAU OF STANDARDS-1963-A

PLATE 16

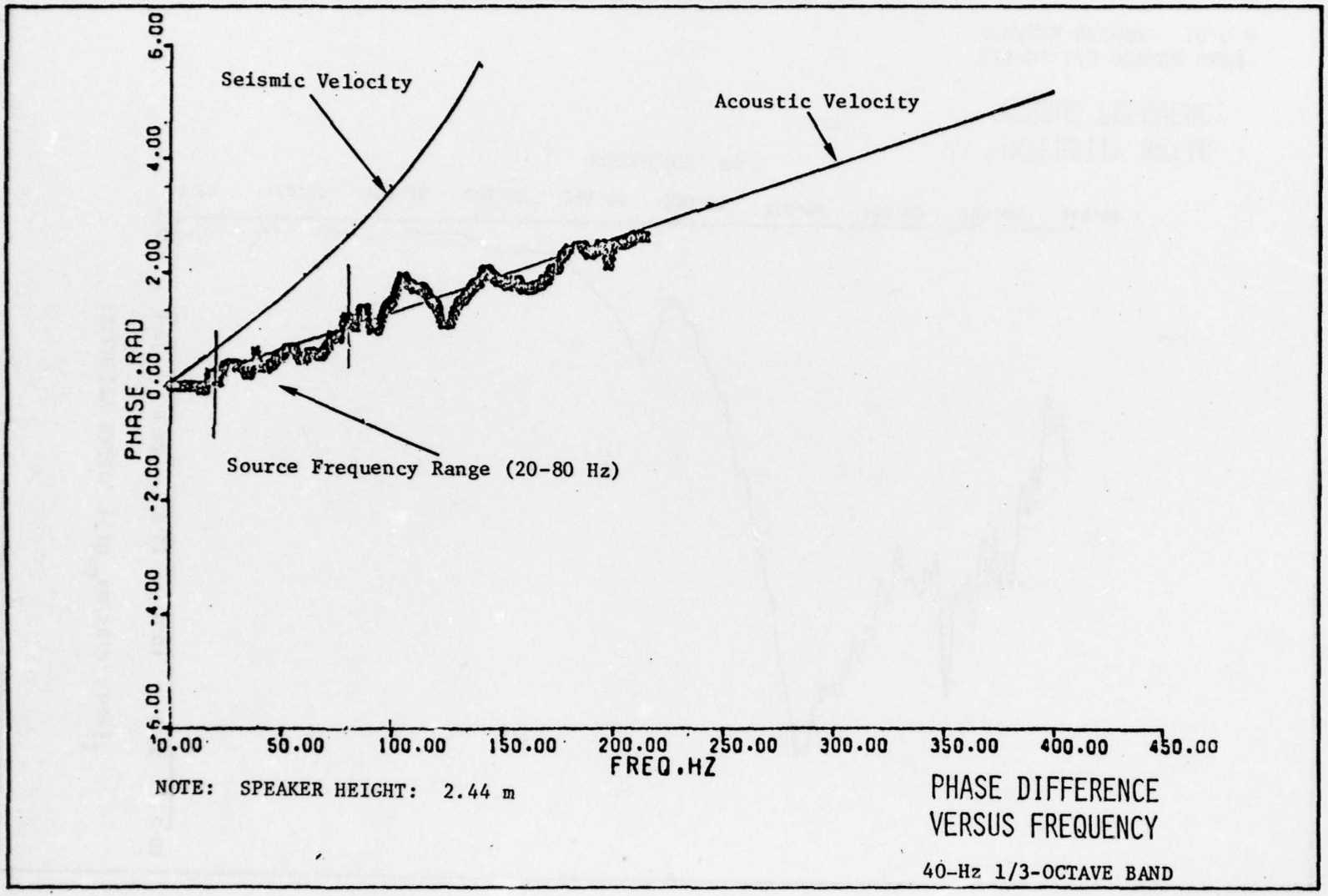

NOTE: SPEAKER HEIGHT: 2.44 m

PHASE DIFFERENCE
VERSUS FREQUENCY

40-Hz 1/3-OCTAVE BAND

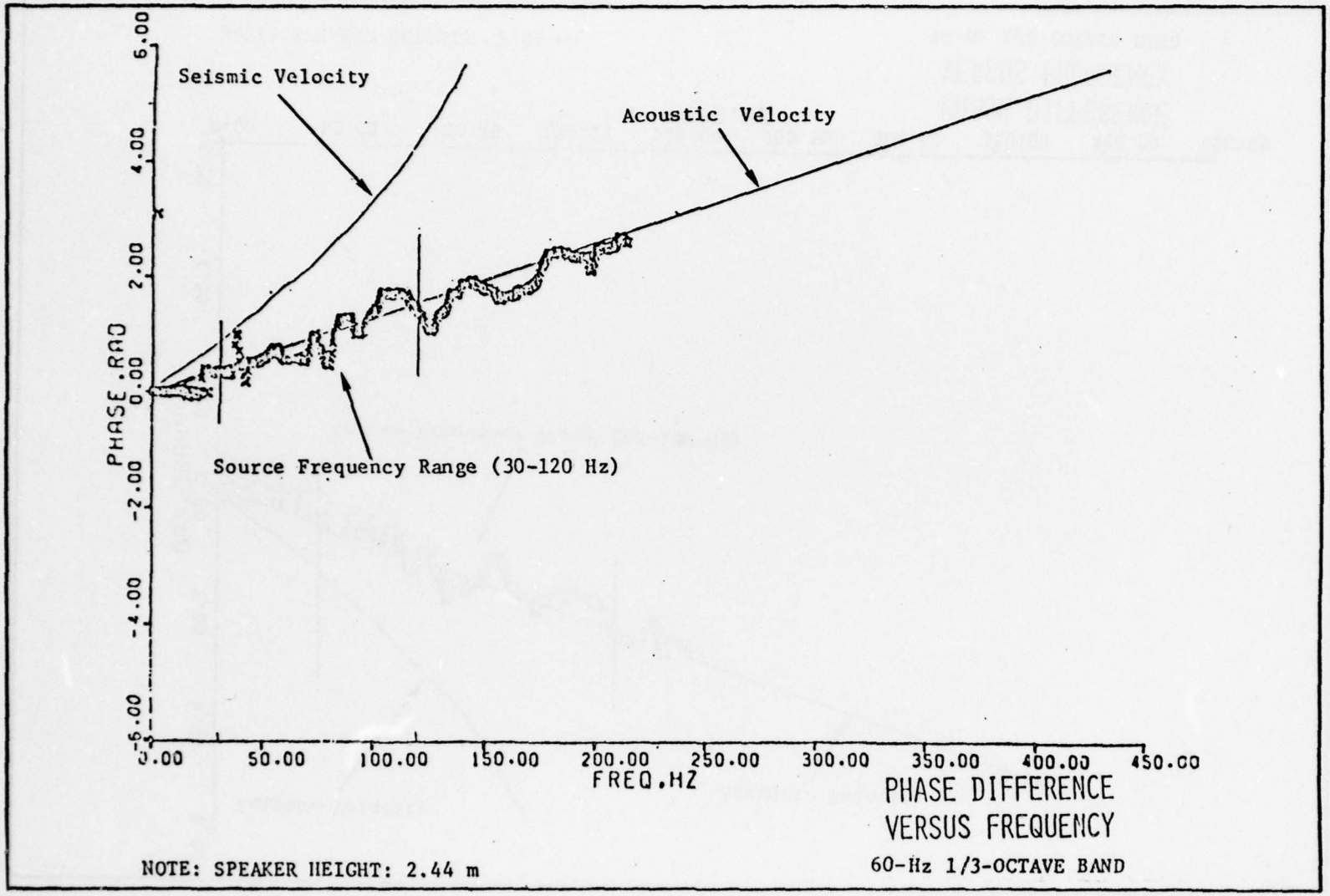

PHASE DIFFERENCE
VERSUS FREQUENCY

60-Hz 1/3-OCTAVE BAND

NOTE: SPEAKER HEIGHT: 2.44 m

PLATE 17

PLATE 18

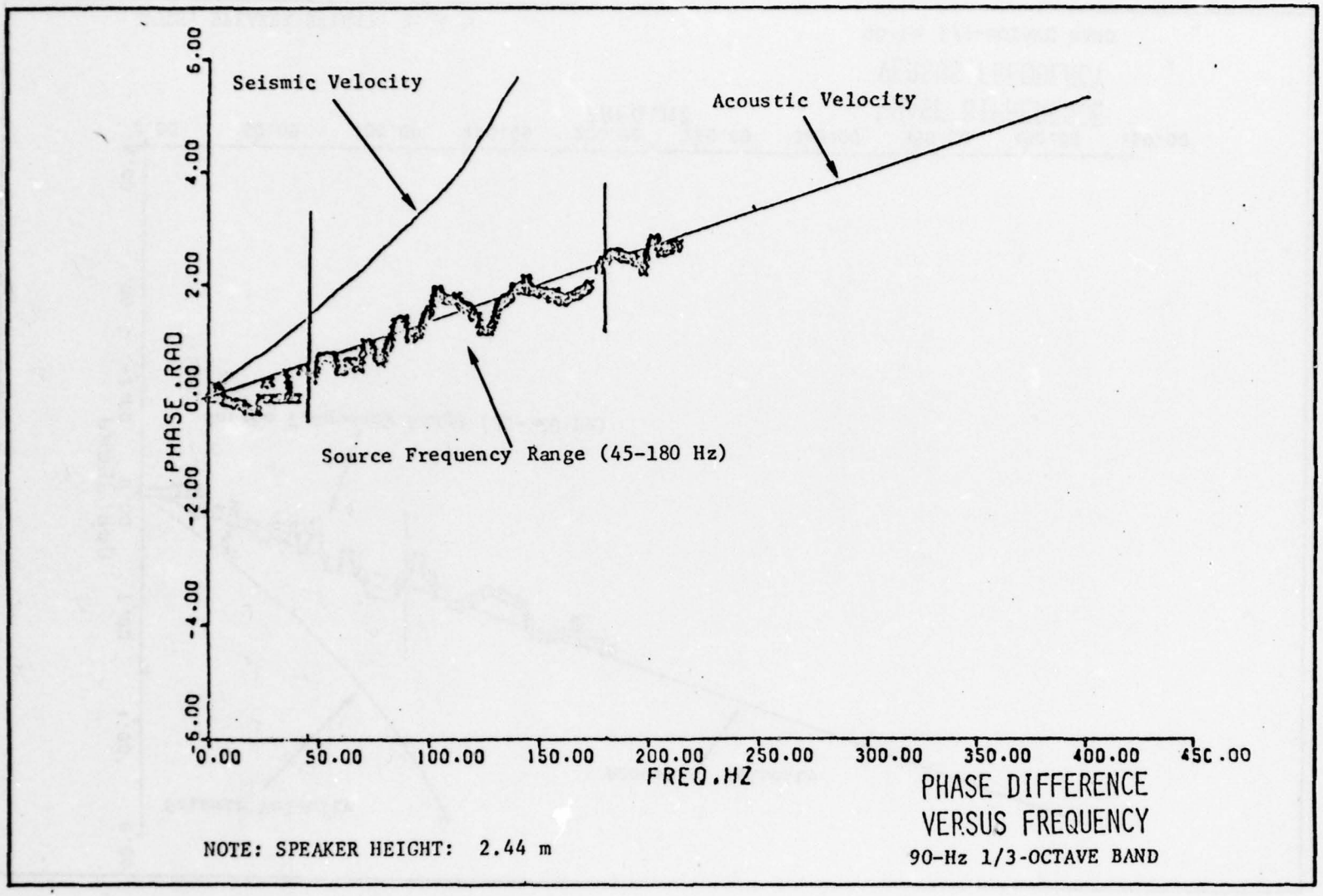

NOTE: SPEAKER HEIGHT: 2.44 m

PHASE DIFFERENCE
VERSUS FREQUENCY
90-Hz 1/3-OCTAVE BAND

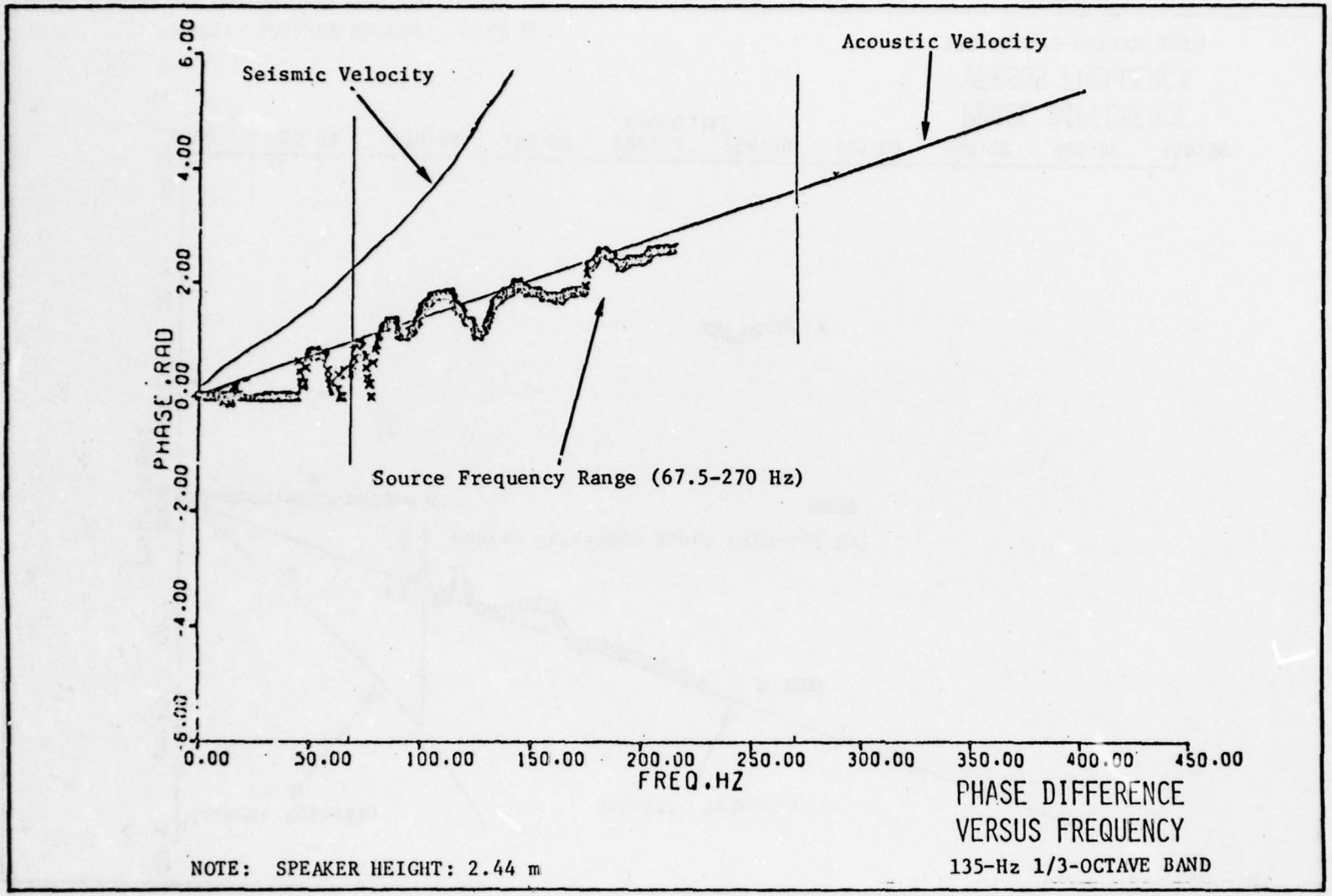

PHASE DIFFERENCE VERSUS FREQUENCY

135-Hz 1/3-OCTAVE BAND

NOTE: SPEAKER HEIGHT: 2.44 m

PLATE 19

PLATE 20

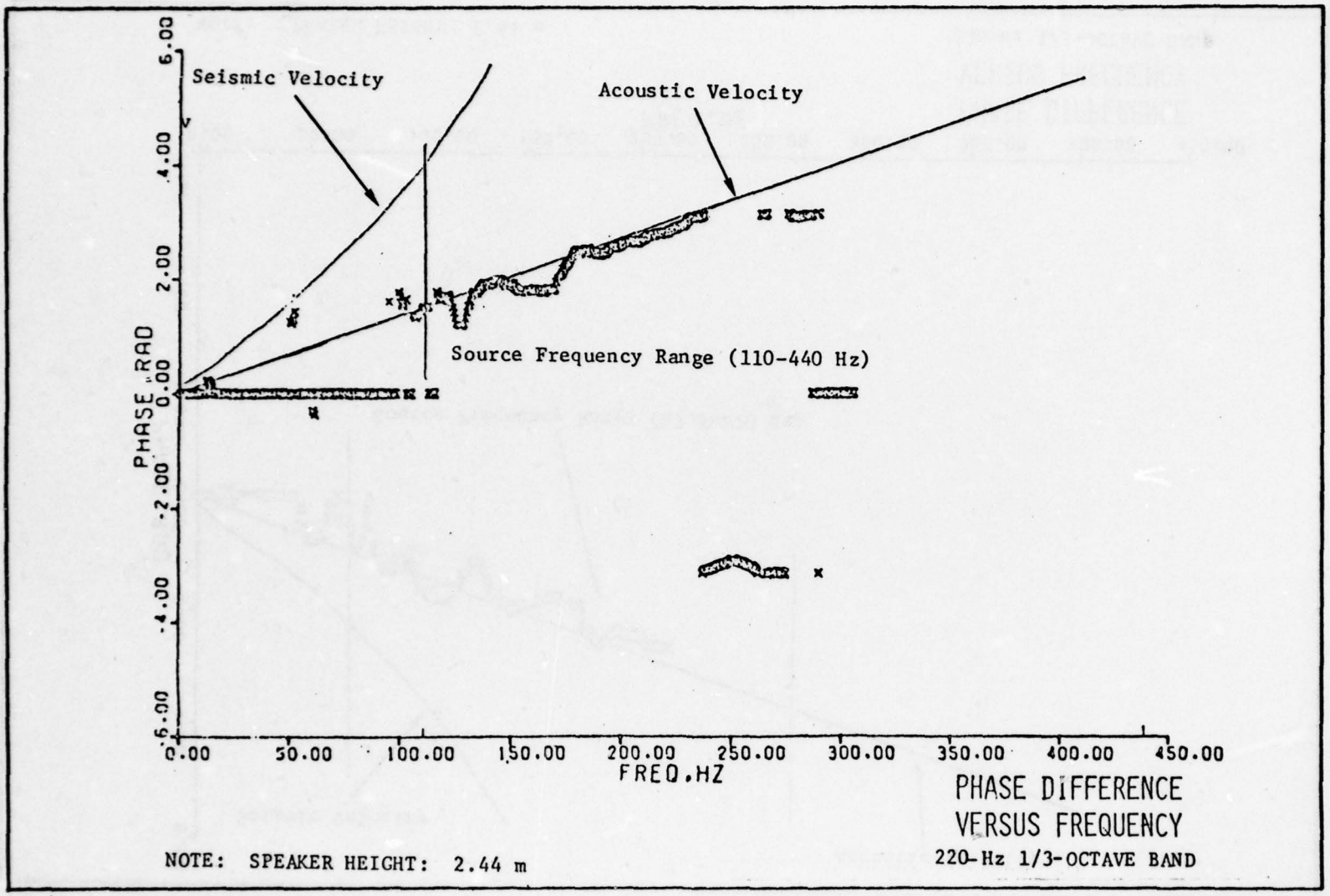

PHASE DIFFERENCE
VERSUS FREQUENCY
220-Hz 1/3-OCTAVE BAND

NOTE: SPEAKER HEIGHT: 2.44 m

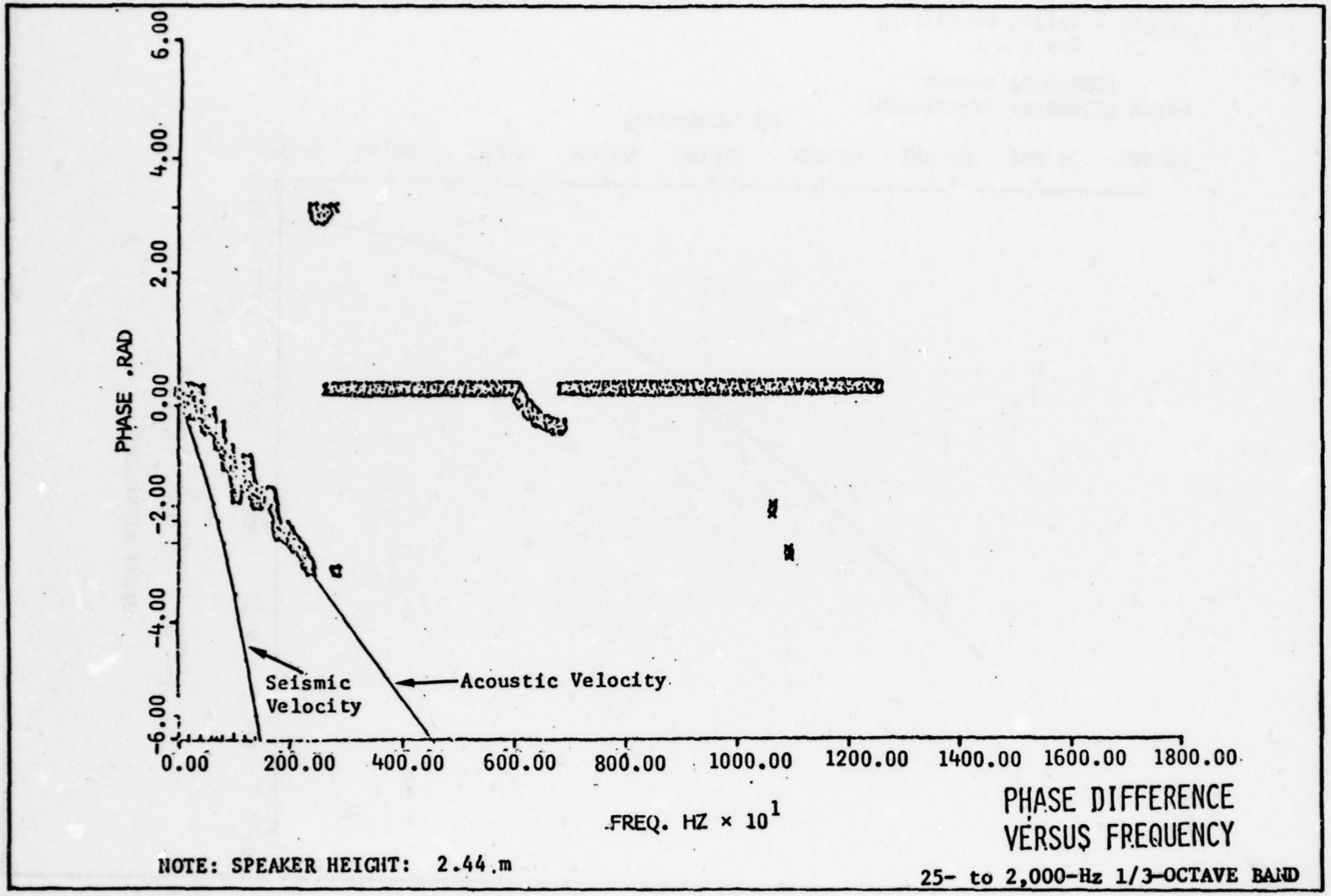
PHASE .RAD
6.00
4.00
2.00
0.00
-2.00
-4.00
-6.00
0.00
200.00
400.00
600.00
800.00
1000.00
1200.00
1400.00
1600.00
1800.00
Seismic Velocity
Acoustic Velocity
FREQ. HZ × 10^1
NOTE: SPEAKER HEIGHT: 2.44 m
PHASE DIFFERENCE VERSUS FREQUENCY
25- to 2,000-Hz 1/3-OCTAVE BAND

PLATE 21

PLATE 22

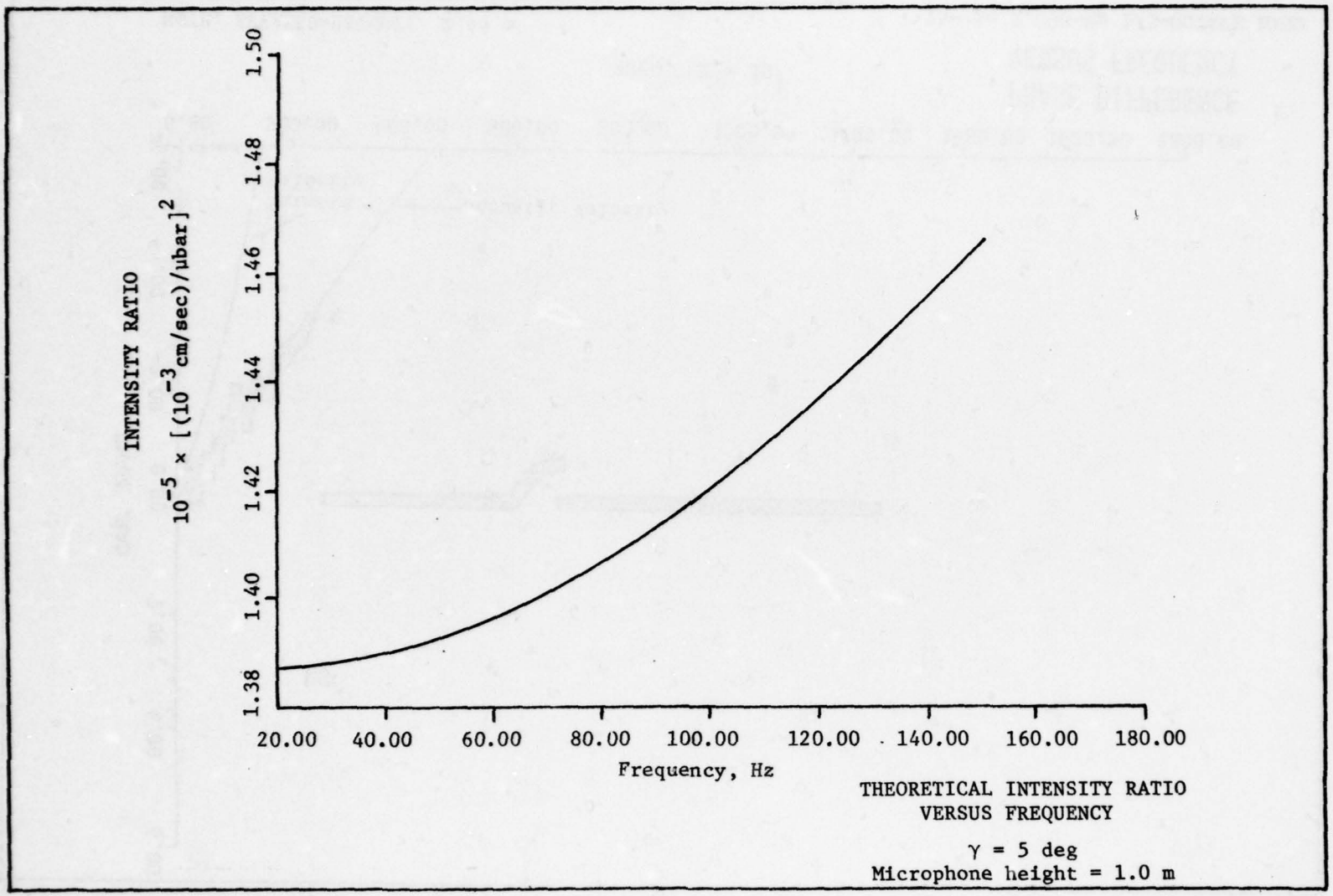

THEORETICAL INTENSITY RATIO
VERSUS FREQUENCY

γ = 5 deg
Microphone height = 1.0 m

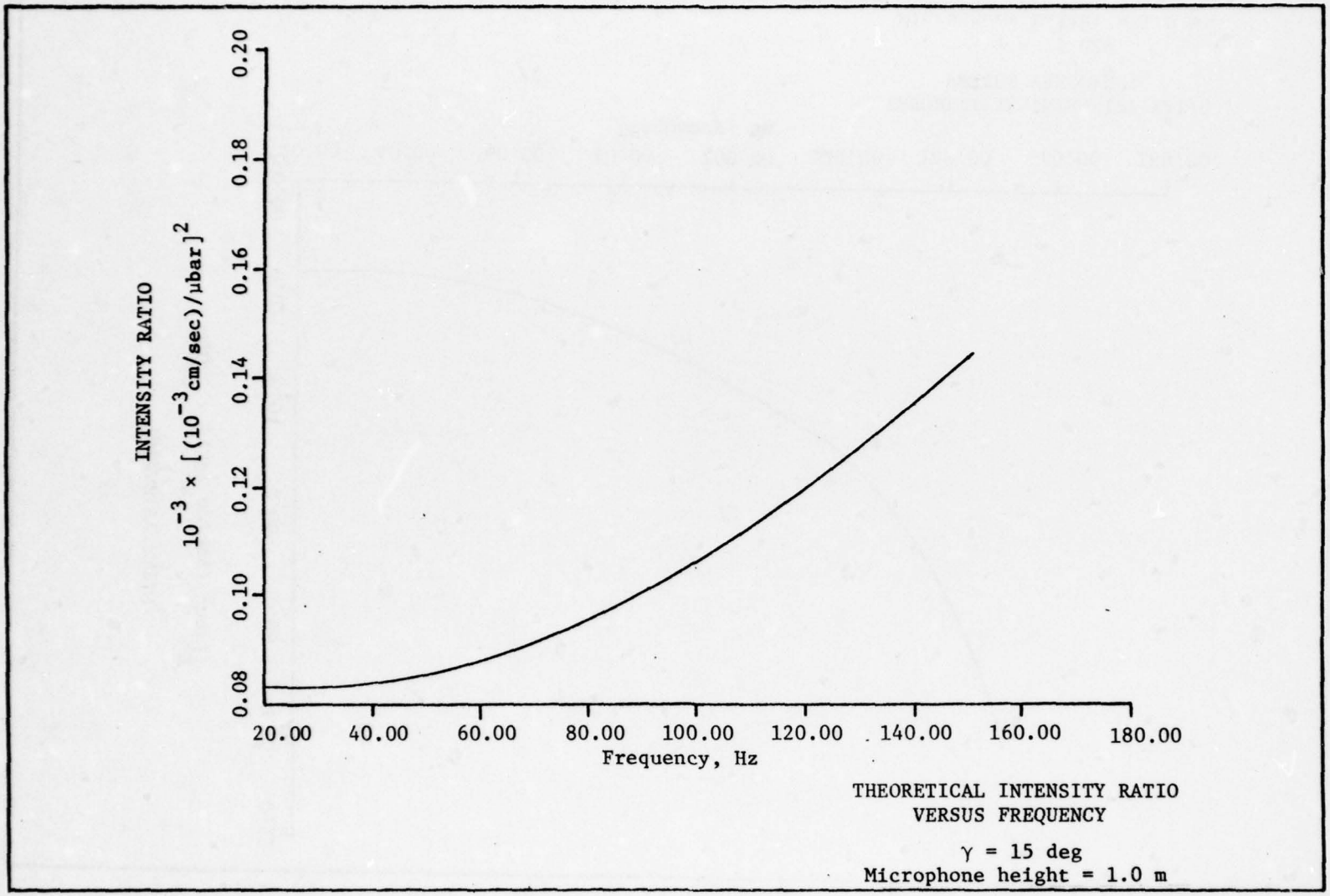

THEORETICAL INTENSITY RATIO
VERSUS FREQUENCY

γ = 15 deg
Microphone height = 1.0 m

PLATE 23

PLATE 24

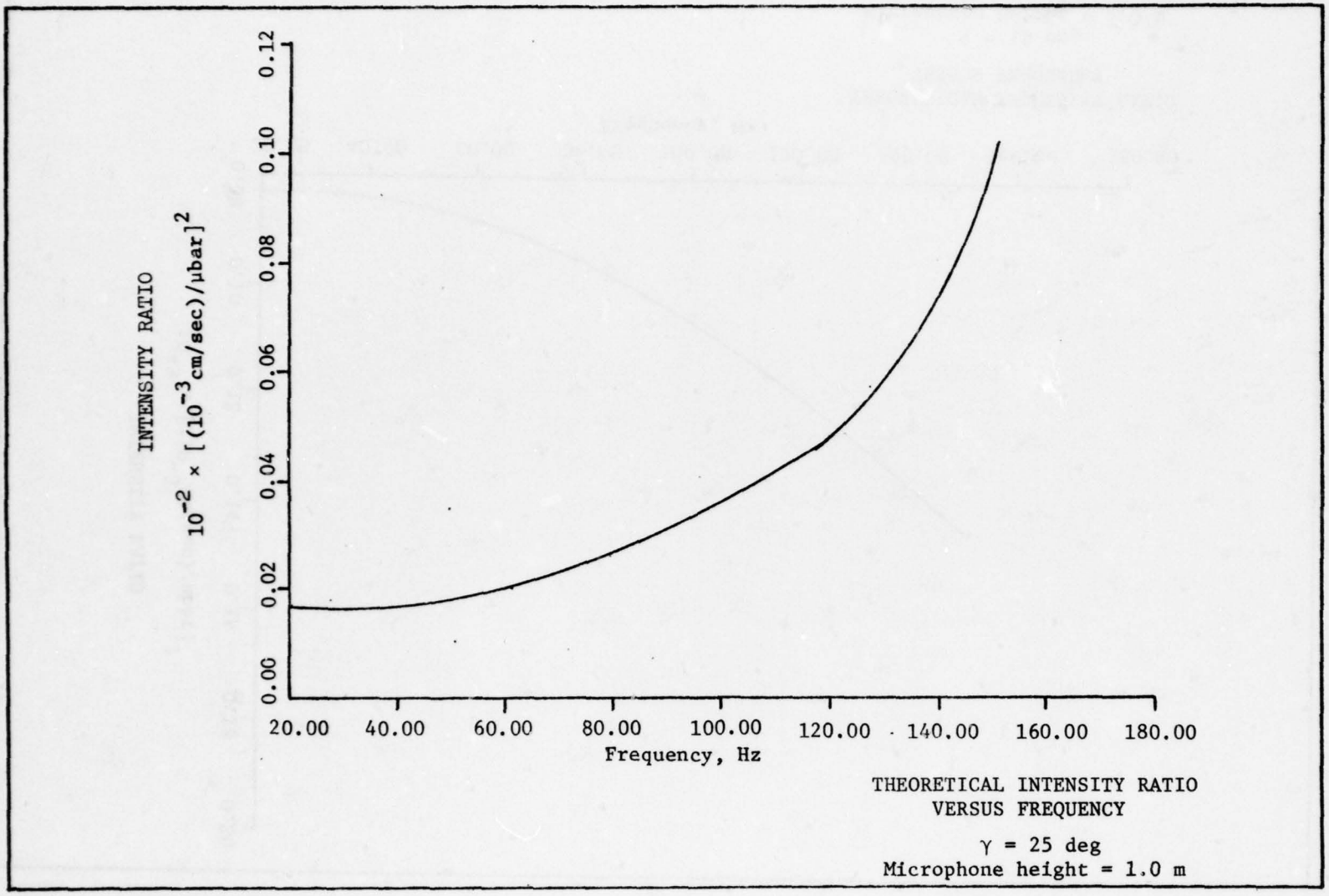

THEORETICAL INTENSITY RATIO
VERSUS FREQUENCY

γ = 25 deg
Microphone height = 1.0 m

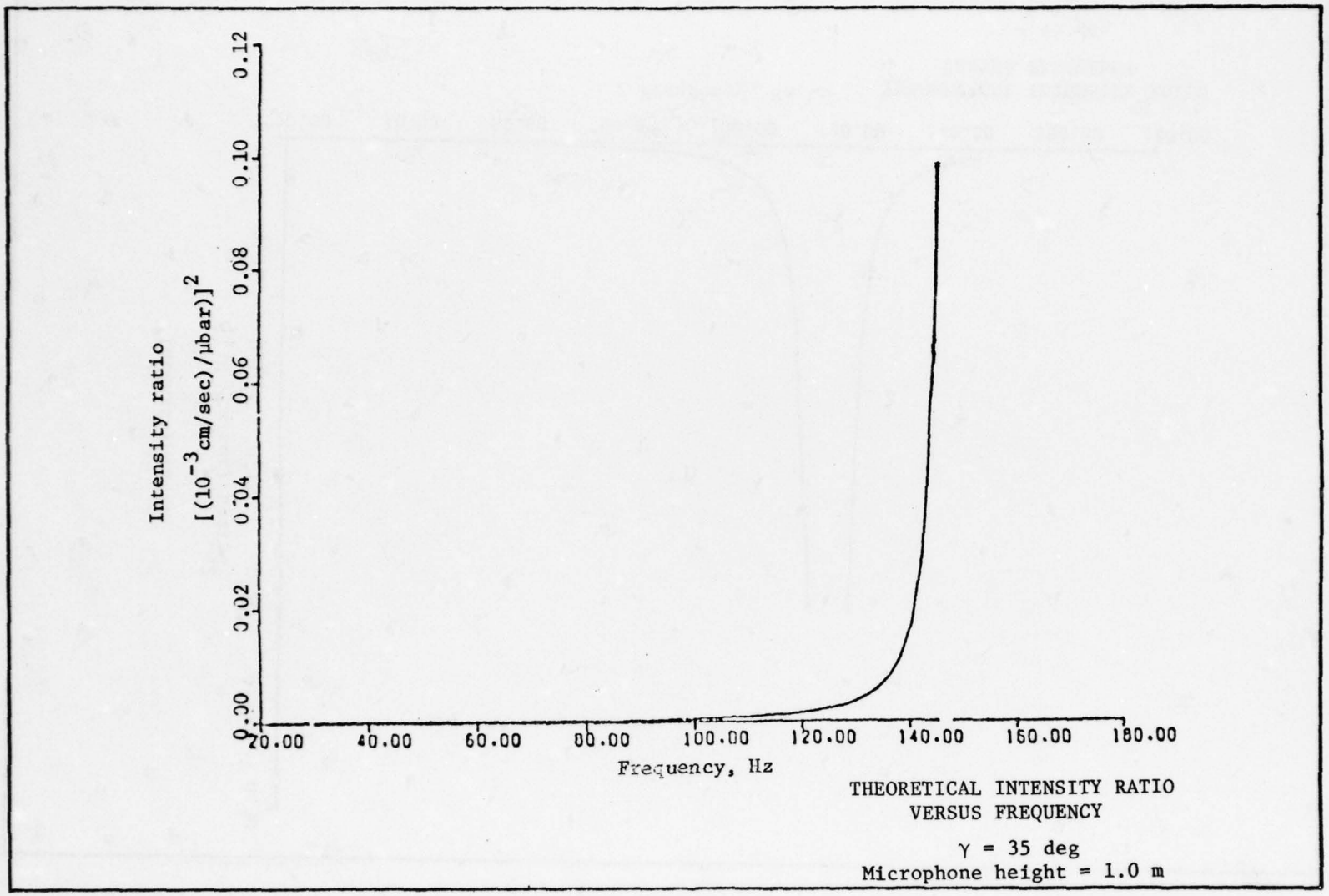

THEORETICAL INTENSITY RATIO
VERSUS FREQUENCY

γ = 35 deg
Microphone height = 1.0 m

PLATE 25

Intensity ratio
[(10⁻³cm/sec)/μbar]²
0.00
0.05
0.10
0.15
0.20
0.25
0.30
20.00
40.00
60.00
80.00
100.00
120.00
140.00
160.00
180.00
Frequency, Hz
THEORETICAL INTENSITY RATIO
VERSUS FREQUENCY
γ = 45 deg
Microphone height = 1.0 m

PLATE 26

APPENDIX A: MATHEMATICAL METHODS

1. The major effort in the evaluation of the test data is determining the spectral properties of acoustic and seismic signatures. By using the Fast Fourier Transform (FFT), the frequency domain representation of a measured signal can be obtained. The time domain signatures $x(t)$ and $y(t)$ for two sensors can be transformed (using complex numbers) to:

$$\tilde{X}_k = \Delta t \sum_{m=0}^{n-1} x_m \exp(-i2\pi f_k m\Delta t)$$

$$\tilde{Y}_k = \Delta t \sum_{m=0}^{n-1} y_m \exp(-i2\pi f_k m\Delta t) \qquad \text{(A1)}$$

where

$\tilde{X}_k$ and $\tilde{Y}_k$ = complex variables

Δt = sampling period

x_m and y_m = $x(m\Delta t)$ and $y(m\Delta t)$

$i = \sqrt{-1}$

f_k = k^{th} frequency value

The real part of $\tilde{X}_k$ (or $\tilde{Y}_k$) denotes that part of $x(t)$ (or $y(t)$) that can be associated with the cosine terms in Fourier expansion, while the imaginary part can be associated with the sine terms in the Fourier expansion. The tildes over $\tilde{X}_k$ and $\tilde{Y}_k$ indicate that $\tilde{X}_k$ and $\tilde{Y}_k$ are "raw" or unaveraged values. Values averaged over several frequencies will be denoted with a circumflex (^).

2. Before the Fourier transform was made, the data were smoothed at both ends of the time-sampled record. This was done to avoid effects of discontinuities or large amplitude changes. The smoothing function used was:

$$s(t) = \sin^2\left(\frac{2\pi t}{0.1T}\right);\ 0 \leq t \leq 0.1T$$

$$s(t) = \sin^2\left[\frac{2\pi(T - t)}{0.0T}\right];\ 0.9T \leq t \leq T \tag{A2}$$

where

$s(t)$ = smoothing function

t = time

T = length of record

This function was applied for the first one-tenth and last one-tenth of the data sample as shown. After the FFT was made, the values were adjusted to give the amplitude at each frequency rather than an amplitude for each frequency interval, which is dependent on the sampling rate and the number of points chosen for the FFT calculation.

3. The cross-spectral density estimate, G_{xyk}, is obtained from $\tilde{X}_k$ and $\tilde{Y}_k$, using the defining expression:

$$\tilde{G}_{xyk} = \tilde{X}_k^* \tilde{Y}_k \tag{A3}$$

where the asterisk denotes a complex conjugate. The resulting expression for G_{xyk} can be separated into real and imaginary parts in the form:

$$\tilde{G}_{xyk} = \tilde{C}_{xyk} - j\,\tilde{Q}_{xyk} \tag{A4}$$

where

$\tilde{C}_{xyk}$ = the cospectrum estimate

$\tilde{Q}_{xyk}$ = the quadrature spectrum estimate

The power spectrum, or autospectrum, is estimated for both $x(t)$ and $y(t)$ from the expressions:

$$G_{xk} = X_k^* X_k$$

and (A5)

$$G_{yk} = Y_k^* Y_k$$

The raw cross-spectral estimates were smoothed over seven adjacent estimates using the expressions:

$$\hat{G}_{xk} = \frac{1}{M} \sum_{j=1}^{7} G_{x(k+j-4)} W_j$$

$$\hat{G}_{yk} = \frac{1}{M} \sum_{j=1}^{7} G_{y(k+j-4)} W_j \qquad \text{(A6)}$$

$$\hat{G}_{xyk} = \frac{1}{M} \sum_{j=1}^{7} G_{xy(k+j-4)} W_j$$

$$\hat{G}_{xyk} = \hat{C}_{xyk} - j\hat{Q}_{xyk}$$

where

$W_j = 1, 2, 4, 6, 4, 2, 1$ for $j = 1, 2, 3, 4, 5, 6, 7$, respectively

$M = \sum_{j=1}^{7} ; W_j = 20$

4. The phase difference, ϕ_{xyk}, between time series $x(t)$ and $y(t)$ was estimated from the expression:

$$\phi_{xyk} = \arctan\left(\frac{\hat{Q}_{xyk}}{\hat{C}_{xyk}}\right) \qquad \text{(A7)}$$

The time delay between $x(t)$ and $y(t)$ for each frequency can be obtained using

$$\Delta t = \frac{\phi_{xyk}}{\omega_k} \qquad \text{(A8)}$$

where

Δt = time delay

ω_k = frequency index by k

An additional parameter having useful properties for the application of the computational technique to time-delay estimate, or equivalently, estimates of phase difference, is the squared coherence, γ^2_{xy}. This parameter is defined in terms of the cross-spectrum $G_{xy}(f)$ and the autospectrum $G_x(f)$ and $G_y(f)$ as:

$$\gamma^2_{xy}(f) = \frac{\left|G_{xy}(f)\right|^2}{G_x(f)G_y(f)} \tag{A9}$$

The coherence estimate can be expressed in terms of the previously obtained estimates of auto- and cross-spectra as:

$$\gamma^2_{xy} = \frac{\left|\hat{G}_{xyk}\right|^2}{\hat{G}_{xk}\hat{G}_{yk}} = \frac{\hat{C}^2_{xyk} + \hat{Q}^2_{xyk}}{\hat{G}_{xk}\hat{G}_{yk}} \tag{A10}$$

5. The squared coherence, calculated using the weighted averaged (Equation A6) values of the cospectra, quadspectra, and autospectra, is a measure of the amount of noise present in signals received by the sensor. The coherence value may be lowered by nonlinearities of the system, but it was assumed that for the short ranges (less than 10 m), seismic and acoustic propagation is linear. Noise in the signal will produce random phase differences between adjacent frequency intervals, as opposed to a linearly increasing or decreasing phase difference expected because of the time delay between sensors.

6. An illustration of the dependence of the squared coherence value on the amount of noise present in the signal is shown in Figure A1. In this figure, coherence is plotted as a function of the variance of a random distribution of phases. The phase values were generated by a random number generator (computer software package at WES) that gives a set of numbers with zero mean and unit standard deviation. Other values of standard deviation were obtained by multiplying this set by the standard deviation desired. The data set sampled for each point of this plot consisted of 210 numbers. A coherence value was calculated

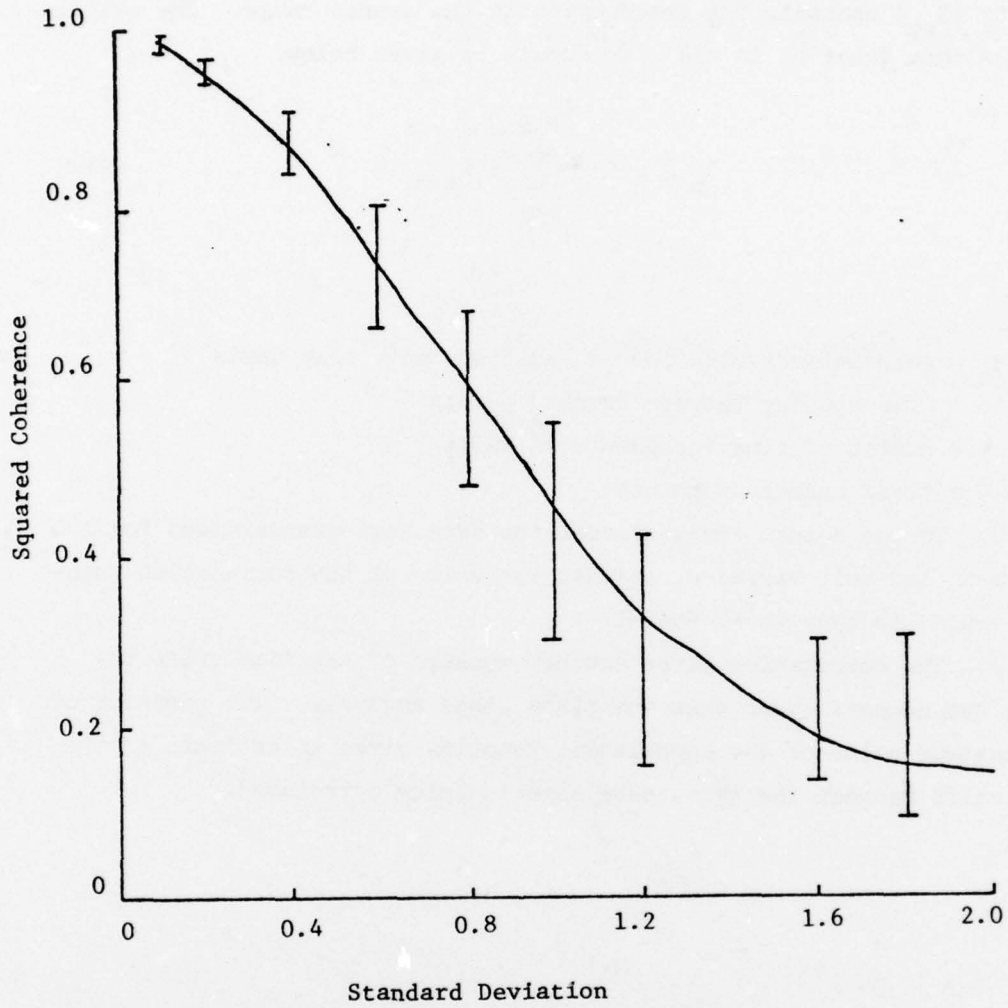

Figure A1. Dependence of squared coherence computation on statistical distribution of phases (50 percent confidence limits indicated by bars)

for thirty consecutive groups of seven numbers using the same weighting that was used in the test data analysis (see Equation A6). The bars shown on the plot of Figure A1 estimate the range of squared coherence values within 50 percent confidence limits. These confidence limits show that squared coherence values below 0.5 are not very meaningful since there may be too much noise in the system.

7. Another useful function is the cross-correlation function. This was calculated by taking the inverse FFT of the cross-spectral

density (G_{xy}) estimate for frequencies in the source range. The calculation of this function in the time domain is given below.

$$R_m = \frac{1}{N - m} \sum_{i=1}^{N-m} y_i x_{i+m} \qquad \text{(A11)}$$

where

R_m = correlation value for x shifted $m\Delta t$ time units

Δt = time spacing between sampled points

m = number of time increments in shift

N = total number of points

8. In the actual computations, the data were standardized for zero mean and unit variance, so that the value of the correlation function would lie between +1 and -1.

9. The correlation gives another measure of the time shift between two sensors other than the phase slope analysis. The position of the maximum value of the correlation function gives an estimate of the time shift between the two sensor signals being correlated.

APPENDIX B: ACOUSTIC WAVES AT BOUNDARIES

Introduction

1. The propagation of an acoustic wave in the vicinity of a boundary can be represented by Figure B1,

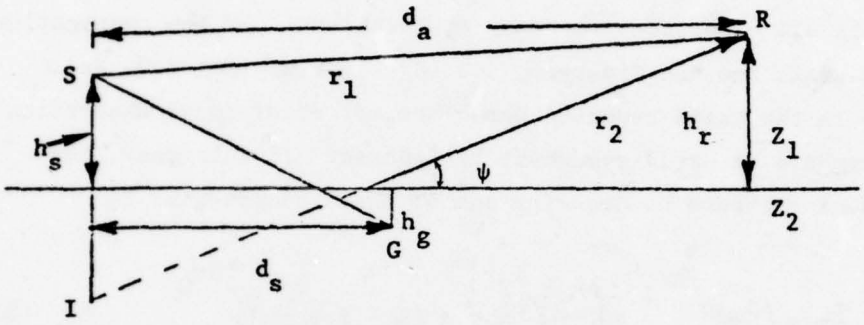

Figure B1. Direct and reflected paths for impedance measurements

where

S = the source

I = the image of the source due to reflection from the boundary

R = acoustic receiver

G = a geophone

h_s = source height

d_s = distance along ground from source to geophone

d_a = distance along ground from source to acoustic receiver

r_1 = distance for direct propagation from source to acoustic receiver

r_2 = distance for reflected propagation from image of source to receiver

ψ = angle of reflection

h_g = depth of geophone

h_r = height of acoustic receiver

Z_1 = acoustic impedance of medium one (assumed to be air)

Z_2 = acoustic impedance of medium two (assumed to be the ground)

2. The following section will be devoted to the development of

the equations that describe an acoustic wave received at point R for the special conditions of importance to this study. The limiting case of plane wave propagation will also be considered.

Spherical Sound Source

3. The source of acoustic energy can be assumed to radiate symmetrically in all directions for many applications. If the propagation distance is small and the frequency low ($d_a < 300$ m, $f < 1000$ Hz), as was true in the tests reported here, the effect of sound absorption by the atmosphere is small enough to be ignored. In this case, the acoustic sound pressure becomes the sum of three components:[6]*

$$\frac{p}{p_o} = \left(\frac{1}{r_1}\right)e^{ikr_1} + \left(\frac{R_p}{r_2}\right)e^{ikr_2} + \left(1 - R_p\right)\left(\frac{F}{r_2}\right)e^{ikr_2} \qquad \text{(B1)}$$

where

p = acoustic sound pressure at the receiver

p_o = acoustic sound pressure at the source

r_1 = distance defined in Figure B1

k = acoustic wave number

R_p = plane wave reflection coefficient = $\dfrac{\sin \psi - Z_1/Z_2}{\sin \psi + Z_1/Z_2}$

r_2 = distance defined in Figure B1

F = factor that accounts for spherical nature of source

4. The first term on the right side in Equation B1 represents direct transmission to the receiver. The second term would be the reflection in the case of plane waves. For small angles of incidence or large propagation distances, $R_p \cong -1$ and the first two terms cancel. In this case, the received acoustic signal is dominated by the third term. For an air-ground interface, at frequencies below 100 Hz,

---

* Superscript numerals in this appendix and subsequent appendixes refer to numbered sources listed in the References section, which appears at the end of the main text.

$Z_1/Z_2 << 1$; so for angles of incidence no greater than a few degrees, R_p is negative and the final term dominates the received signal.

5. The solution of Equation B1 for the sound pressure in the vicinity of a boundary reduces to the evaluation of the factor F in Equation B2, which is given by Reference 6:

$$F = 1 + 2i\omega^{1/2} \exp(-\omega) \int_{-i\omega^{1/2}}^{\infty} \exp(-u^2)du \qquad \text{(B2)}$$

where

ω = numerical distance = $ikr_1\left[\sin \psi + (Z_1/Z_2)\right]^2/2$

When the microphone is on the ground, the first two terms on the right side in Equation B1 vanish. For these conditions, Embleton, Piercy, and Olson[6] have shown that

$$\frac{p}{p_o} \cong -\exp(ikr)\left(\frac{ik}{\gamma^2 r^2}\right)\left[2 - 2\gamma h + \gamma^2\left(h_s^2 + h_r^2\right)\right] + \left\{\varepsilon i 2\pi\gamma \exp(-\gamma h)\, H_o^{(1)}\left[(k^2 + \gamma^2)^{1/2} r\right]\right\} \qquad \text{(B3)}$$

where

$r = r_1 \cong r_2$

$\gamma = ikZ_1/Z_2 = \alpha + i\beta$ (defines α and β)

$h = h_r + h_s$

$\varepsilon = 1$ if $\beta \geq 0$, $0 \geq \alpha \geq \beta\,(1 + \beta^2/k^2)^{-1/2}$, otherwise $\varepsilon = 0$

$H_o^{(1)}$ = Hankel function

The first term in Equation B3 falls off as r^{-2} and represents the ground wave, which is analogous to the wave that carries AM radio broadcasts along a surface. The second term decreases exponentially with height above the ground and is referred to as the surface wave. Although Equation B3 is valid only when $r_1 = r_2$, for other cases, the integral in Equation B2 can be separated into terms that diminish as r^{-1} (surface wave) and r^{-2} (ground wave); hence these two contributions can be mathematically separated in all cases.[7]

6. We have now introduced four types of waves that will impinge on the acoustic receiver: the direct wave (D), the plane reflected wave (R), the ground wave (G), and the surface wave (S). For typical ground, the relative contribution from these four waves is given in Figure B2. The important feature to note is that for short propagation distances (d = 100 ft), the received acoustic energy is dominated by the direct

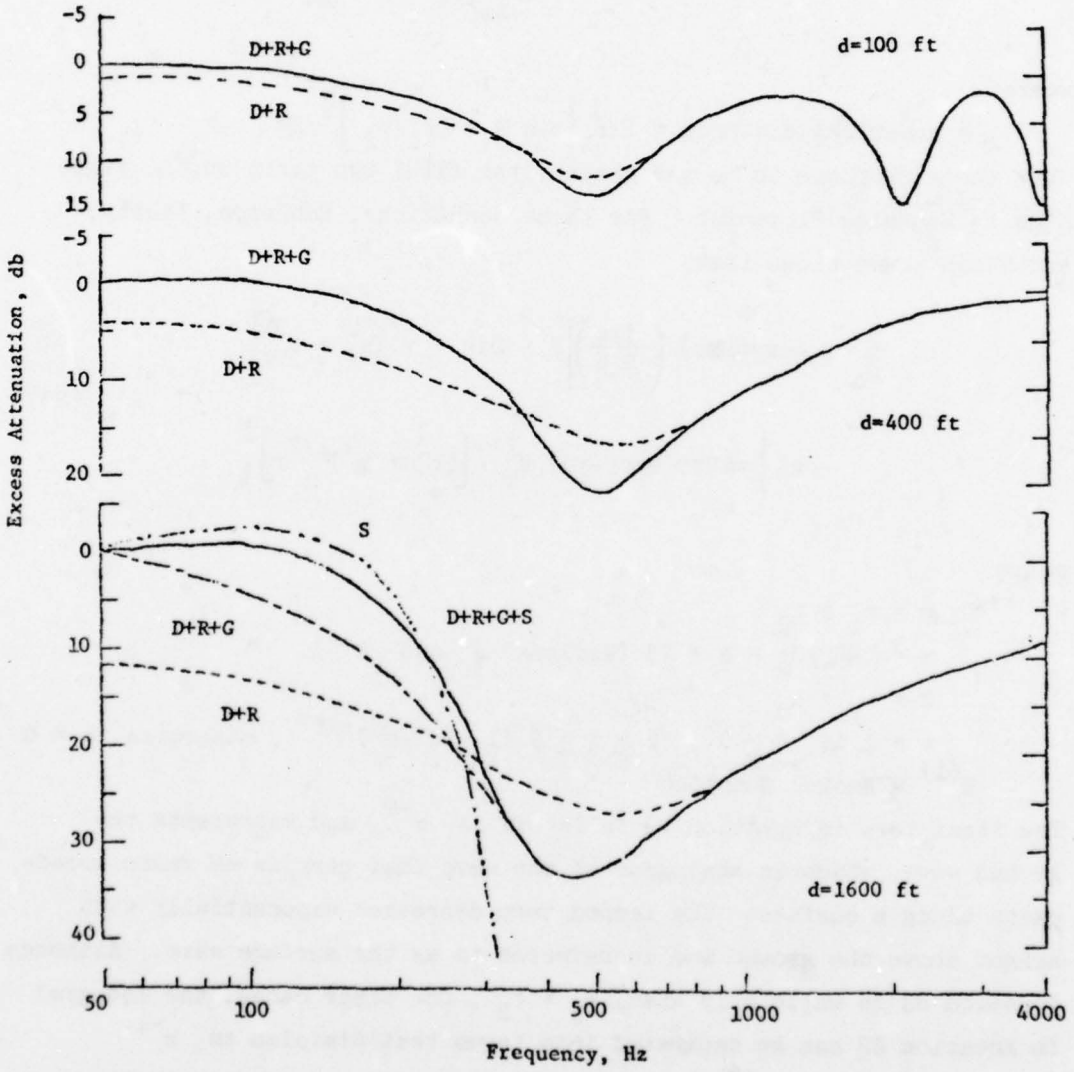

Figure B2. Relative contribution to measured acoustic signal (from Reference 8)

plus plane reflected wave (D + R). At 400 ft, the contribution of the ground wave (D + R + G) becomes measurable, but the surface wave is dominant only at ranges of several hundred feet (and microphone placements much closer to the ground than 5 ft). This report is concerned primarily with propagation distances less than 200 ft; hence it is reasonable to expect that the measured acoustic field will be accurately represented by the D + R curve (except, perhaps, when the microphone is on the ground). If this is the case, then the problem can be reduced to one of plane waves interacting with the surface with little error.

7. A computer program has been developed by Donato[7] to evaluate the integral in Equation B2 and identify the four types of waves that contribute to the received acoustic signal. This program has been adapted to the UM Dec 1077 computer. In order to use the program, the frequency, source and receiver heights, propagation distance, and surface impedance must be known. All these parameters, except surface impedance, are determined experimentally. To determine the surface impedance, the received acoustic amplitude is measured as a function of receiver height and propagation distance. Then the surface impedance is adjusted to give agreement between the measured sound intensity at each distance/height combination and the computed values for the same combination. This process is repeated for each frequency considered (since Z is a function of frequency). The surface impedance, then, is that value of impedance necessary to obtain agreement between experimental measurements of the sound pressure and values computed using the theory outlined above.

8. The description of the acoustic field in the earth is complicated by the presence of several modes of propagation (paragraph 6, Appendix B). Although the mathematical form for the displacement of the earth due to a spherical acoustic source has been developed,[9] the results are not in a form amenable to analytical or numerical solution. Clearly, more work is needed in this area. Until a rigorous computational technique is available, an estimate of the displacement experienced by a seismic sensor due to an impinging acoustic wave cannot be made.

9. If a microphone is placed only a few centimetres from the

surface, the direct wave inpinging on the microphone will be approximately the same as the direct wave impinging on the earth below it. Thus, we can compute the energy that impinges the surface. Further, the energy received by the microphone due to the presence of the surface will be a sum of the plane reflected, ground, and surface waves. Experimentally, all these waves are combined, but as described above, mathematically each one can be identified separately; thus the ratio of incident energy to reflected acoustic energy (α) is equal to the ratio of the squares of the sound pressure. If the amplitude of the plane reflected plus ground plus surface waves is denoted as B and the direct wave as D, then

$$\alpha_r = \frac{B^2}{D^2} \tag{B4}$$

The transmission coefficient (α_t) is $1 - \alpha_r$, so that the acoustic power coupled into the earth is α_t times the incident acoustic power. For a plane acoustic wave, the incident intensity is given by $D^2/2\rho_1 c_1$, while the transmitted intensity is given by $\rho_2 c_2 u^2/2$ where $\rho_1 c_1$ and $\rho_2 c_2$ are the density and the sound velocity in the air and earth, respectively, and u is the displacement velocity. Then,

$$\frac{\alpha_t D^2}{2\rho_1 c_1} \approx \frac{\rho_2 c_2 u^2}{2} \tag{B5}$$

Equation B5 can then be used to solve for the displacement measured directly below the surface. It should be kept in mind that this is at best a crude approximation of the displacement. But in the absence of a vigorous formalism, this and a similar expression developed later for plane waves can provide some insight into the behavior of the received seismic signal.

Plane Wave Propagation Near a Surface

10. As noted in the previous section, for the range of parameters

considered in this study, plane wave theory provides a reasonable representation of the acoustic field above the surface. Since the mathematics associated with plane waves propagating through a boundary is relatively straightforward, it should be illuminating to consider the plane wave case. It is assumed that the sound intensity falls off, in essence, as r^{-2}, but by invoking plane wave theory it is assumed that no energy is transmitted via a ground or surface wave. This means that at some point below the surface all the energy comes along one refracted path.

11. Experimental measurements reviewed by Piercy and Sutherland[8] indicate that a grassy surface can be decribed well, assuming it is a locally (or normally) reacting porous medium. Such a description deep into the soil is probably much too simple, but since the geophones utilized for this study were near the surface, the locally reacting nature of the surface should suffice to describe the coupling into soil. For this case, it can be shown[3] that

$$\alpha_t = \frac{4R\,\rho_1 c_1 \cos\psi}{(R\cos\psi + \rho_1 c_1) + X^2\cos^2\psi} \tag{B6}$$

where R and X are the real and imaginary parts of the surface impedance, respectively. Using Equation B6 for α_t, Equation B5 can be used to compute u^2, i.e.,

$$u^2 = \frac{D^2}{\rho_2 c_2} \frac{4R\cos\psi}{(R\cos\psi + \rho_1 c_1) + X^2\cos^2\psi} \tag{B7}$$

There are two methods of determining R and X. One is to determine the values from seismic measurements and plane wave theory and Equation B7. The other is to use acoustic measurements above the surface and spherical wave theory (paragraphs 3-7). Table B1 shows impedances for several frequencies determined using these two methods.

Table B1

Impedance Determined from Different Approaches

Frequency Hz	Surface Measurements gm/cm^2/sec		Plane Wave Theory gm/cm^2/sec	
	Real	Imaginary	Real	Imaginary
63	8.3×10^2	4.0×10^2	2.2×10^4	2.2×10^4
125	6.2×10^2	4.0×10^2	1.9×10^4	1.9×10^4
250	4.2×10^2	3.7×10^2	7.8×10^3	7.8×10^3
500	2.9×10^2	3.7×10^2	2.3×10^4	2.3×10^4

APPENDIX C: THEORETICAL BACKGROUND

Introduction

1. In this appendix acoustic-to-seismic coupling will be determined for an idealized case approximating measured conditions of Test I at the 30-m location (see Figure 1 of the main text).

2. The intensity ratio will be calculated for the microphone at height z so that the results can be applied to both experimental setups (z = 1.0 m and z = 0.0 m). The latter case (z = 0.0 m) will not have interference effects between the direct and reflected acoustic waves because there is no reflected wave.

Plane Wave Approximation

3. An approximation[10] to the experimental conditions of Test I at the 30-m location is an incident compression (sound) wave consisting of plane wave fronts in the air with a plane interface with the ground. The ground will be approximated as an infinite half-space having a smooth surface and the same physical properties as those measured for the first layer.

4. The plane wave approximation of the quasi-spherical wave that is generated by the acoustic source is a good approximation at large distances from the source. Neglecting surface roughness introduces some error for small angles of incidence. The neglect of the second layer removes interference effects due to internal reflections.

Boundary Conditions (z = o)

5. Figure 25 shows the case to be analyzed with sensors at the origin. The boundary conditions are given below with u, v, and w representing displacement in the direction of the x, y, and z axis, respectively, and p_{xx}, p_{yy}, and p_{zz} representing stresses. Primed values are in ground, and unprimed values are in air.

$$w = w'$$

$$p_{zz} = p'_{zz} \tag{C1}$$

$$p_{zx} = p'_{zx} = 0$$

The displacements can be expressed in terms of scalar and vector potentials, ϕ and ψ, respectively, with

$$u = \frac{\partial \phi}{\partial x} + \frac{\partial \psi_3}{\partial y} - \frac{\partial \psi_2}{\partial z}$$

$$v = \frac{\partial \phi}{\partial y} + \frac{\partial \psi_1}{\partial z} - \frac{\partial \psi_3}{\partial x} \tag{C2}$$

$$w = \frac{\partial \phi}{\partial z} + \frac{\partial \psi_2}{\partial x} - \frac{\partial \psi_1}{\partial y}$$

The scalar and vector potentials satisfy the wave equations:

$$\nabla^2 \phi = \frac{1}{\alpha^2} \frac{\alpha^2 \phi}{\alpha t^2}$$

(C3)

$$\nabla^2 \psi_i = \frac{1}{\beta_i^2} \frac{\partial^2 \psi_i}{\partial t^2} \qquad (i = 1,2,3)$$

where

α = compression wave velocity

β_i = shear wave velocity for i^{th} component (i.e., i = 1 for x-direction, 2 for y, and 3 for z)

t = time

Since the plane wave shown in Figure 25 is independent of y, the C2 equations reduce to:

$$u = \frac{\partial \phi}{\partial x} - \frac{\partial \psi_2}{\partial z}$$

$$v = \frac{\partial \psi_1}{\partial z} - \frac{\partial \psi_3}{\partial x} \qquad \left[\text{SH wave (horizontal polarization)}\right] \qquad \text{(C4)}$$

$$w = \frac{\partial \phi}{\partial z} + \frac{\partial \psi_2}{\partial x}$$

Only compression and SV (vertically polarized) waves will be discussed here since SH waves were not analyzed experimentally. The subscript on ψ_2 can be dropped and

$$u = \frac{\partial \phi}{\partial x} - \frac{\partial \psi}{\partial z}$$

$$w = \frac{\partial \phi}{\partial z} + \frac{\partial \psi}{\partial x} \qquad \text{(C5)}$$

will be used in the remainder of this discussion.

6. In order to express potentials of ϕ and ψ in terms of coordinates x and z, let

$$\phi = f(z)e^{ik(ct-x)}$$

$$\psi = g(z)e^{ik(ct-x)} \qquad \text{(C6)}$$

(where c is the wave velocity in X-direction) in Equation C3 and solve for $f(z)$ and $g(z)$. Then,

$$f(z) = A_1 \exp\left[+ik\left(\sqrt{\frac{c^2}{\alpha^2} - 1}\right)z\right] + A_2 \exp\left[-ik\left(\sqrt{\frac{c^2}{\alpha^2} - 1}\right)z\right]$$

$$g(z) = B_1 \exp\left[+ik\left(\sqrt{\frac{c^2}{\beta^2} - 1}\right)z\right] + B_2 \exp\left[-ik\left(\sqrt{\frac{c^2}{\beta^2} - 1}\right)z\right] \qquad \text{(C7)}$$

where A_1 , A_2 , B_1 , B_2 are constants to be determined by boundary conditions. Therefore,

$$\phi(x,z,t) = A_1 \exp\left\{ik\left[ct + \left(\sqrt{\frac{c^2}{\alpha^2} - 1}\right)z - x\right]\right\} + A_2\left\{ik\left[ct - \left(\sqrt{\frac{c^2}{\alpha^2} - 1}\right)z - x\right]\right\}$$

$$\psi(x,z,t) = B_1 \exp\left\{ik\left[ct + \left(\sqrt{\frac{c^2}{\beta^2} - 1}\right)z - x\right]\right\} + B_2\left\{ik\left[ct - \left(\sqrt{\frac{c^2}{\beta^2} - 1}\right)z - x\right]\right\} \qquad (C8)$$

In air B_1 and B_2 are zero since there are no shearing stresses. So,

$$\phi_{air} = A_1 \exp\left\{ik\left[ct + \left(\sqrt{\frac{c^2}{\alpha^2} - 1}\right)z - x\right]\right\} + A_2 \exp\left\{ik\left[ct - \left(\sqrt{\frac{c^2}{\alpha^2} - 1}\right)z - x\right]\right\} \qquad (C9)$$

and in the ground there are only transmitted waves so that

$$\phi_{ground} = A' \exp\left\{ik\left[ct + \left(\sqrt{\frac{c^2}{\alpha'^2} - 1}\right)z - x\right]\right\}$$

$$\psi_{ground} = B' \exp\left\{ik\left[ct + \left(\sqrt{\frac{c^2}{\beta'^2} - 1}\right)z - x\right]\right\} \qquad (C10)$$

where primed values indicate transmitted waves and c is the apparent velocity along the surface given by

$$c = \frac{\alpha}{\cos \gamma} = \frac{\alpha'}{\cos \gamma'} = \frac{\beta'}{\cos \delta'} \tag{C11}$$

and $kc = \omega$ = circular frequency . The following notation is convenient to use for calculations:

$$a = \sqrt{\frac{c^2}{\alpha^2} - 1} = \tan \gamma$$

$$a' = \sqrt{\frac{c^2}{\alpha'^2} - 1} = \tan \gamma' \tag{C12}$$

$$b' = \sqrt{\frac{c^2}{\beta'^2} - 1} = \tan \delta'$$

where angles γ , γ' , and δ' are as shown in Figure 25. With this notation Equations C9 and C10 become

$$\phi = A_1 \exp\left[ik(ct + az - x)\right] + A_2 \exp\left\{ik\left[ck(ct - az - x)\right]\right\}$$

$$\phi' = A' \exp\left[ik(ct + a'z - x)\right] \tag{C13}$$

$$\psi' = B' \exp\left[ik(ct + b'z - x)\right]$$

where z is positive in the upward direction

$$\text{and if } \; c = \frac{\alpha}{\cos \gamma} < \alpha' \; , \; a' \text{ is imaginary}$$

$$\text{or, if } \; c < \beta' \text{ , then } \; b' \text{ is imaginary} \tag{C14}$$

The velocities chosen to approximate conditions at the test site were

α = acoustic velocity = 340 m/sec

α' = compression wave velocity = 340 m/sec and 358 m/sec

β' = 160 m/sec

An α' of 340 m/sec approximates first-layer conditions (see Table 1 of main text). Since α and α' are equivalent, there is no angle for which α' is imaginary. However, if an α' of 358 m/sec is chosen, then a' is imaginary for an incident angle less than

$$\gamma = \cos^{-1}\left(\frac{\alpha}{\alpha'}\right) = 18.25 \text{ deg} \tag{C15}$$

This is the critical angle of incidence. For angles less than this, a compression wave is not propagated in the downward vertical direction below the surface and the amplitude is attenuated exponentially with depth below the surface.

7. The boundary conditions (Equation C1) can be applied to get the relationship between reflected and transmitted waves and the incident wave. As the vertical displacement is given by

$$w = \frac{\partial \phi}{\partial z} + \frac{\partial \psi}{\partial x} \tag{C16}$$

at $z = 0$,

$$w_{air} = \left[ik\left(\frac{c^2}{\alpha^2} - 1\right)A_1 - ik\left(\frac{c^2}{\alpha^2} - 1\right)A_2\right] \exp[ik(ct - x)]$$

$$w_{ground} = \left[ik\left(\frac{c^2}{\alpha'} - 1\right)A' - ik\,B'\right] \exp[ik(ct - x)] \tag{C17}$$

Equating these,

$$\left(\frac{c^2}{\alpha^2} - 1\right)(A_1 - A_2) = \left(\frac{c^2}{\alpha'^2} - 1\right)A' - B'$$

or (C18)

$$a\,(A_1 - A_2) = a'A' - B'$$

8. Vertical stress is given by

$$P_{zz} = \lambda\Theta + 2\mu \frac{\partial w}{\partial z}$$

$$P_{zz} = \lambda \frac{\partial^2 \phi}{\partial x^2} + (\lambda + 2\mu) \frac{\partial^2 \phi}{\partial z^2} + 2\mu \frac{\partial^2 \psi}{\partial x \partial z} \tag{C19}$$

where λ and μ are Lame's constants. In terms of compression and shear wave velocities, they are given by

$$\lambda = \rho(\alpha^2 - \beta^2)$$

$$\mu = \rho\beta^2 \tag{C20}$$

where ρ = density of medium . For air, β is zero and at the surface z is zero, so the vertical stress in air at the surface is given by

$$p_{zz} = \left[-k^2\lambda(A_1 + A_2) - k^2\lambda\left(\frac{c^2}{\alpha^2} - 1\right)(A_1 + A_2)\right] \exp[ik(ct - x)], \tag{C21}$$

since $\mu = 0$ for air. Substituting $\lambda = \rho\alpha^2$ into Equation C20 gives

$$p_{zz} = -k^2 (\rho\alpha^2 + a^2)(A_1 + A_2) \exp[ik(ct - x)]$$

Taking the absolute value and reducing gives

$$p_{zz} = k^2\rho c^2 (A_1 + A_2) \exp[ik(ct - x)] \tag{C22}$$

For the ground at $z = 0$

$$p'_{zz} = \lambda \frac{\partial^2 \phi'}{\partial x^2} + (\lambda + 2\mu) \frac{\partial^2 \phi'}{\partial z^2} + 2\mu \frac{\partial' \psi'}{\partial x \partial z}$$

$$= \left[\lambda(-k^2 A') + (\lambda + 2\mu)(-k^2 a'^2 A') + 2\mu(-k^2) b' B'\right] \exp[ik(ct - x)]$$

$$= -\rho' k^2 \beta'^2 \left[\left(\frac{c^2}{\beta'^2} - 2\right) A' + 2b' B'\right] \exp[ik(ct - x)] \qquad (C23)$$

Equating P_{zz} and P'_{zz},

$$\rho c^2 (A_1 + A_2) = \rho' \beta'^2 \left[(b'^2 - 1)A' - 2b' B'\right] \qquad (C24)$$

9. The tangetial stress is given by

$$P_{zx} = \frac{\partial w}{\partial x} + \frac{\partial u}{\partial z} = \rho \beta^2 \left(2 \frac{\partial^2 \phi}{\partial x \partial z} + \frac{\partial^2 \psi}{\partial x} - \frac{\partial^2 \psi}{\partial z}\right) \qquad (C25)$$

For air at the surface

$$P_{zx} = \rho \beta^2 \left[2(-ik)(ika)A_1 + (-ik)(ika)A_2\right] \exp[ik(ct - x)] \approx 0 \qquad (C26)$$

(since $\beta = 0$)

For the ground at the surface

$$P'_{zx} = \rho \beta'^2 \left[2(-ik)(ika')A' + (ik)^2 B'\right] \exp[ik(ct - x)] = 0 \qquad (C27)$$

(since $p_{zx} = 0$)

or

$$A' = \frac{-1}{2a'} (b'^2 - 1)B' \qquad (C28)$$

10. So three equations from the boundary conditions are:

$$a(A_1 - A_2) = a'A' - b'B'$$

$$\rho c^2(A_1 + A_2) = \rho'\beta'^2\left[(b'^2 - 1)A' - 2b'B'\right] \qquad (C29)$$

$$0 = 2a'A' + (b'^2 - 1)B'$$

The solutions for the unknown coefficients (A_2, A', B') given A_1 are:

$$\frac{A_2}{A_1} = \frac{-\rho a'c^4/\beta'^2 + \mu' a\left[(c^2/\beta'^2 - 2)^2 + 4a'b'\right]}{\rho a'c^4/\beta'^2 + \mu' a\left[(c^2/\beta'^2 - 2)^2 + 4a'b'\right]}$$

$$\frac{A'}{A_1} = \frac{2\rho ac^2(c^2/\beta'^2 - 2)}{\rho a'c^4/\beta'^2 + \mu' a\left[(c^2/\beta'^2 - 2)^2 + 4a'b'\right]} \qquad (C30)$$

$$\frac{B'}{A_1} = -\frac{4\rho aa'c^2}{\rho a'c^4/\beta'^2 + \mu' a\left[(c^2/\beta'^2 - 2)^2 + 4a'b'\right]}$$

These results can be used to derive a theoretical intensity ratio to compare to the intensity ratio results of the data analysis by expressing the theoretical vertical component of velocity and the acoustic pressure in terms of ϕ and ψ or equivalently in terms of A_1, ρ, β, α, and α'.

Acoustic Pressure

11. Approximating the pressure variation in a sound wave is an adiabatic process.[11] Then

$$\frac{P'}{P} = \left(\frac{V}{V'}\right)^{\gamma} \qquad (C31)$$

where

P, P' = any two pressures

V, V' = volumes associated with P and P', respectively

$\gamma = 1.4$ for air

However,

$$\rho V = \text{constant} = \text{mass}$$

or

$$V = \text{constant}/\rho$$

where

ρ = mass density

so that

$$\frac{P'}{P} = \left(\frac{\rho'}{\rho}\right)^{\gamma}$$

$$= (1 + s)^{\gamma} \qquad \text{(C32)}$$

$$\simeq 1 + \gamma s$$

where

$s = (\rho' - \rho)/\rho$

ρ, ρ' = densities associated with P, P'

The approximation is good for $s \ll 1$. For the measured data

$P \equiv P_o$ = static air pressure $\simeq 1.0 \times 10^6$ μbars

P' = instantaneous pressure, and $P' - P_o$ is of the order of one microbar. Therefore,

$$\frac{P' - P_o}{P_o} \simeq 10^{-6}$$

or

$$P'/P_o \simeq 1.0$$

and

$$\rho'/\rho = 1 - s \simeq 1$$

so that $s << 1$, as required in approximation of Equation C32. From Equation C32,

$$P' = P_o(1 + \gamma s)$$

and (C33)

$$P = P' - P_o = P_o \gamma s$$

12. The equation of motion for a volume element can be expressed in terms of the pressure, P, and velocity of the volume element, $\vec{v}$, as

$$\vec{\nabla} P = -\rho \frac{\partial \vec{v}}{\partial t} \qquad (C34)$$

The motion of the volume element due to pressure P is regarded as irrotational, i.e., curl $\vec{v}$ vanishes. Therefore, $\vec{v}$ can be written as the gradient of a scalar function defined to be Φ. Using the scalar function, referred to as the velocity potential, Equation C34 becomes:

$$\nabla \vec{P} = -\rho \frac{\partial}{\partial t} \vec{\nabla} \Phi$$

where

$\vec{v}$ = displacement velocity

Φ = scalar velocity potential

so

$$\vec{\nabla}\left(\rho\,\frac{\partial\Phi}{\partial t} + P\right) = 0$$

and (C35)

$$\rho\,\frac{\partial^2\Phi}{\partial t^2} = -\,\frac{\partial P}{\partial t}$$

or substituting for P from Equation C33

$$\rho\,\frac{\partial^2\Phi}{\partial t^2} = -P_o\gamma\,\frac{\partial s}{\partial t}$$

Then, using

$$-\vec{\nabla}\cdot\vec{v} = \frac{\partial\vec{s}}{\partial t} \qquad (C36)$$

Equation C35 reduces further to

$$\rho\,\frac{\partial^2\Phi}{\partial t^2} = P_o\gamma(\vec{\nabla}\cdot\vec{v})$$

$$= P_o\gamma\left[\vec{\nabla}\cdot(\vec{\nabla}\Phi)\right]$$

$$= P_o\gamma\cdot\nabla^2\Phi$$

so

$$\nabla^2\Phi = \frac{\rho}{P_o\gamma}\,\frac{\partial^2\Phi}{\partial t^2}$$

(C37)

or

$$\nabla^2\Phi = \frac{1}{\alpha^2}\,\frac{\partial^2\Phi}{\partial t^2}$$

where

$$\alpha^2 = \frac{P_o\gamma}{\rho}$$

A solution of the wave equation (Equation C37) is

$$\Phi = A \cos k\,(\alpha t - x) \tag{C38}$$

then

$$\vec{\nabla}\Phi = \vec{v} = v_x = -k\,A \sin k\,(\alpha t - x) \tag{C39}$$

Equation C36 gives

$$s = \frac{\rho}{P_o \gamma} \frac{\partial \Phi}{\partial t}$$

or

$$s = \frac{Ak}{c} \sin k(\alpha t - x) \tag{C40}$$

and

$$P = P' - P_o = P_o \gamma s \text{ (from Equation C33)}$$

or

$$P = \rho c^2 \left(\frac{Ak}{c}\right) \sin k\,(\alpha t - x) \tag{C41}$$

substituting Equation C39 into Equation C41, get

$$P = \rho \alpha v \tag{C42}$$

13. Equation C42 expresses the sound pressure as a function of the displacement velocity. Since velocity is just a derivative of the scalar and vector displacement potentials, the theoretical intensity ratio can be expressed in terms of A_2 , A_1 , and B' .

14. The seismic data used in calculating the intensity ratio was taken with a geophone oriented vertically. The vertical displacement w

for the plane wave being discussed is given in Equation C5 as

$$w = \frac{\partial \phi}{\partial z} + \frac{\partial \psi}{\partial x}$$

In the ground

$$w' = \text{Real}\left(\frac{\partial \Phi'}{\partial z} + \frac{\partial \psi'}{\partial x}\right)$$

$$w' = \text{Real}\left\{ ik(a'A' - B')\exp\left[ik(ct - x)\right]\right\} \tag{C43}$$

The velocity is

$$\frac{\partial w'}{\partial t} = \text{Real}\left\{ -k^2 c(+a'A' - B')\exp\left[ik(ct + x)\right]\right\} \tag{C44}$$

For incident P wave, A_1 is real (i.e., has no phase term) so

$$\frac{\partial w'}{\partial t} = -k^2 c A_1 \text{ Real}\left(a'\frac{A'}{A_1} - \frac{B'}{A_1}\exp\left[ik(ct - x)\right]\right) \tag{C45}$$

for $z = 0$. Then, substituting for A'/A_1 and B'/A_1 from Equation C30,

$$\frac{\partial w'}{\partial t} = -k^2 c A_1 \text{ Real } \frac{2\rho a' a c^2\left(\frac{c^2}{\beta'^2} - 4\right)}{\rho a' \frac{c^4}{\beta'^2} + \mu' a\left[\left(\frac{c^2}{\beta'^2} - 2\right)^2 + 4a'b'\right]} \tag{C46}$$

if a' is real, the argument of Real is real.

15. The quantities a and b' are necessarily real, however, a' can be imaginary for $a' = 358$ m/sec and γ less than 18.25 deg. If a' is imaginary, then the argument of Real needs to be separated into real and imaginary parts. Then for $x = t = 0$,

$$\frac{\partial w'}{\partial t} = -k^2 c A_1 \frac{2\rho a' a c^4/\beta'^2\left(\rho a' \dfrac{c^4}{\beta'^2} + 4\mu' a' a b'\right)}{\left(\rho a' \dfrac{c^4}{\beta'^2} + 4\mu' a' a b'\right)^2 + \left[\mu' a\left(\dfrac{c^2}{\beta'^2} - 2\right)^2\right]^2} \qquad (C47)$$

where $a' = ||a'||$

16. The acoustic signal was measured with an omnidirectional microphone. The plane wave being used in the approximation has no y-dependence, so the displacement is given by

$$u^2 + w^2 = \left\{\left[\mathrm{Re}\left(\frac{\partial \phi}{\partial x} - \frac{\partial \psi}{\partial z}\right)\right]^2 + \left[\mathrm{Re}\left(\frac{\partial \phi}{\partial z} + \frac{\partial \psi}{\partial z}\right)\right]^2\right\}^{1/2} \qquad (C48)$$

where Re indicates the real part of expression in the argument of Re . But $\psi = 0$ for air, therefore,

$$u^2 + w^2 = \left\{\left[\mathrm{Re}\left(\frac{\partial \phi}{\partial x}\right)\right]^2 + \left[\mathrm{Re}\left(\frac{\partial \phi}{\partial z}\right)\right]^2\right\}^{1/2} \qquad (C49)$$

The velocity associated with this displacement in the air is

$$v = \frac{\partial}{\partial t}\sqrt{u^2 + w^2} \qquad (C50)$$

For $x = t = 0$,

$$v = \left[\left(\mathrm{Re}\left\{-k^2 c\left[A_1 \exp(-ikaz) + A_2 \exp(ikaz)\right]\right\}\right)^2 + \left(\mathrm{Re}\left\{-k^2 ca\left[-A_1 \exp(-ikaz) + A_2 \exp(ikaz)\right]\right\}\right)^2\right]^{1/2}$$

or,

$$v = \left\{ -k^2 cA_1 \left[-\cos(kaz) + \left|\left|\frac{A_2}{A_1}\right|\right| \cos(kaz) + \kappa) \right]^2 + a^2 \left[-\cos(kaz) + \left|\left|\frac{A_2}{A_1}\right|\right| \cos(kaz + \kappa) \right]^2 \right\}^{1/2} \tag{C51}$$

where κ is the phase difference between A_2 and A_1 and κ equals 0 for a' real . For a' real :

$$v = -k^2 cA_1 \cos(kaz) \left(\left\{ - \frac{2\mu' a \left[\left(\frac{c^2}{\beta'^2} - 2 \right)^2 + 4a'b' \right]}{\rho a' \frac{c^4}{\beta'^2} + \mu' a \left[\left(\frac{c^2}{\beta'^2} \right)^2 + 4a'b' \right]} \right\}^2 + a^2 \left\{ \frac{2\rho a' \frac{c^4}{\beta'^2}}{\rho a' \frac{c^4}{\beta'^2} + \mu' a \left[\left(\frac{c^2}{\beta'^2} - 2 \right)^2 + 4a'b' \right]} \right\}^2 \right)^{1/2} \tag{C52}$$

But if a' is imaginary, then use

$$\left|\left|\frac{A_2}{A_1}\right|\right| = \left\{ \frac{\left(4\mu' a'ab' - \rho a' \frac{c^4}{\beta'^2} \right)^2 + \left[\mu' a \left(\frac{c^4}{\beta'^2} - 2 \right)^2 \right]^2}{\left(4\mu' a'ab' + \rho a' \frac{c^4}{\beta'^2} \right)^2 + \left[\mu' a \left(\frac{c^2}{\beta'^2} - 2 \right)^2 \right]^2} \right\}^{1/2} \tag{C53}$$

and

$$\kappa = \tan^{-1}\left[\frac{\mathrm{Im}\left(\frac{A_2}{A_1}\right)}{\mathrm{Re}\left(\frac{A_2}{A_1}\right)}\right]$$

or

$$\kappa = \tan^{-1}\left\{\frac{\left(-2\rho a'\frac{c^4}{\beta'^2}\right)^2 + \mu a\left(\frac{c^2}{\beta'^2} - 2\right)^2}{\left[\mu' a\left(\frac{c^4}{\beta'^2}\right)^2\right]^2 + (4\mu' a' ab')^2 - \left(\rho a'\frac{c^4}{\beta'^2}\right)^2}\right\} \qquad (C54)$$

in the previous equation for velocity (Equations C51). This equation for particle velocity in the air together with Equation C42 gives an expression for the acoustic pressure P.

17. The computed intensity ratio (v^2/P^2) becomes, for a' real

$$\frac{v^2}{P^2} = \frac{\left(\rho a' a c^4/\beta'^2\right)^2}{[\rho\alpha\cos(kaz)]^2\left(\left(\rho\alpha a'\frac{c^4}{\beta'^2}\right)^2 + \left\{\mu' a\left[\left(\frac{c^2}{\beta'^2} - 2\right)^2 + 4a'b'\right]\right\}^2\right)} \qquad (C55)$$

and for a' imaginary

$$\frac{v^2}{p^2} = \left(\frac{\rho a' a \frac{c^4}{\beta'^2} \left(\rho a' \frac{c^4}{\beta'^2} + 4\mu a' a b' \right)^2}{\left\{ \left(\rho a' \frac{c^4}{\beta'^2} + 4\mu' a' a b' \right)^2 + \left[\mu' a \left(\frac{c^2}{\beta'^2} - 2 \right)^2 \right]^2 \right\}^2} \right)$$

$$\times \left[\left(\cos(kaz) + \left\{ \frac{\left(4\mu' a' a b' - \rho a' \frac{c^4}{\beta'^2} \right)^2 + \left[\mu' a \left(\frac{c^4}{\beta'^2} - 2 \right)^2 \right]^2}{\left(4\mu' a' a b' + \rho a' \frac{c^4}{\beta'^2} \right)^2 + \left[\mu' a \left(\frac{c^4}{\beta'^2} - 2 \right)^2 \right]^2} \right\}^{1/2} \cos(kaz + \kappa) \right)^2 \right. \qquad \text{(C56)}$$

$$\left. + a^2 \left(-\cos(kaz) + \left\{ \frac{\left(4\mu' a' a b' - \rho a' \frac{c^4}{\beta'^2} \right)^2 + \left[\mu' a \left(\frac{c^4}{\beta'^2} - 2 \right)^2 \right]^2}{\left(4\mu' a' a b' + \rho a' \frac{c^4}{\beta'^2} \right)^2 + \left[\mu' a \left(\frac{c^4}{\beta'^2} - 2 \right)^2 \right]^2} \right\}^{1/2} \cos(kaz + \kappa) \right)^2 \right]$$

Figure 26 and Plates 22-26 show the theoretical intensity ratio results. Figure 26 shows results for z = 0.0 m and incident angles 5 to 80 deg. Plates 22-26 show results for z = 1.0 m . A peak is present in these spectra due to interference effects in the acoustic spectra.

APPENDIX D: SITE CHARACTERIZATION MEASUREMENTS

Introduction

1. This appendix describes the measurement of seismic and atmospheric properties of the test site. The quantities chosen to describe the seismic properties were compression and shear wave velocities, and layer depths associated with them, and Rayleigh wave velocity (frequency-dependent). The quantity chosen to describe the atmospheric properties was coherence length. Another quantity that may be useful in describing the site is the ground surface impedance. Measurement for this quantity will also be discussed in this appendix.

Measurement of Seismic Velocities

Compression wave velocity

2. The compression wave velocities for each layer and the refraction layer thickness of the surface material (0-10 m in depth) at the test site were measured in a refraction seismic survey.[12] The seismograph used in Test I was an SIE Geophysical Instrumentation Model R4, 24-channel recorder with an SIE Model RS44 amplifier. A newer seismograph was used in Test II, an SIE Model R6, 24-channel recorder with an SIE Model 49R amplifier. The geophones used with these recorders were Mark Products Model L10 sensitive to vertical particle velocity.

Shear wave velocity

3. The same recording equipment was used as in the compression wave velocity measurement; however, the geophones used were sensitive to horizontal particle velocity, and the source of the signal for the tests was generated by hitting a board on its side rather than on the top as for compression wave measurements.

Rayleigh wave velocity

4. The signal for the Rayleigh wave measurement was generated by a Goodman Industries electromagnetic vibrator. This vibrator has a 50-lb force output with a frequency range of 20-10,000 Hz. The maximum frequency needed for these measurements was less than 300 Hz. The same

recording equipment was used as for the other velocity measurements, but the geophone spacing was adjusted to be less than a wavelength.

Measurement of Coherence Length and Ground Surface Impedance

5. This section of the appendix defines the terms "coherence length" and "ground surface impedance" and gives the results of measurements for determining them. It was not necessary to determine a value of the coherence length. It was necessary only that it exceeded ranges necessary in the experiment (30 m). Ground surface impedance values were determined as a function of frequency.

Coherence length

6. If the source of acoustic energy emits an infinitely long monochromatic wave train having spherical or plane wave fronts, such that the phase difference between the sensed wave train at any two fixed points spaced any distance apart is time-independent, the waves exhibit perfect temporal coherence. If the phase difference between the wave trains sensed at any two fixed points in a plane normal to the ray direction is time-independent, the wave exhibits perfect lateral coherence. Similarly, if the phase difference between the wave train sensed at any two fixed points along a ray direction is time-independent, the waves exhibit perfect radial coherence. In general, air turbulence and refraction effects will affect the transmission of an acoustic wave and will limit the separation distance between microphones such that the waves received by them are coherent. In practice, the radial coherence length is measured by moving a microphone radially away from a reference microphone near the source until the cross-correlation between the two microphones falls to $1/e$ (where e is the base of the natural logarithm) of the value it would have if the two microphones were collocated. The lateral coherence length is measured by moving two microphones apart maintaining the same distance from the source until the cross-correlation between the two microphones falls to $1/e$ of the value they had when they were collocated. These measurements of lateral and radial coherence length should provide comparable values.

7. Figure D1 presents the correlation function derived from two microphones laterally separated by the indicated distance (0, 1, 3, 5, and 10 m). The broadcast signal was band limited white noise (45-1800 Hz). The correlation function exceeds 1/e (i.e., 0.37) for each separation distance so that the lateral coherence length is greater than 10 m. These measurements were made during Test I just before the surface impedance measurements.

8. Although the data are not presented in this report, coherence length measurements were obtained several times during the test. A correlation function was calculated between geophones separated by 30 m radially outward from speaker during the surface impedance measurements in Test I. The results showed that the radial coherence length was greater than 30 m.

9. In Test II, lateral and radial coherence length measurements were made and found to be greater than 30 m, even though the wind velocity was high (2.7-3.7 m/sec) during these measurements. Since the other measurements (velocity, intensity ratio, etc.) were made in less windy conditions, it seems reasonable to expect that the coherence length was greater than 30 m throughout the tests.

Surface impedance

10. The surface impedance provides a measure of the manner in which the acoustic wave interacts with the ground surface. It is obtained by measuring the interaction between the waves received at the microphone directly from the source and those reflected from the ground surface (prior to their arrival at the microphone). Appendix B discusses the theoretical considerations of acoustic waves at a boundary in terms of impedance values of the two media. Only a few measurements of the surface impedance of the ground have been reported. The surface impedance of mowed grass has been measured by using a vertical impedance tube technique,[13] and by using interference phenomena at oblique angles of incidence.[14] Other measurements of the surface impedance of the ground under a pine plantation[15] and in a stubble field[16] indicate a value of surface impedance similar to that reported for grass.

11. Measurements were made at the University of Mississippi over

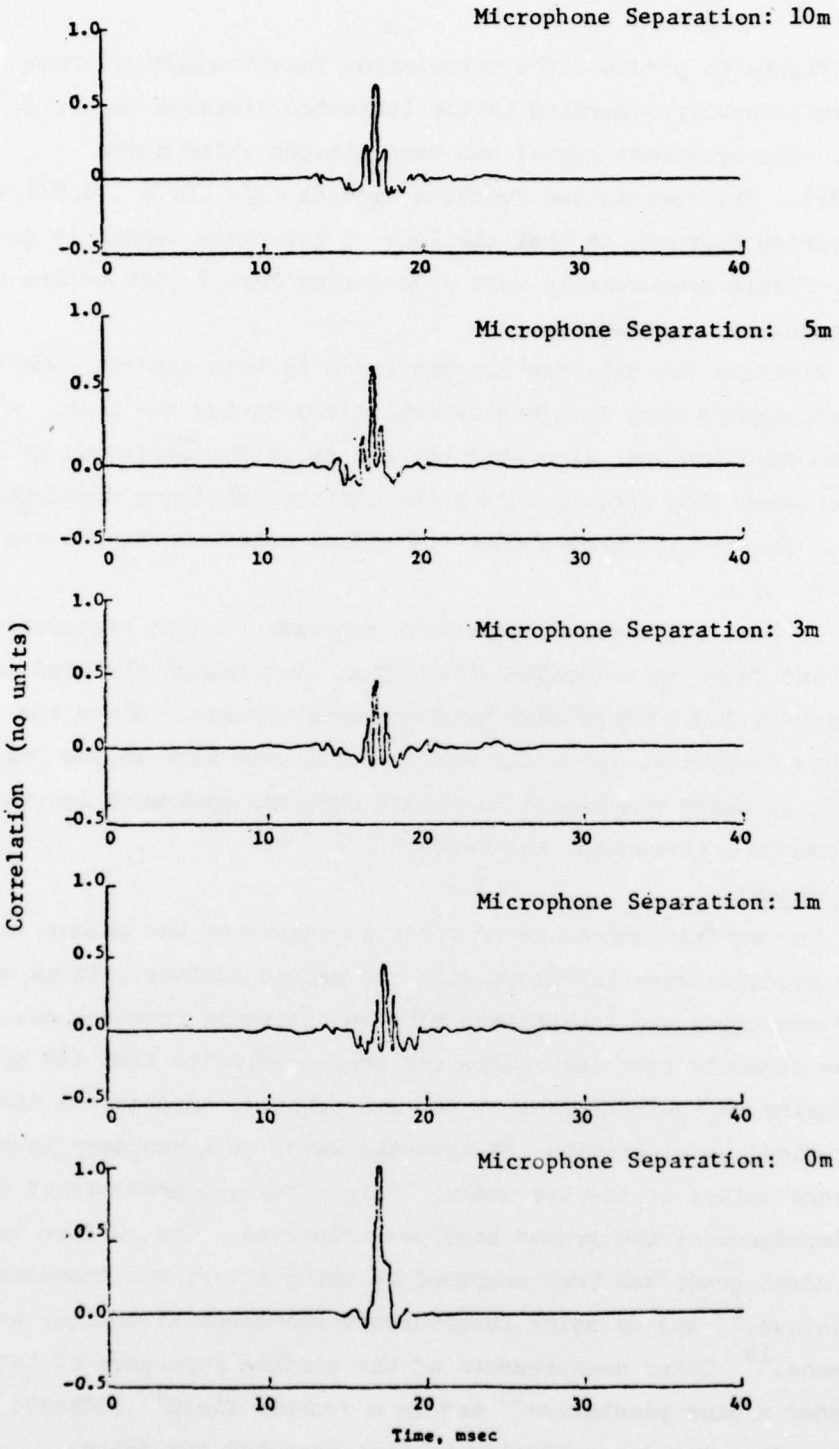

Figure D1. Correlation function used for determining lateral coherence length

a soybean field during the course of one growing season in an effort to obtain additional information on the parameters needed to characterize the surface impedance.[17] Pao and Evans[18] had indicated that the effectiveness of ground attenuation depends critically on the elevation angle of the sound source, and the initial results of the measurements made over the soybeans with a fixed source height were consistent with this theory. It was felt that additional data, over various ground covers taken with a range of source and receiver heights to vary the angle of the sound source, were necessary.

12. For the surface impedance measurement, the source types were pure tones and octave band pink noise (Table 3 in main text). The signals from the microphones were transcribed to AM 1/4-track tape and played on a Crown 800 tape recorder. Each octave band limited pink noise signal was analyzed for surface impedance measurements using a GR 1554-A Sound and Vibration Analyzer in the 1/3-octave band pass-filter mode. Examples of the frequency domain of an octave band noise signal and the response of the 1/3-octave band filter used in the surface impedance analysis centered at 1000 Hz are shown as Figure D2. The signal sound pressure level (SPL) was averaged for each band of noise for each microphone position. These data were corrected for microphone gain settings and entered into the program for analysis discussed later.

13. The surface impedance was determined using an interactive search procedure on the computer. The search procedure is designed so as to converge on a value of the surface impedance that satisfies the mathematical model of acoustic propagation discussed in Appendix B. The experimentally measured sound pressure for each microphone height and source-to-sensor separation was entered into the program. Then an initial surface impedance was assumed (impedance for institutional grass for that frequency), and the sound pressure level at each experimental distance and microphone height was computed. The difference between computed and measured SPL's was stored, the impedance was incremented a small amount, and the process was repeated. Since the surface impedance consists of real and imaginary parts, this procedure was repeated over a two-dimensional grid of real and imaginary parts of the impedance

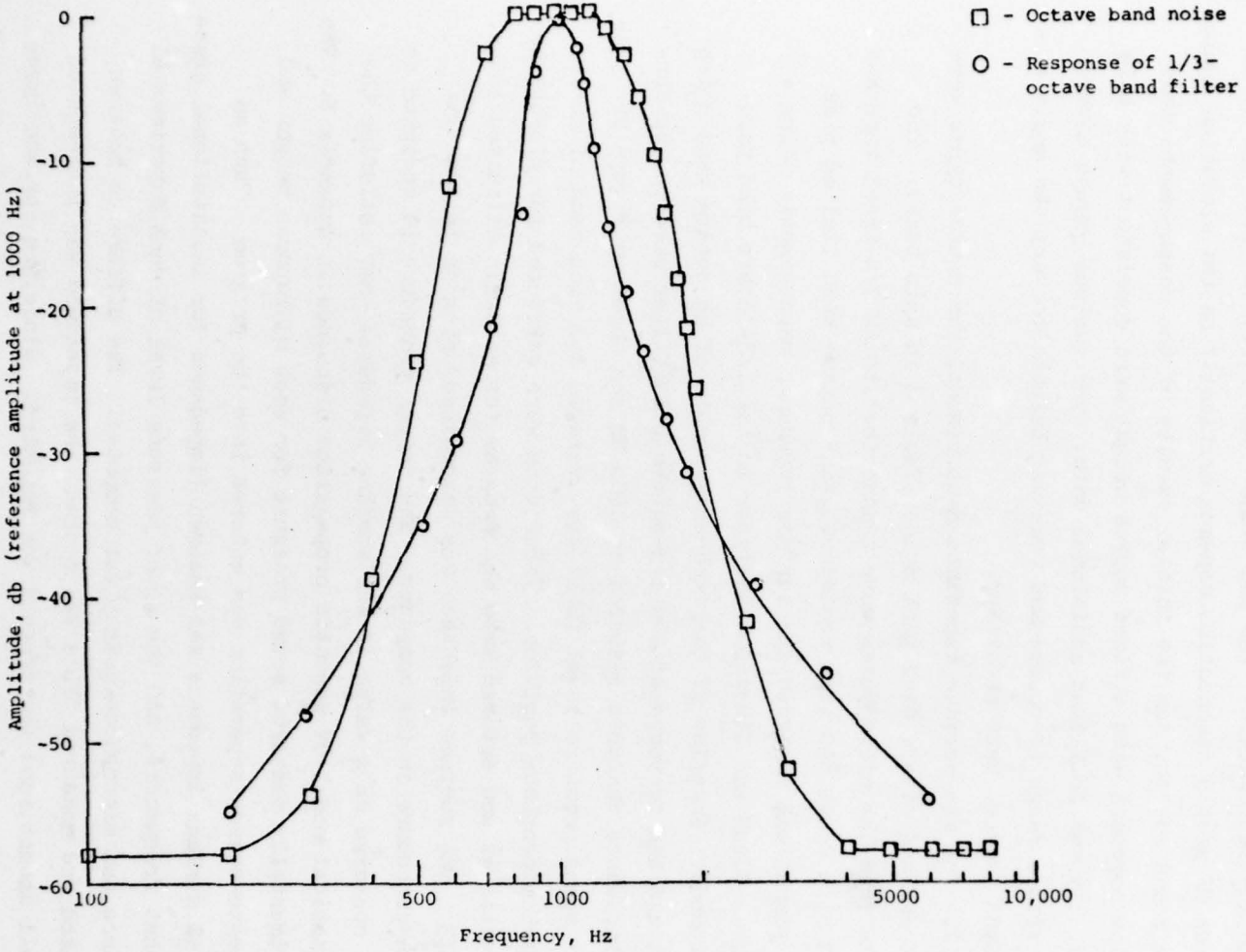

Figure D2. Example of octave band noise and the response of the 1/3-octave band filter

until that pair of values that gave the smallest difference between measured and computed SPL's was found. That pair of values (the real and imaginary parts of the impedance) was assumed to be the impedance of the surface at the frequency of concern. The values obtained in this manner will be referred to as experimental values.

14. From a theoretical point of view, the surface impedance should be a smooth function of frequency dependent on another parameter referred to as the "specific flow resistance." An empirical relation between specific flow resistance per unit thickness (σ) and surface impedance has been developed by Chessel[19] and is given by

$$\frac{X}{\rho_o c} = -11.9\left(\frac{f}{\sigma}\right)^{-0.73}$$

$$\frac{R}{\rho_o c} = 1.0 + 9.08\left(\frac{f}{\sigma}\right)^{-0.75}$$

where

X = imaginary part of impedance

ρ_o = density of the air at normal temperature and pressure

c = velocity of sound in air

$\rho_o c$ = characteristic impedance of air

f = frequency, Hz

σ = specific flow resistance per unit thickness, g/cm^3-sec

R = real part of impedance

The values of impedance found as described in paragraph 13 were used to compute σ for each frequency using the above relations; then the surface impedance Z was computed for this average σ at each frequency for which Z had been determined using the method of Appendix B. The computed values of the real and imaginary parts of the surface impedance for Tests I and II are given in Figure D3. The experimental values (paragraph 13) are also presented in Figure D3. (The values of σ were found to be 300 g/cm^3-sec for Test I and 130 g/cm^3-sec for Test II.) There is significant deviation between the computed and experimental

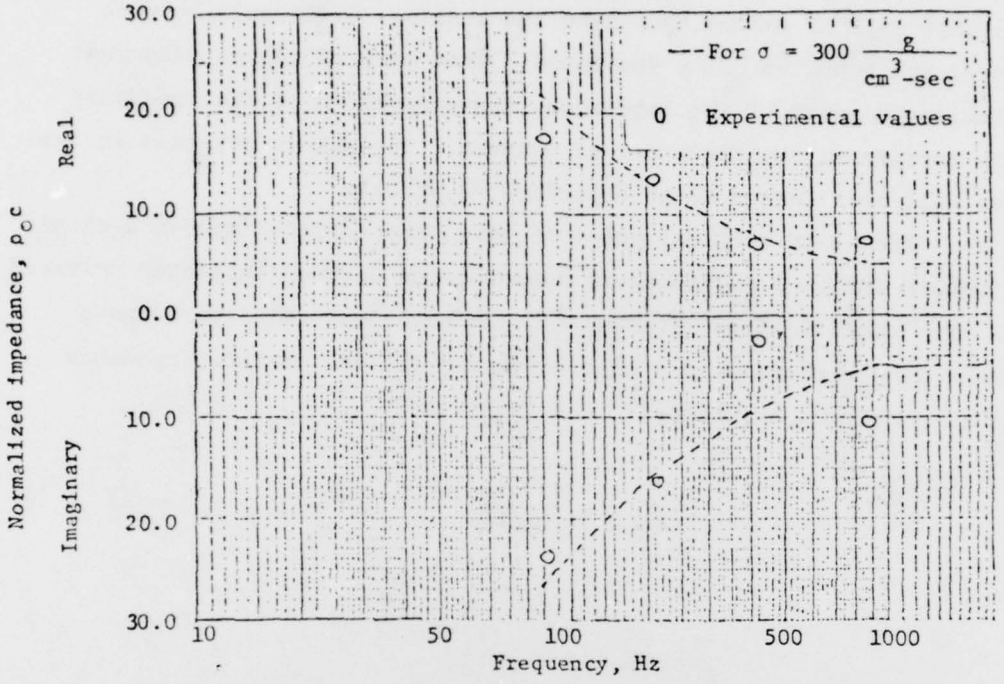

a. Test I

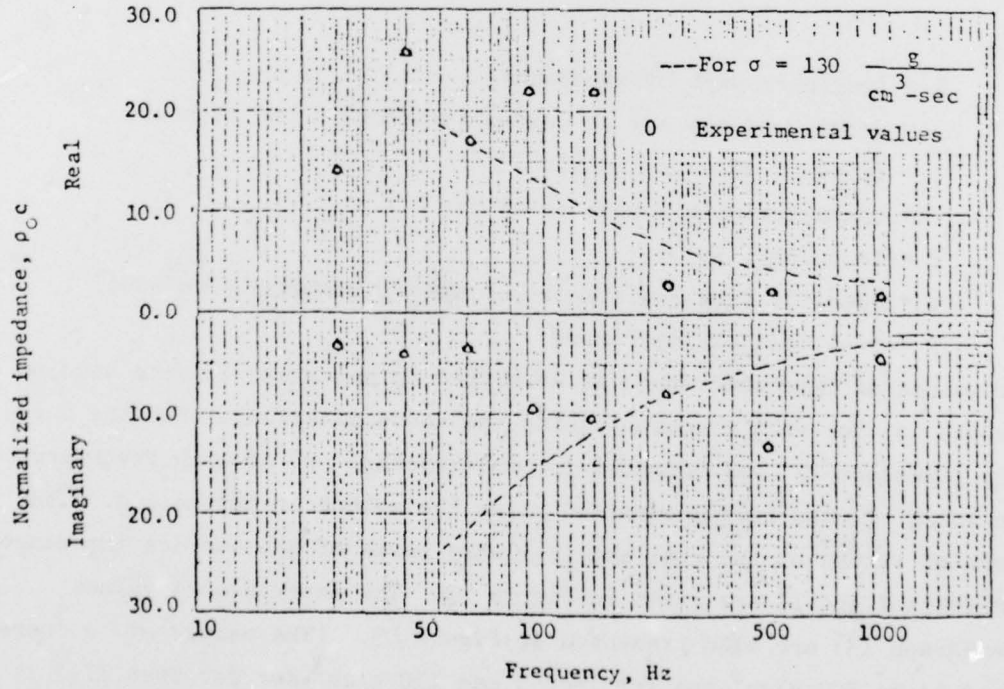

b. Test II

Figure D3. Impedance values for Test I and Test II

Z-values below 100 Hz. It is not clear whether this deviation is due to the theoretical model used to derive the experimental values (which has not been tested below 100 Hz) or poor signal-to-noise ratio for the measured data.

15. The values of specific flow resistance are in general agreement with the findings of Dickinson and Doak.[13] They found that σ for dry soils varied between 10 g/cm^3-sec for sandy soil and 490 g/cm^3-sec for clay. The first set of measurements (Test I) was for a fairly hard and dry surface, hence a value of σ near that of clay is not surprising. The second set of measurements (Test II) were taken when the soil was very wet. This supports the findings of Dickinson and Doak[13] that "a slight amount of moisture, instead of partly filling up the pores and increasing the flow resistance, rather brings about increased surface repulsion between the grains, causing the material to bulk and open up the pores."

16. Following the first series of measurements, it was obvious that the primary region of interest for the test configurations possible was from 20 Hz to 500 Hz. It was decided, therefore, for the surface impedance measurements of Test II to eliminate the 9.152-m (6-in.) steps in altitude and increase the number of speaker-to-microphone distances used. This would provide better impedance values at low frequencies. The results of this analysis are given in Figure D3. The dotted lines in this figure show impedance values for the computed specific flow resistance per unit thickness.

17. Some additional analysis was done for the Test II surface impedance measurement data to investigate the sensitivity of the experimental values of impedance to errors in measurement. The SPL at each frequency was measured with an error of ± 2 db. To observe the effect of such errors on the calculated impedance value, several sets of data representing deviations in the measured data due to measurement error were inserted into the calculation. The results of introducing such errors into the calculation of surface impedance are presented for a frequency of 220 Hz. The experimental values obtained from the measured data for 220 Hz was 2.5 $\rho_o c$ (real) and 9.0 $\rho_o c$ (imaginary). Table D1

shows that for the first test of the sensitivity of the impedance calculation to measurement error, a measured value of SPL at each distance (10, 20,...70 m) was uniformly increased by 2 db, and these data were inserted into the program for calculation. No change in calculated impedance resulted. The measured data inserted into the computer program were then alternately varied by adding 1 db to the 10-m SPL, subtracting 1 db from the 20-m SPL, adding 1 db to the 30-m SPL, etc. This variation was repeated with 1 db subtracted from the SPL at 10 m, 1 db added to the SPL at 20 m, etc., and alternating +1 db, then -1 db every 10 m. The results of a second test alternating the addition of ± 2 db to the data for both sequences are also given in Table D1. These variations in SPL did not affect the calculated impedance more than 3 $\rho_o c$. The measured SPL is not a strong function of the impedance, since the direct sound wave dominates. Thus, the calculated impedance is not extremely sensitive to changes in the measured values of SPL, and the choice of the best value for the impedance has some uncertainty. It was assumed, however, that if the process was repeated independently for each frequency, the resultant points would define the trend of frequency-dependence.

Table D1

Sensitivity of Surface Impedance Calculations to Error in Measured Sound Pressure Level

Data at 220 Hz	Normalized Impedance in Units of $\rho_o c$	
	Real	Imaginary
Original data	2.5	9.0
Adding +5 db to data	2.5	9.0
Adding +1 db, -1 db in sequence to data	3.1	8.4
Adding -1 db, +1 db in sequence to data	1.7	9.7
Adding +2 db, -2 db in sequence to data	3.1	7.8
Adding -2 db, +2 db in sequence to data	0.9	11.0

In accordance with letter from DAEN-RDC, DAEN-ASI dated 22 July 1977, Subject: Facsimile Catalog Cards for Laboratory Technical Publications, a facsimile catalog card in Library of Congress MARC format is reproduced below.

Flohr, Mark D
Acoustic-to-seismic coupling; properties and applications to seismic sensors / by Mark D. Flohr, Daniel H. Cress. Vicksburg, Miss. : U. S. Waterways Experiment Station ; Springfield, Va. : available from National Technical Information Service, 1979.
48, [72] p., 26 leaves of plates : ill. ; 27 cm. (Technical report - U. S. Army Engineer Waterways Experiment Station ; EL-79-1)
Prepared for Sandia Laboratories, Albuquerque, New Mexico.
References: p. 47-48.

1. Acoustic detection. 2. Acoustic signatures. 4. Acoustic-to-seismic coupling. 5. Mathematical models. 6. Seismic detection. 7. Seismic sensors. I. Cress, Daniel H., joint author. II. Sandia Laboratories. III. Series: United States. Waterways Experiment Station, Vicksburg, Miss. Technical report ; EL-79-1.
TA7.W34 no.EL-79-1